u!nnovation.

UNITED IMAGING

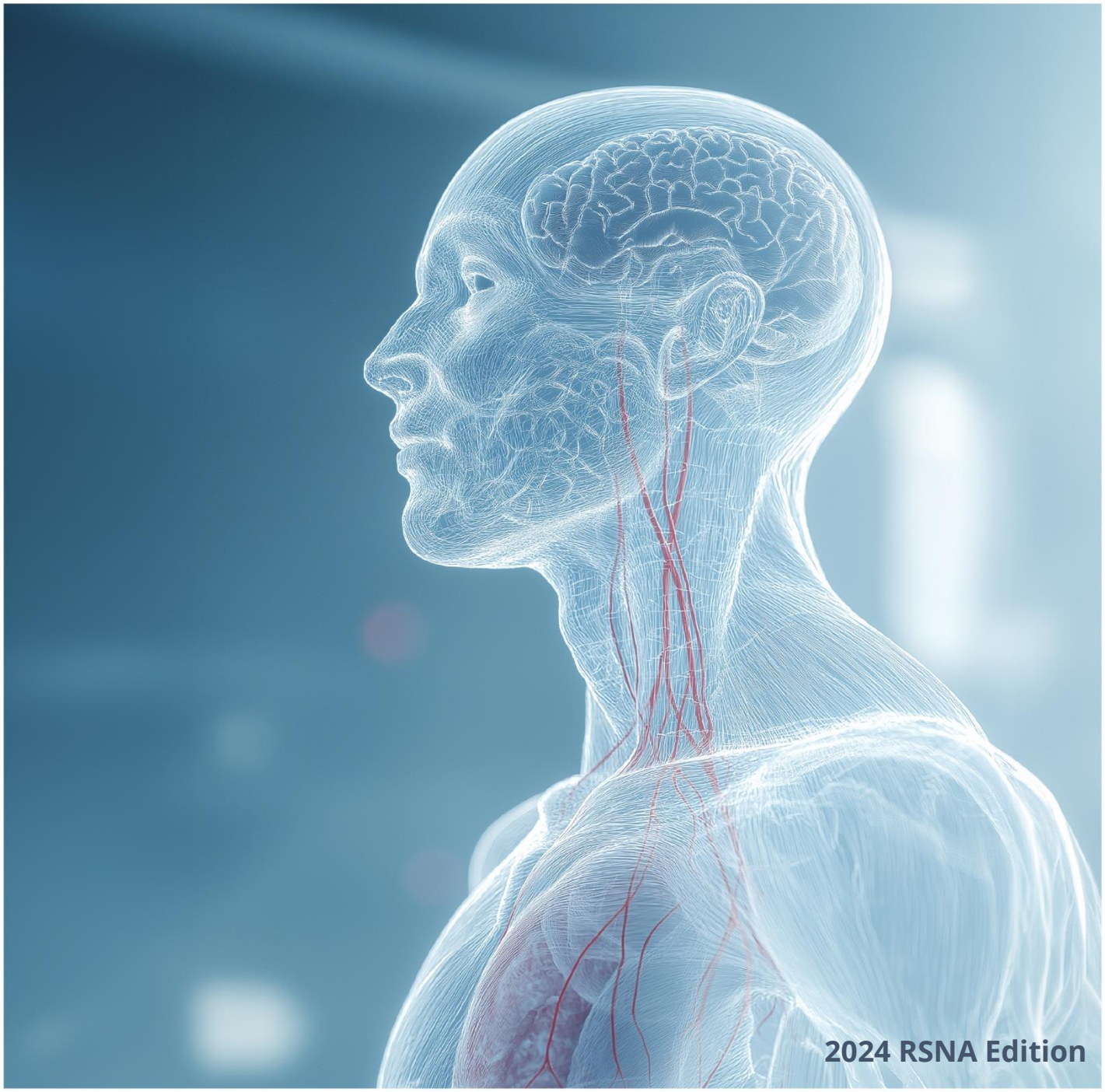

Issue Highlights

Editorial Board

Editors/Reviewers

Contributors

Disclaimer

The articles contained in this magazine are provided solely by the authors, and the author(s) of each article appearing in this magazine is/are solely responsible for the content thereof as well as personal data, which is used anonymously or complied with applicable data privacy laws or regulations. United Imaging Healthcare makes no representation or warranties, expressly or impliedly, with respect to the accuracy, timeliness, reliability, legitimacy, applicability, fitness, originality, or completeness of the contents of this magazine. United Imaging Healthcare assumes no legal responsibility or liability for any error, omission, or illegality with respect to the material contained within.

All articles contained in this magazine only represent the opinions and views of the authors and do not implicitly or explicitly represent any official positions or policies, or medical opinions of United Imaging Healthcare or the institutions with which the authors are affiliated unless this is clearly specified. Discussions of any brand, services, or products in the magazine should not be construed as promotion or endorsement thereof.

Articles published in this magazine are intended to inspire further general scientific research, investigation, understanding, and discussion only and are NOT intended to and should not be relied upon as recommending or promoting a specific medical advice, method, diagnosis, or treatment by physicians for any particular individual, nor to replace the advice of a medical doctor or other healthcare professional. Any individual wishing to apply the information in this magazine for the purposes of improving their own health should not do so without consulting with a qualified medical practitioner. All patients need to be treated in an individual manner by their personal medical advisors. The decision to utilize any information in this magazine is ultimately at the sole discretion of the reader, who assumes full responsibility for any and all consequences arising from such a decision. United Imaging Healthcare makes no representations or warranties with respect to any treatment, action, or application of medication or preparation by any person following the information offered or provided within or through the magazine. United Imaging Healthcare shall remain free of any fault, liability, or responsibility for any loss or harm, whether real or perceived, resulting from the use of information in this magazine.

The articles included in this magazine may contain work in progress, which represents ongoing research and development. Such technologies are not available for sale in the United States for clinical use and also may not be available for such sales in other countries around the world.

Please note that the magazine is intended to be distributed only within a limited scope instead of publication.

If you have any questions about the magazine, or simply wish to reach out to us for any other reasons, you are welcomed to contact us at the following email address: compliance@united-imaging.com

About uINNOVATION

——

Welcome to uINNOVATION, our new, recurring collection of perspectives from leading global experts in the medical imaging field. Technologies discussed in the articles of the 2024 edition of uINNOVATION may contain work in progress, which represents ongoing research and development. Such technologies are not available for sale in the United States for clinical use and also may not be available for such sales in other countries.

If you have any questions about the magazine, or simply wish to reach out to us for any other reasons, you are welcomed to contact us at the following email address: compliance@united-imaging.com

To download the uINNOVATION 2024 edition, click on the links below or Scan the QR Code.
https://global.united-imaging.com/en/uinnovation/uInnovation-magazine

This magazine is 100% funded and edited by United Imaging Healthcare.

Authors or their institutions may have received or currently receive financial support from United Imaging Healthcare, as indicated in each article.

About United Imaging Healthcare

——

United Imaging Healthcare is a provider of high-end medical equipment and medical IT solutions. From our headquarters in Shanghai's Jiading district to our network of research and development centers throughout the world, our global mission is to provide medical institutions with a full range of healthcare solutions, from diagnostic imaging and radiation therapy equipment to service, training, and medical IT solutions. We are dedicated to expanding access to high-quality medical care and improving the value of our services.

VISION

——

Leading Healthcare Innovation

MISSION

——

To Bring Equal Healthcare for All

To learn more,
visit https://www.united-imaging.com/

No. 2258 Chengbei Rd, Jiading District, Shanghai, 201807

Business Consultation: +86 (21)-67076666

Email: info.global@united-imaging.com

www.united-imaging.com

9370 Kirby Drive, Houston, Texas 77054

www.united-imaging.com

Editorial: The Transformative Power of Neurological Imaging: Pushing the Boundaries of Brain Science

Hemant Patel[a]
[a]Gujrat Imaging Center (GIC) Prime, India

The human brain has long been considered the final frontier in medicine. Despite centuries of research, its complex structure and function continue to captivate scientists and clinicians alike. Neurological imaging has emerged as a pivotal tool, transforming the field of neuroscience by providing unprecedented insight into the brain's architecture and activity. From detecting early signs of disease to exploring consciousness, brain imaging technologies have revolutionized both diagnosis and research in neurology.

Neurological imaging has come a long way since the early days of X-ray imaging. The modern era of brain imaging began with the invention of the computed tomography (CT) scan in the early 1970s, followed by the development of magnetic resonance imaging (MRI) and positron emission tomography (PET). These technologies allow us to peer inside the brain in ways that would have been unimaginable just decades ago.

Enhancing Diagnostics and Personalized Medicine

Neurological imaging has revolutionized the way we diagnose and treat conditions such as epilepsy, multiple sclerosis, and traumatic brain injuries. High-resolution MRI scans allow for the precise identification of lesions and abnormalities, while advances in diffusion tensor imaging (DTI) have enabled the visualization of the brain's white matter pathways, crucial for understanding diseases that affect brain connectivity.

Beyond diagnosis, imaging plays a vital role in personalized medicine. By analyzing the structure and function of an individual's brain, doctors can tailor treatments to the specific needs of the patient. For example, in epilepsy, imaging helps to identify the exact location of seizure activity, guiding surgical interventions that can dramatically improve the quality of life for patients who do not respond to medication.

Imaging has also become crucial in the early detection of neurodegenerative diseases. Alzheimer's disease, which begins its destructive course years before noticeable symptoms emerge, can now be detected early through imaging biomarkers. This is a game-changer in developing treatments that can slow or halt the progression of the disease before irreversible damage occurs.

Challenges and Ethical Considerations

Despite the transformative potential of neurological imaging, the field faces significant challenges. One of the most pressing is the interpretation of the vast amount of data generated by these technologies. Brain scans produce detailed and complex images that require expert analysis. Artificial intelligence (AI) and machine learning have already begun to play a role in this area, offering the potential for more accurate and faster diagnoses, but there is still a long way to go in making this a reliable tool in clinical settings.

Moreover, as our ability to image the brain becomes more precise, ethical questions inevitably arise. fMRI studies can reveal a great deal about an individual's mental processes, raising concerns about privacy. Could these technologies be misused to infer thoughts, emotions, or even intentions? How do we balance the benefits of neurological imaging with the need to protect individuals' cognitive liberty?

The Future of Neurological Imaging

Neurological imaging is rapidly advancing with the introduction of non-contrast-enhanced magnetic resonance angiography (NCE-MRA) at ultra-high magnetic fields. Traditionally performed at 1.5T and 3T, NCE-MRA is now expanding into the realm of ultra-high field imaging with systems like the 5.0T uMR® Jupiter, which offers whole-body vascular scans without the need for contrast agents. This has been introduced and described very well by author Li Hao in his article "Preliminary Application of 5.0T Whole Body Non-Contrast-Enhanced Magnetic Resonance Angiography". This article discusses this new platform and its enhancements in signal-to-noise ratio (SNR), resolution, and acquisition speed, particularly in brain vessel imaging, with

fewer limitations than the 7T systems.

Further Fei King, Zhaojuan Xie and Wenhui Ma focus on validation and evaluation of a vendor provided head motion correction algorithm on uMI Panorama PET/CT system in our next article.

The article describes about NeuroFocus [1] Algorithm that aims at Revolutionizing Head Motion Correction in PET Imaging. A new data-driven approach, the NeuroFocus algorithm, offers a promising solution by detecting, estimating, and correcting motion using PET raw data without the need for additional hardware or patient restraints. This study is a landmark validation of NeuroFocus, focusing on its effectiveness in detecting and correcting head motion during 18F-FDG brain PET/CT imaging.

Further this magazine delves into the advancements and future potential of brain PET imaging, focusing on the uNeuroEXPLORER [2] system. Dr. Richard Carson, in his interview, highlights the significance of PET brain evolution, starting from the HRRT scanner to the recent innovations in imaging technology. He discusses the improvements in resolution, sensitivity, and patient comfort enabled by the new system, which promises to open new avenues in the study of neurological disorders like Parkinson's and Alzheimer's. The interview emphasizes the growing role of brain PET in both clinical and research settings, particularly in disease diagnosis, drug development, and treatment monitoring.

In the next article, authors Marufjon Salokhiddinov and Gulnara Rahkimbaeva introduce the aspects of machine learning in the diagnosis of Alzheimer Disease (AD). A recent study leveraged cutting-edge deep learning techniques, specifically the Cascaded Weakly Supervised Confidence Integration Network (CINet), to measure brain volume in healthy controls (HC) and individuals with mild AD. The study used MRI data from the Alzheimer's Disease Neuroimaging Initiative (ADNI) to analyze and compare GM and WM volumes.

In this magazine we not only focus on facilitation of cutting-edge imaging but the UIH collaborative initiative with our various collaborators that continues to push the boundaries of brain imaging, supported by key philanthropic contributions and a crucial collaboration with Stony Brook to optimize PET technology for neurological applications with uMI 550 PET model.

The author Paul Vaska focuses on the practical challenges, such as patient positioning and head motion, and addresses them through customized protocols, including the use of infrared-based motion tracking systems, ensuring precise data collection and analysis.

Recent advancements in MRI technology are propelling the field of neuroimaging into a new territory. High-resolution brain mapping, crucial for understanding cognition and diagnosing neurological diseases, has traditionally faced limitations due to physical constraints like scan time, resolution, and signal-to-noise ratio (SNR). However, the next authors Liyi Kang and Dan Wu focus on NeuroFrontier[3] 3.0T MRI system from United Imaging Healthcare which has allowed us to overcome many of these obstacles with innovations in ultra-high gradient strength, artificial intelligence (AI), and motion correction techniques, marking a significant step forward in brain imaging.

Recent developments in ultra-high field MRI, particularly with systems operating at 5T and 7T, have revolutionized the field of neurological imaging. Authors Zhensong Wang and Jie Gan focuses on a comparative study between 5T and 3T MRI, emphasizing the benefits of 5T in capturing more detailed anatomical images without extending scanning time. Importantly, the study highlights that ultra-high field MRI is particularly beneficial for detecting small lesions and subtle brain changes that may be missed at lower field strengths. This advancement holds promise for improving the diagnosis and treatment planning for conditions like multiple sclerosis, epilepsy, and other neurodegenerative diseases.

Acute ischemic stroke (AIS) represents a significant global health challenge, necessitating rapid and effective imaging techniques to optimize patient outcomes. In a groundbreaking study, authors Jin Fang and Guihua Jiang explored the efficacy of a one-stop dynamic whole-brain

[1,2,3] This product is not available for sale in the U.S. for clinical uses and also may not be available for such sales in other countries.

computed tomography perfusion (CTP) protocol using a 320-row scanner (uCT 960+, United Imaging Healthcare) to streamline imaging for AIS patients. The study highlights that timely recanalization can markedly improve clinical outcomes, underscoring the importance of swiftly identifying salvageable brain tissue.

The final article of this issue discusses the advancement of MULTIPLEX MRI (MTP)[4] as a transformative tool in the characterization of brain tumors. The author H.K. Anand of this study highlights the effectiveness of machine learning (ML) algorithms in processing of MTP MRI data for automated tumor classification, revealing that combinations of T1, T2*, and QSM provide superior diagnostic performance compared to individual parameters.

Looking ahead, the future of neurological imaging is poised for even greater advances. Emerging technologies such as ultra-high-field MRI, optogenetics, and advanced PET tracers promise to further refine our ability to image the brain at both structural and functional levels. These tools could revolutionize the way we understand psychiatric disorders like depression and schizophrenia, which have long eluded clear-cut diagnostic criteria.

Neurological imaging has already transformed the practice of neurology and the broader field of brain science.

Collectively, this issue of uINNOVATION 2024 offers an insight into the new innovations in the field of neuroimaging. From diagnosis to personalized treatments, from understanding brain function to correcting the head motion, the future of neurological imaging promises both tremendous opportunities and significant challenges. What is clear, however, is that brain imaging is, and will remain, at the heart of modern neurology, guiding the field into a future where the mysteries of the brain become ever clearer.

Guest Editor Biography

Dr. Hemant Patel
Professor of Radiology and Managing Director
Gujarat Imaging Centre,
Post Graduate Institute of Radiology and Imaging
Ahmedabad, Gujarat, India

Dr. Hemant Patel is the Director of Gujrat Imaging Center group of diagnostics centres and Professor of Radiology at the Post-Graduate Institute of Radiology & Imaging in Ahmedabad. Dr Patel obtained his MBBS degree followed by advanced medical degrees such as DMRE, MD and DNB in the field of radiology. In the year 2018, Dr Patel had served as the national president of Indian Radiological Imaging Association (IRIA). Dr Patel has been awarded best radiology entrepreneur at Health Express Radiology conclave in the year 2019. Dr Patel had published over 200 scientific articles in the field of radiology and delivered over 80 scientific talks at various national and international avenues, and he is the editor of "Comprehensive Textbook of Clinical Radiology" published under Elsevier. Currently, Dr Patel holds Executive Committee position at World Radiology Society and Treasurer of Asian Oceanic Society of Radiology. Dr Patel is also serving as RSNA Coordinator for Asian Subcontinents.

[4] This product is not available for sale in the U.S. for clinical uses and also may not be available for such sales in other countries.

Preliminary Application of 5T Whole Body Non-Contrast-Enhanced Magnetic Resonance Angiography

Hao Li[1*], Xianyi Zhang[1], Zhang Shi[2], Weirui Cai[1], He Wang[1]
[1] The Institute of Science and Technology for Brain-inspired Intelligence, Fudan University, Shanghai, 200433
[2] Department of Radiology, Zhongshan Hospital, Fudan University, Shanghai 200032

1. Introduction

Non-contrast-enhanced magnetic resonance angiography (NCE-MRA) generates vascular images without the use of exogenous contrast agents, thus avoiding the risks associated with gadolinium-based contrast agents. It is widely used for vascular disease screening and assessment in various body regions.

Currently, clinical NCE-MRA scanning is primarily performed at 1.5T and 3T. Recent advancements in ultra-high field (field strength >3T) magnetic resonance equipment have enabled vascular imaging at higher field strengths. Increasing the main magnetic field strength is expected to bring many improvements to NCE-MRA, particularly in enhanced signal-to-noise ratio (SNR), resolution and acquisition efficiency. The 7.0T MR system, a typical ultra-high field MR, has shown significant advantages in intracerebral MRA compared to 1.5T and 3T (1). However, its use is limited by B1+/B0 inhomogeneity and the lack of body imaging coils, restricting it mostly to brain vessel scanning. Some pioneering studies have explored using custom transmit-receive coils for 7T body vascular imaging in the lower extremities (2, 3) and kidneys (4, 5), but these efforts face challenges like B1+ field inhomogeneity, causing blood signal loss and uneven image brightness (3, 5).

The uMR® Jupiter 5T is the first whole-body ultra-high field magnetic resonance imaging system, bringing new opportunities for ultra-high field whole-body NCE-MRA. This system features a large aperture 8-channel parallel transmit volume coil, combined with receiving coils suitable for multiple regions, enabling whole-body multi-regional scanning. Additionally, compared to 7.0T, the 5T field strength is expected to alleviate B1+ field inhomogeneity and RF heating issues, providing better suitability for body imaging. This article categorizes and reviews NCE-MRA methods, analyzes the advantages and challenges of NCE-MRA at ultra-high fields, and discusses NCE-MRA schemes applicable to different body regions using the 5T MR imaging platform.

2. Classification of NCE-MRA Techniques

Based on different principles, most NCE-MRA techniques can be divided into the following three categories:

2.1. Techniques Based on Inflow Enhancement Effect

NCE-MRA based on the inflow enhancement effect utilizes specific methods to suppress stationary tissue signals in the imaging region. Since the blood protons outside the imaging region are not yet excited, they generate high signal intensity relative to stationary tissues upon entering the imaging layer. Typical techniques include Time-of-Flight (TOF), inflow inversion recovery (IFIR) (6), quiescent interval single shot (QISS) (7), and arterial spin labeling (ASL).

TOF can be acquired in either 2D or 3D mode, using repeated excitation of RF pulses based on a gradient-echo sequence to saturate the static tissues within the imaging layer. IFIR and QISS utilize a 180°inversion recovery pulse and a 90° saturation pulse, respectively, to saturate the background signal in the imaging region and acquire MRA images after a predetermined wait time, allowing unsaturated blood to flow in. The former is suitable for observing renal and hepatic arteries, while the latter is commonly used for imaging the limbs and iliac arteries. ASL methods perform subtraction processing on images of labeled and unlabeled upstream blood to eliminate background signals, and are applicable for imaging blood vessels in the head (8), neck (9), chest, and abdomen (10).

2.2. Techniques Based on Spin-Phase Effect

Under the action of bipolar gradients, the stationary protons in background tissues experience no net phase shift, while the moving protons in the blood undergo a net phase shift proportional to their velocity, enabling NCE-MRA based on the spin-phase effect. Phase contrast (PC) can measure the

net phase shifts of blood protons in three directions to obtain blood signals and calculate blood flow velocity, representing spin-phase effect NCE-MRA. Besides conventional 2D and 3D acquisition modes, PC can introduce a time dimension for cine or 4D flow imaging (11), facilitating dynamic blood flow monitoring.

Fresh blood imaging (FBI) (12) and flow-sensitized dephasing (FSD) (13, 14) can generate NCE-MRA images by subtracting arterial high-signal bright blood images (diastole) from arterial low-signal images based on the spin-phase effect (systole). FBI uses ECG gating and sets appropriate delay times based on differences in blood flow velocity and phase dispersion between diastole and systole, generating dark-bright blood images. FSD employs specially designed blood suppression pre-pulses to inhibit blood flow signals, effectively differentiating between arteries and veins (13, 15, 16).

2.3. Techniques Based on Blood T1/T2 Values

NCE-MRA based on inflow enhancement or spin-phase effects relies on blood flow, and its effects diminish in cases of slow blood flow or complex vasculature. In balanced steady-state free precession (bSSFP) sequence images, tissue signals are proportional to the tissue T2/T1 ratio. Blood, having a higher T2/T1 ratio, appears as a high signal in bSSFP sequences, enabling flow-independent NCE-MRA. Previous studies (17–19) have shown that combining bSSFP sequences with T2 preparation pulses, fat suppression pulses, and T1 contrast modulation pre-pulses helps to fully suppress background signals, making it suitable for coronary and aortic imaging.

The aforementioned three types of NCE-MRA techniques have different applicable scenarios. Existing research is mostly limited to MR equipment of 3T and below, lacking studies on the applicability of ultra-high-field imaging, especially body imaging. The unique environment of ultra-high-field MR poses higher demands on imaging techniques, necessitating the selection of the optimal NCE-MRA imaging and technical schemes based on the study area.

3. Analysis of Ultra-High Field Vascular Imaging Techniques

For vascular imaging, increasing the main magnetic field strength can bring the following advantages:

1. Improved Signal-to-Noise Ratio (SNR): The most direct advantage of increased signal strength at ultra-high fields, resulting in higher SNR and blood-to-background contrast-to-noise ratio.
2. Shortened Scan Time: Based on increased signal strength, ultra-high fields can achieve higher acceleration factors, reducing acquisition time.
3. Increased Resolution: Higher SNR and greater acceleration factors help improve spatial resolution, presenting vascular structures and pathological features more clearly within the same examination time.
4. Increased Blood-to-Background Contrast: As tissue T1 values increase with field strength, ultra-high fields can improve background suppression for inflow enhancement methods (such as TOF, IFIR, QISS) and enhance labeling efficiency for ASL methods.

Higher field strengths also bring many technical challenges to vascular imaging:

1. B1+ Field Inhomogeneity: The smaller RF wavelength at higher field strengths (3T: 27 cm, 5T: 16 cm, 7.0T: 12 cm) can cause standing wave effects due to insufficient penetration through the body, affecting B1+ field homogeneity. This effect can cause uneven image signals and blood signal loss, especially in body imaging (20, 21).
2. B0 Field Inhomogeneity: At ultra-high fields, the inhomogeneity of the main magnetic field (B0) is also more severe, potentially causing off-resonance artifacts and more severe blood signal dephasing. bSSFP sequences are particularly sensitive to these issues.
3. RF Heating Effects: The higher RF pulse energy at ultra-high fields increases patient energy deposition, raising the risk of thermal burns, further limiting the application of RF-intensive sequences like FSE.

4. Application of 5T MRA in Different Regions

The unique advantages and challenges of ultra-high-field imaging require researchers to select the most appropriate NCE-MRA imaging methods and techniques based on different anatomical regions. This section selects several typical body parts to demonstrate feasible technical schemes and example images.

4.1 Data Acquisition

The following 5T example images were acquired using the United Imaging uMR Jupiter 5T MRI scanner. Intracranial and foot vascular scans used a 48-channel head transmit-receive coil, while chest, abdominal, and lower limb vascular scans used a 48-channel spine receive coil and a 24-channel body receive coil. The 3T control images were acquired using the United Imaging uMR® 790 3T MRI scanner. This study has been approved by the Ethics Committee of the Institute of Brain Science and Technology, Fudan University (FE222691). All subjects were healthy volunteers who signed informed consent forms

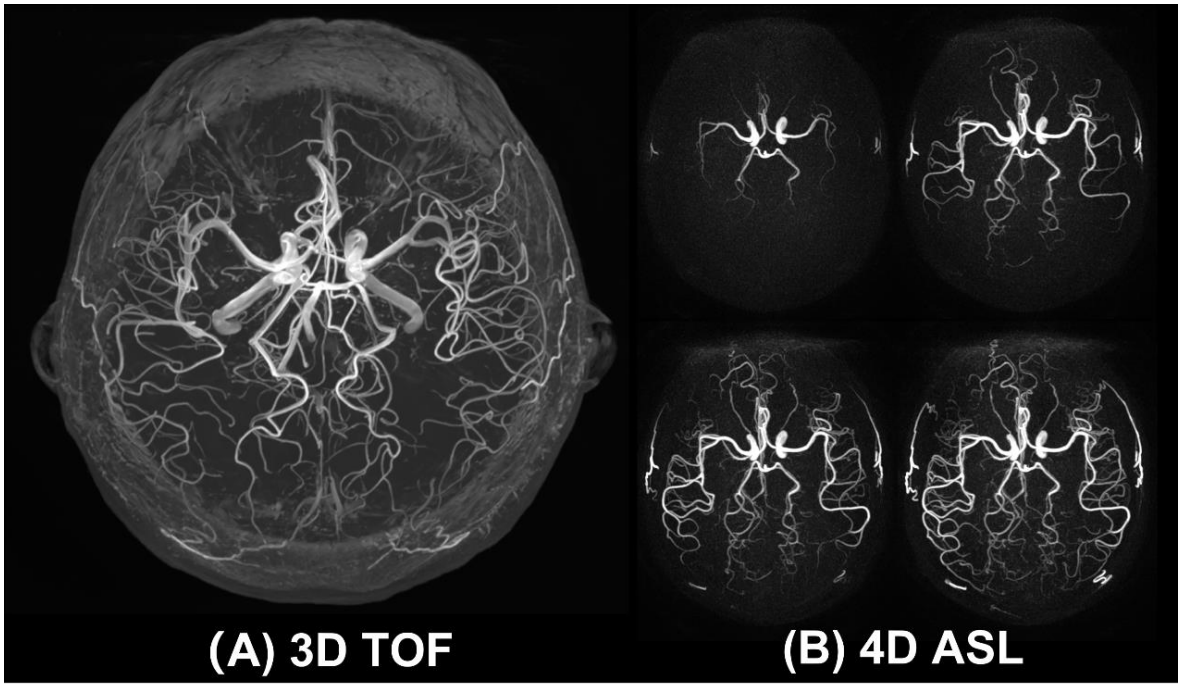

Figure 1. Examples of 5T intracranial MRA. A. 3D TOF maximum intensity projection (MIP) image (healthy male, 24 years old). B. 4D ASL MIP images at post-labeling delay times of 300, 600, 900 and 1500 ms(healthy male, 34 years old).

4. Application of 5T MRA in Different Regions

The unique advantages and challenges of ultra-high-field imaging require researchers to select the most appropriate NCE-MRA imaging methods and techniques based on different anatomical regions. This section selects several typical body parts to demonstrate feasible technical schemes and example images.

4.1 Data Acquisition

The following 5T example images were acquired using the United Imaging uMR Jupiter 5T MRI scanner. Intracranial and foot vascular scans used a 48-channel head transmit-receive coil, while chest, abdominal, and lower limb vascular scans used a 48-channel spine receive coil and a 24-channel body receive coil. The 3T control images were acquired using the United Imaging uMR 790 3T MRI scanner. This study has been approved by the Ethics Committee of the Institute of Brain Science and Technology, Fudan University (FE222691). All subjects were healthy volunteers who signed informed consent forms.

4.2 Cerebral Vessels

3D TOF is the most commonly used method for intracranial MRA and shows good applicability at ultra-high fields (Figure 1A). Zhang et al. conducted a comprehensive quantitative evaluation of 3D TOF at 3T, 5T, and 7T field strengths, revealing that 5T TOF significantly outperforms 3T and that its quantitative results are consistent with those at 7T (22).

As a novel dynamic MRA technique, 4D ASL can capture dynamic changes in blood flow within the intracranial arterial

system by acquiring images at different post-labeling delay times, allowing for the detection of arterial abnormalities such as stenosis, dilation, or thrombosis. Figure 1B shows example images of 5T 4D ASL at different post-labeling delay times.

4.3 Thoracic and abdominal Vessels

The IFIR technique based on the inflow effect can effectively be used for vascular imaging of thoracic and abdominal organs. Figure 2 shows 5T renal MRA obtained using the IFIR sequence (United Imaging: Flow-Inversion Nonenhanced (FINE) 3D). For imaging of the aorta and other chest vessels, the flow-independent bSSFP technique can be used. Additionally, 4D Flow technology, with high temporal resolution, can dynamically present blood flow changes and achieve quantitative flow measurements, showing potential for application at 5T ultra-high field.

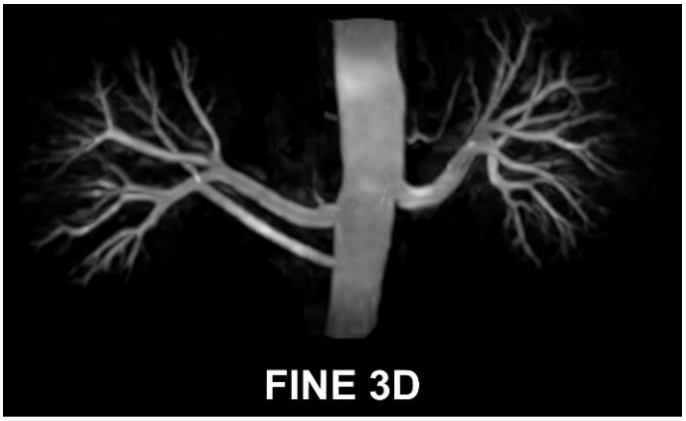

Figure 2. Example of 5T FINE 3D renal artery imaging (healthy male, 38 years old).

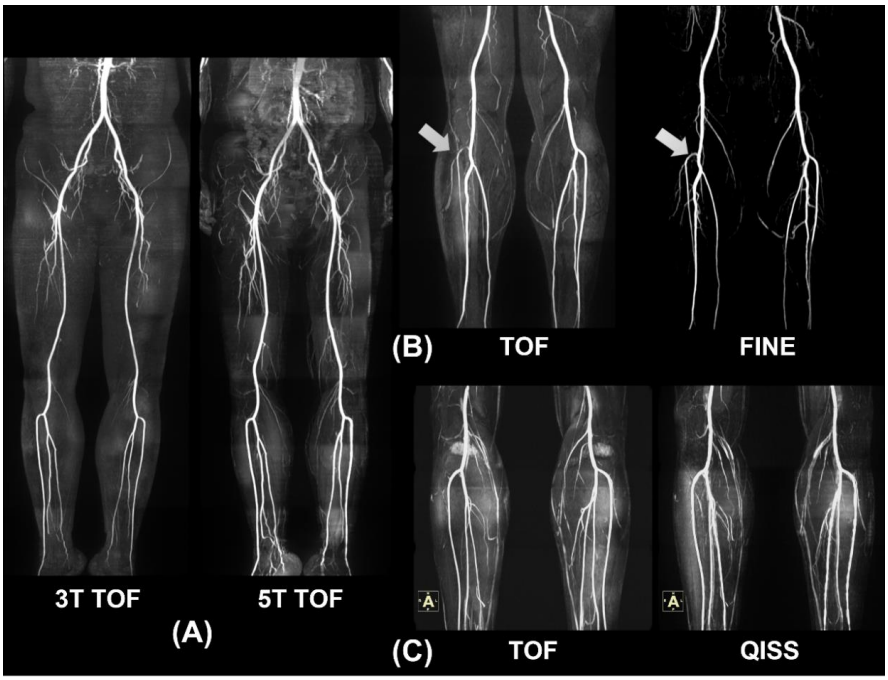

Figure 3. Examples of 5T lower limb MRA. A. Comparison of 2D TOF MIP images at 3T and 5T field strengths; B. Comparison of 2D TOF and FINE 2D, with arrows indicating missing signals in TOF; C. Comparison of 2D TOF and QISS, where the acquisition time required for QISS is one-third of that for 2D TOF. All images were acquired from healthy male volunteers aged 30-50, with each comparative image pair obtained from the same volunteer.

Figure 4. Example of 5T foot vascular imaging. Comparison of MIP images of 3D PC foot vascular imaging at 3T and 5T field strengths (same healthy volunteer, 48 years old).

4.4 Lower Limb Vessels

The vascular morphology and blood flow direction of the lower limbs generally follow a head-to-foot orientation and are relatively straight. NCE-MRA methods based on the inflow effect can achieve high-quality vascular images at ultra-high fields, such as TOF and QISS. Typically, 2D plane acquisitions in the transverse position are used to obtain strong inflow effects. During acquisitions, external ECG gating signals can be used to capture data during diastole and reduce pulsation artifacts. Figure 3A shows the performance of 2D TOF at 3T and 5T field strengths, demonstrating improved artery visualization at 5T.

The ASL method (United Imaging: FINE 2D) can achieve better background suppression by acquiring and subtracting images of arteries and veins separately. Figure 3B shows the imaging results of FINE 2D and 2D TOF in the calf, where FINE 2D shows enhanced background suppression and improved vessel delineation compared to 2D TOF.

The QISS method is another suitable NCE-MRA technique for lower limb vessels. Previous researchers have applied it to 7T but found it susceptible to B1 field issues, leading to blood signal loss and uneven image brightness (2, 3). The 5T field strength is expected to mitigate this defect. Figure 3C shows the imaging results of QISS in the calf. Compared to TOF, which completes layer acquisition every three heartbeats, QISS can reduce acquisition time from approximately 3 minutes per station to 1 minute per station using single-shot bSSFP acquisition.

Furthermore, FBI and FSD techniques based on 3D FSE or bSSFP acquisition can also be used for lower limb vascular imaging, but their application at 5T ultra-high field requires further research.

4.5 Foot Vessels

The slow blood flow in the foot presents significant challenges for NCE-MRA. TOF and QISS methods based on the inflow effect often fail to achieve ideal imaging results. Researchers have used FBI (23) and FSD (24) techniques to scan foot vessels, but these methods face challenges due to field inhomogeneity at ultra-high fields.

3D PC is a feasible technique that can achieve clear imaging of foot vessels by setting a small velocity encoding value (VENC) (25). Figure 4 shows the performance of 3D PC in the same healthy volunteer at 3T and 5T field strengths, demonstrating a significant improvement in vascular presentation at higher field strengths.

5. Conclusion

The advent of the uMR Jupiter 5T MRI platform brings new opportunities for ultra-high-field whole-body NCE-MRA research. Currently, the Jupiter 5T system preliminarily covers the full-body vascular scanning sequence. Existing research results indicate that traditional imaging techniques like TOF and PC demonstrate significantly superior vascular visualization at 5T compared to 3T (22, 25). The preliminary exploration results presented in this paper also suggest that more advanced techniques like ASL and QISS are feasible at 5T. Future research requires more in-depth studies to

validate the applicability of various NCE-MRA techniques at 5T.

However, new opportunities come with more complex technical challenges. The technical issues faced by NCE-MRA at ultra-high fields are often a double-edged sword. For example, higher field strengths enhance signal, which can improve image SNR and resolution; however, more severe B1+ and B0 field inhomogeneities at ultra-high fields impose higher demands on NCE-MRA sequence design, especially for advanced techniques like FBI and FSD. Additionally, increased tissue T1 values at ultra-high fields result in longer signal recovery times, potentially leading to reduced image T1 contrast and extended scan times. However, for NCE-MRA, this phenomenon can be utilized to achieve higher blood-to-background contrast. Therefore, selecting imaging schemes suitable for ultra-high fields based on the morphology and blood flow characteristics of specific body parts and addressing challenges like field inhomogeneity through sequence optimization, coil design, and shimming techniques are crucial for ultra-high-field whole-body NCE-MRA research.

This paper only presents example images of NCE-MRA in various body regions and preliminarily discusses the technical characteristics and feasibility of 5T ultra-high-field whole-body vascular imaging. Future research plans will combine large-sample clinical scan data to conduct in-depth quantitative evaluations of various techniques in clinical applications, providing stronger support for their widespread use in medical imaging.

6. Image/Figure Courtesy

All images are the courtesy of The Institute of Science and Technology for Brain-inspired Intelligence, Fudan University, Shanghai, China and Department of Radiology, Zhongshan Hospital, Fudan University, Shanghai, China

7. References

1. Stamm AC, Wright CL, Knopp MV, Schmalbrock P, Heverhagen JT: Phase contrast and time-of-flight magnetic resonance angiography of the intracerebral arteries at 1.5, 3 and 7 T. Magnetic Resonance Imaging 2013; 31:545–549.

2. Raval SB, Britton CA, Zhao T, et al.: Ultra-high field upper extremity peripheral nerve and non-contrast enhanced vascular imaging. PLoS ONE 2017; 12:1–20.

3. Fischer A, Maderwald S, Johst S, et al.: Initial evaluation of non-contrast-enhanced magnetic resonance angiography in patients with peripheral arterial occlusive disease at 7 T. Investigative Radiology 2014; 49:331–338.

4. Umutlu L, Maderwald S, Kraff O, et al.: New look at renal vasculature: 7 tesla nonenhanced T1-weighted FLASH imaging. Journal of Magnetic Resonance Imaging 2012; 36:714–721.

5. Metzger GJ, Auerbach EJ, Akgun C, et al.: Dynamically applied B1+ shimming solutions for non-contrast enhanced renal angiography at 7.0 tesla. Magnetic Resonance in Medicine 2013; 69:114–126.

6. Glockner JF, Takahashi N, Kawashima A, et al.: Non-contrast renal artery MRA using an inflow inversion recovery steady state free precession technique (inhance): Comparison with 3D contrast-enhanced MRA. Journal of Magnetic Resonance Imaging 2010; 31:1411–1418.

7. Edelman RR, Sheehan JJ, Dunkle E, Schindler N, Carr J, Koktzoglou I: Quiescent-interval single-shot unenhanced magnetic resonance angiography of peripheral vascular disease: Technical considerations and clinical feasibility. Magnetic Resonance in Medicine 2010; 63:951–958.

8. Yan L, Wang S, Zhuo Y, et al.: Unenhanced dynamic MR angiography: High spatial and temporal resolution by using true FISP-based spin tagging with alternating radiofrequency. Radiology 2010; 256:270–279.

9. Koktzoglou I, Meyer JR, Ankenbrandt WJ, et al.: Nonenhanced arterial spin labeled carotid MR angiography using three-dimensional radial balanced steady-state free precession imaging. Journal of Magnetic Resonance Imaging 2015; 41:1150–1156.

10. Zhu D, Li W, Liu D, et al.: Non-contrast-enhanced abdominal MRA at 3 T using velocity-selective pulse trains. Magnetic Resonance in Medicine 2020; 84:1173–1183.

11. Markl M, Frydrychowicz A, Kozerke S, Hope M, Wieben O: 4D flow MRI. Journal of Magnetic Resonance Imaging 2012; 36:1015–1036.

12. Miyazaki M, Takai H, Sugiura S, Wada H, Kuwahara R, Urata J: Peripheral MR angiography: separation of arteries from veins with flow-spoiled gradient pulses in electrocardiography-triggered three-dimensional half-

Fourier fast spin-echo imaging. Radiology 2003; 227:890–896.

13.Priest AN, Taviani V, Graves MJ, Lomas DJ: Improved artery-vein separation with acceleration-dependent preparation for non-contrast-enhanced magnetic resonance angiography. Magnetic Resonance in Medicine 2014; 72:699–706.

14.Fan Z, Sheehan J, Bi X, Liu X, Carr J, Li D: 3D noncontrast MR angiography of the distal lower extremities using flow-sensitive dephasing (FSD)-prepared balanced SSFP. Magnetic resonance in medicine 2009; 62:1523–32.

15.Li H, Priest AN, Patterson I, Graves MJ, Lomas DJ: Subtractive non-contrast-enhanced MRI of lower limb veins using multiple flow-dependent preparation strategies. Magnetic Resonance in Medicine 2019; 81:1769–1783.

16. Xu F, Zhu D, Fan H, et al.: Magnetic resonance angiography and perfusion mapping by arterial spin labeling using Fourier transform–based velocity-selective pulse trains: Examination on a commercial perfusion phantom. Magnetic Resonance in Medicine 2021; 86:1360–1368.

17.Bangerter NK, Cukur T, Hargreaves BA, et al.: Three-dimensional fluid-suppressed T2-prep flow-independent peripheral angiography using balanced SSFP. Magnetic Resonance Imaging 2011; 29:1119–1124.

18.Stafford RB, Sabati M, Mahallati H, Frayne R: 3D non-contrast-enhanced MR angiography with balanced steady-state free precession dixon method. Magnetic Resonance in Medicine 2008; 59:430–433.

19. Edelman RR, Koktzoglou I: "Push-button" noncontrast MR angiography using balanced T1 relaxation-enhanced steady-state (bT1RESS). Magnetic Resonance in Medicine 2021; 85:1248–1257.

20.Miyazaki M, Akahane M: Non-contrast enhanced MR angiography: Established techniques. Journal of Magnetic Resonance Imaging 2012; 35:1–19.

21.Miyazaki M, Isoda H: Non-contrast-enhanced MR angiography of the abdomen. European Journal of Radiology 2011; 80:9–23.

22.Shi Z, Zhao X, Zhu S, et al.: Time-of-Flight Intracranial MRA at 3 T versus 5 T versus 7 T: Visualization of Distal Small Cerebral Arteries. Radiology 2023; 306:207–217.

23. Schubert T, Takes M, Aschwanden M, et al.: Non-enhanced, ECG-gated MR angiography of the pedal vasculature: comparison with contrast-enhanced MR angiography and digital subtraction angiography in peripheral arterial occlusive disease. European Radiology 2016; 26:2705–2713.

24.Liu X, Fan Z, Zhang N, et al.: Unenhanced MR Angiography of the Foot: Initial Experience of Using Flow-Sensitive Dephasing–prepared Steady-State Free Precession in Patients with Diabetes. Radiology 2014; 272:885–894.

25.Shi Z, Li H, Zeng M: Improved Visualization for Foot MRA by Warm Water Immersion. In Proceedings of Society for Magnetic Resonance Angiography 35th Annual International Conference; 2023.

Author Biography

Dr. Hao Li
Assistant Professor
Young Associate Principal Investigator

The Institute of Science and Technology for Brain-inspired Intelligence, Fudan University, China

Dr. Hao Li has been working as an Assistant Professor at the Zhangjiang International Brain Imaging Centre, Fudan University since April 2022. He earned his PhD in Radiology from the University of Cambridge in 2020, where he continued to work as a Research Associate until March 2022. His research focuses on the advancement of MRI techniques, including non-contrast-enhanced MR angiography, quantitative MRI and whole-body MRI at ultra-high-field strengths.

Clinical evaluation of head motion correction on uMI Panorama PET/CT system

Fei Kang[1#], Zhaojuan Xie[1#], Wenhui Ma[1#], Zhiyong Quan[1], Guiyu Li[1], Kun Guo[1], Xiang Li[1], Taoqi Ma[1], Weidong Yang[1], Jing Wang[1]

[1] Department of Nuclear Medicine, Xijing Hospital, Fourth Military Medical University, Xi'an, China.

[#] These authors contributed equally to this article.

1. Introduction

Head motion (HM) during brain PET imaging poses significant challenges, introducing errors in uptake estimation and creating artifacts that compromise diagnostic accuracy. Advanced scanners, such as the uMI Panorama PET/CT (1), require minimal patient movement to achieve optimal spatial resolutions, including sub-3-mm full-width-half-maximum. In clinical settings where precise evaluations are critical for diagnosis, treatment planning, and assessing treatment responses, HM can undermine diagnostic confidence (2). Additionally, HM can lead to misalignment between PET and CT images, causing artifacts such as attenuation mismatches and localization issues. In extreme cases, significant motion blur may necessitate rescanning.

Traditional methods like frame-based image registration and hardware-based motion tracking (HMT) have limitations leading to artifacts (3-9). To address these limitations, data-driven HMC techniques have emerged (10,11). Methods like principal component analysis and centroid of distribution (COD) estimate rigid motion from PET raw data, offering software-based solutions easily integrated into clinical processes. The NeuroFocus[1] algorithm, specifically designed for the uMI Panorama PET/CT system, is a significant innovation. This system, equipped with a 189-picosecond time-of-flight (TOF) resolution and a 35-centimeter axial field of view (FOV), uses a statistics-based method developed by Revilla et al. to detect HM without parameter adjustments, accurately distinguishing COD variations caused by HM (12).

This study presents three key findings: (1) validating the precision of NeuroFocus for the uMI Panorama PET/CT system; (2) demonstrating the algorithm's effectiveness in diagnosing brain disorders; and (3) analyzing the frequency and severity of HM in clinical 18F-FDG brain studies. Further, this study marks the first large-scale clinical application of an HMC algorithm with short PET acquisition times.

2. Materials and Methods

2.1 Validation study data acquisition

The study involved 15 volunteers who participated in a prospective validation process. Each participant underwent a 3-minute brain PET scan on a single bed, conducted approximately 52.2±9.2 minutes after the administration of 18F-FDG. During the first scan, the volunteers were instructed to remain completely still ("NoMo"). For the second 3-minute scan, participants were directed to perform specific translational and rotational movements ("InstrMo"). Prior to each PET scan, a CT scan was performed for attenuation correction (AC). Additionally, MR images, including T1-weighted, contrast-enhanced T1-weighted, and T2-weighted images, were collected for each participant on the same day. The study, conducted at Xijing Hospital in Xi'an, China, was approved by the Ethics Committee of the Medical University in accordance with the revised Declaration of Helsinki (1964). All participants provided written informed consent.

2.2 Evaluation study data acquisition

A retrospective analysis was conducted on 302 clinical single-bed brain 18F-FDG scans, each lasting 3.0 minutes and performed 75.0±19.9 minutes after injection. The scans were classified into two groups: those without head motion correction (NMC) and those with head motion correction (HMC). Each study included a CT scan for attenuation correction (AC), though no MR images were obtained. Detailed patient information is provided in Table 1. The institutional review board approved this retrospective analysis, waiving the requirement for informed consent.

[1]This product may not be available for such sales in some countries.

2.3 Head motion correction algorithm

The head motion correction (HMC) algorithm involves three essential stages: motion detection, estimation, and correction. Motion was detected using the Center of Distribution (COD) algorithm, which produced a COD trace at 1 Hz intervals. By distinguishing motion-induced variations from statistical count variations in the COD trace, the study was divided into consecutive motion-free frames (MFFs), separated by motion time points. Frames shorter than 5 seconds were discarded. Motion estimation involved rigidly registering subsequent MFFs to a reference frame (the first MFF) using mutual information difference as the similarity metric. The first MFF was assumed to align spatially with the CT scan, ensuring no movement occurred between the CT and PET scans. The transformation matrix T(i) was used to estimate the i-th MFF, and the CT attenuation map was adjusted using the inverse of T(i) to create a matched attenuation map. Ordered subset expectation maximization with attenuation correction (OSEM-AC) was applied to each MFF, and all OSEM-AC MFFs were then transformed back to the reference frame and summed to produce the final HMC image. Reconstructions used a voxel size of 1.20×1.20×1.45 mm^3.

2.4 Evaluation

For the validation dataset, FreeSurfer was used to segment paired T1-weighted MR images into 109 brain regions of interest (ROIs), which were then resliced to match individual PET scans and grouped into 11 gray matter (GM) regions: amygdala, caudate, cerebellum cortex, frontal, hippocampus, insula, occipital, parietal, putamen, temporal, and thalamus. The percentage differences in standard uptake value (SUVmean) between the instructed motion (InstrMo) and no motion (NoMo) scans, as well as between InstrMo with HMC and NoMo, were reported for each GM region.

For the evaluation dataset, brain ROIs were created using an in-house CT-based segmentation algorithm. After registering with the MNI brain MRI template, 116 AAL brain ROIs were mapped to individual CT spaces. Cerebellum uptake and SUVmean ratio images were calculated, and a threshold was applied to create a binary GM mask. The cerebellum ROI was used to calculate cerebellum uptake on the reference frame using OSEM with AC. The SUVmean ratio image of the reference frame was generated with cerebellum uptake as the reference value, and a threshold of 1.0 was applied to create a binary GM mask. Overlapping regions between the mask and the 116 ROIs were used to refine GM regions, which were then merged into 11 regions based on the AAL definition. Supplemental Figure 1 illustrates the process for generating brain ROIs.

To quantify head motion, the distance traveled by each ROI was calculated through image registration, and the distances traveled by all 116 ROIs during different MFFs were averaged per minute. The average motion amplitude for the 11 combined GM ROIs was calculated by averaging the distances moved by the sub-ROIs, with reported distances of movement documented for each case study.

3. Results

3.1 Prospective validation study

Figure 1 presents three cases from the validation study, where significant image blurring is observed in the InstrMo scans due to head motion (HM). After applying the head motion correction (HMC), the images show a marked improvement in contrast and resolution, closely resembling the NoMo scans. The corresponding MR images also clearly depict anatomical structures in line with the NoMo studies. The detailed clinical diagnoses for these cases are provided in the caption of Figure 1.

Figure 2 highlights a patient from the evaluation study who was diagnosed with angioimmunoblastic T-cell lymphoma. This figure displays two axial slices from CT, NMC, and HMC images. The HMC images reveal areas of annular hypermetabolism with central hypometabolism in the left parietal lobe, as indicated by arrows, which were mostly blurred and indistinct in the NMC images due to HM.

In Figure 3, a case is shown where focal hypometabolism in the left thalamic and basal ganglia regions is clearly visible in the HMC image, while these regions are obscured by HM in the NMC image, making them undetectable.

Table 2 provides a quantitative analysis of the 15 validation studies, showing the SUVmean percentage error for each region of interest (ROI). The InstrMo scans generally demonstrated significant negative differences (-10%) with considerable variation across brain regions compared to NoMo scans. For example, the frontal region had a larger discrepancy (-16%) compared to the amygdala. After applying HMC, the differences were much smaller (around -1%) with

reduced variability (3%), indicating successful compensation for HM across all validation studies.

3.2 Retrospective evaluation study

Figure 4 shows two clinical evaluation studies of patients with suspected nervous system lymphoma and thalamic lacunar infarction. Significant HM was detected in the initial PET scans, which prompted the technician to recall the patients for re-scanning. During the second scans, both patients remained still. Remarkably, applying HMC to the initial scans resulted in images comparable to the re-scans, demonstrating the practical benefit of HMC in reducing the need for repeat scans due to HM.

Figure 5 illustrates a case of a patient with non-small cell lung cancer who exhibited significant involuntary head movements during both the initial and re-scan. Without advanced correction methods, these scans were not suitable for clinical diagnosis. However, after applying HMC, notable improvements in image resolution and contrast were observed in both sets of scans. The corrected images revealed reduced metabolic activity and swelling around a possible brain metastasis, which was only identifiable after using HMC.

In the evaluation study, Table 3 presents the numerical results of SUVmean changes across different brain regions after applying HMC. Participants were categorized into two groups based on the extent of head motion: small motion and large motion, using a 5% threshold in SUVmean change in the frontal lobe after HMC. In the small motion group, the average motion distance was relatively consistent across brain regions (2.4 mm) with low variability (1.9 mm). In contrast, the large motion group showed increased motion distances in all regions of interest (ROIs), ranging from 7.3 mm in the cerebellum to 15.0 mm in the frontal region, with significantly higher mean motion amplitude and variability (10.9 mm ±5.9 mm).

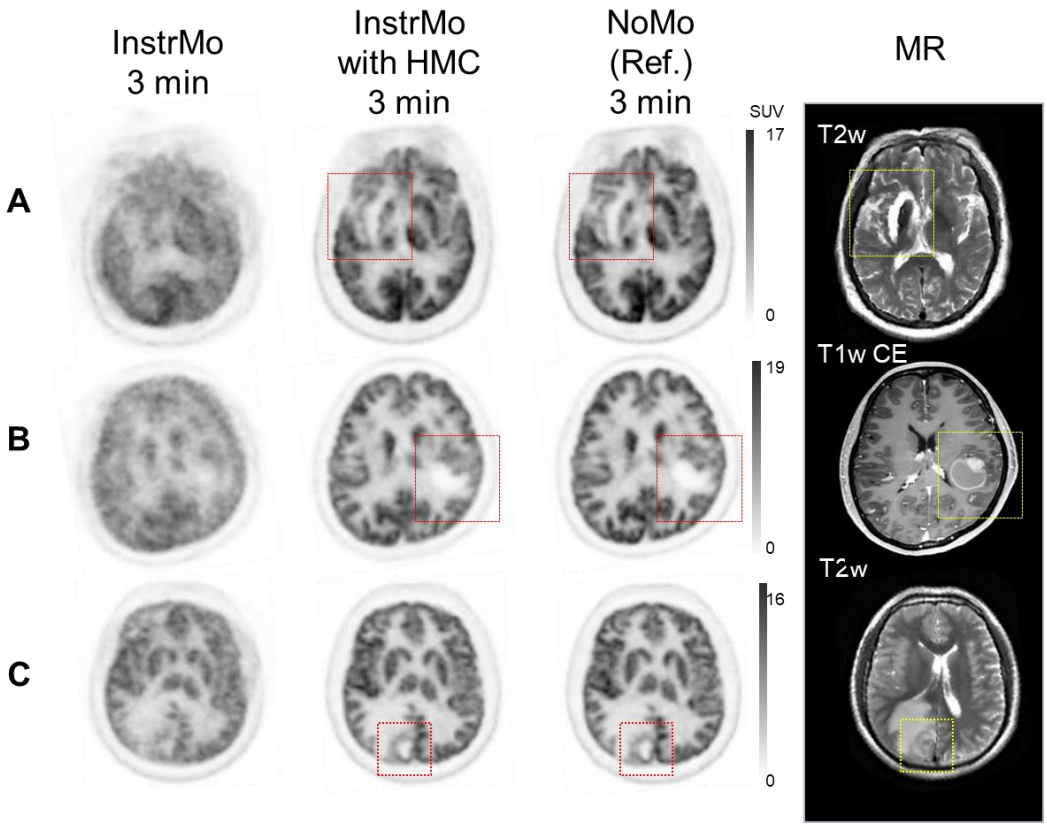

Figure 1. PET images from three distinct cases in the validation study, comparing scans with instructed motion (InstrMo), head motion correction (HMC), no motion (NoMo), and MRI. A) encephalomalacia/gliosis of the right basal ganglia and the right temporal lobe, and mild ex-vacuo dilatation of the right lateral ventricle in a geriatric patient with a history of right middle cerebral artery territory infarct; B) hypermetabolic nodules on PET aligns with nodular wall thickening in a cystic-appearing lesion observed in MR imaging associated with brain metastases from small-cell lung cancer; C) an annular hypermetabolic cerebral syphilitic gumma with surrounding edema in the right parietal occipital lobe. Averaged/maximal moving distance of the frontal lobe: 8.5/26.3 mm (Case A), 9.5/17.3 mm (B) and 19.0/54.2 mm (C). Injected dose/post injection/duration/body

weight: A) 273.8 MBq/56.1 min/3 min/69 kg, B) 214.6 MBq/65.6 min/3 min/56 kg and C) 270.1 MBq/67.8 min/3 min/70 kg. InstMo: instructed motion; HMC: instructed motion after head motion correction; NoMo: no motion repeat scan.

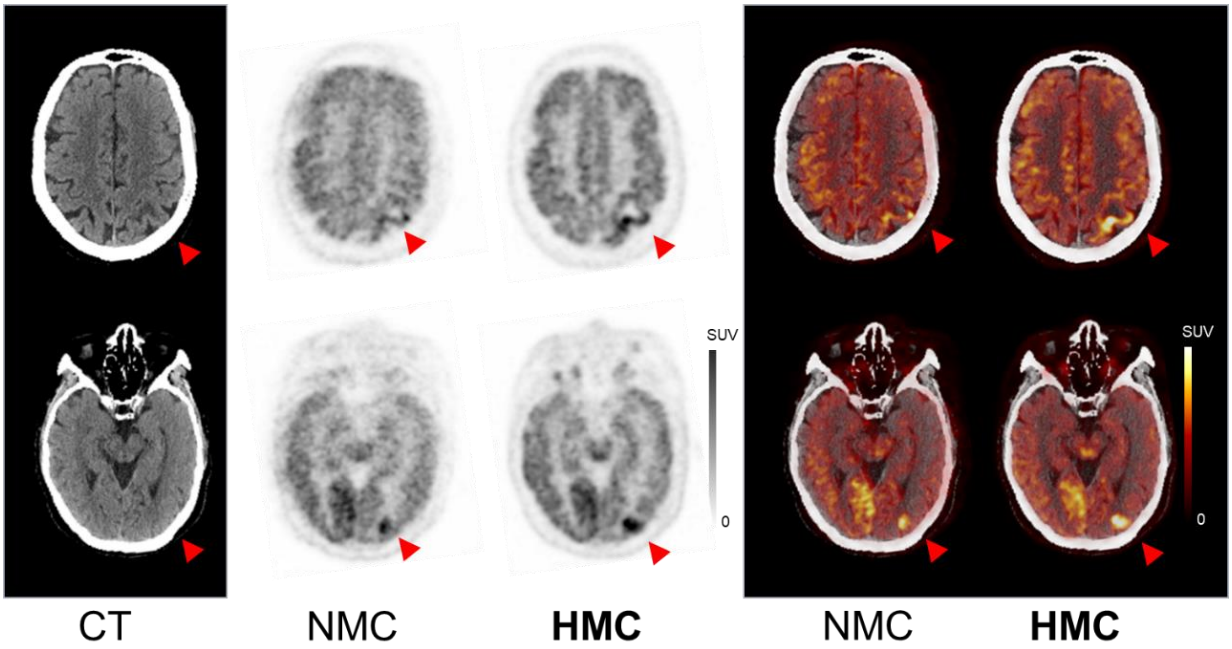

Figure 2. CT, PET and PET-CT with motion before and after HMC in a case of angioimmunoblastic T-cell lymphoma (AITL) suspected with cerebral infiltration due to acute onset of neurological symptoms. Motion blur and mis- registration were corrected after HMC. Areas of annular hypermetabolism with central hypometabolism in the left parietal lobe were revealed after HMC. Injected dose 251.6 MBq, post injection 90 min, frame duration 3 min single bed, body weight 65 kg. Averaged/maximal moving distance of the frontal lobe: 10.9/18.8 mm. NMC: no motion correction; HMC: head motion correction.

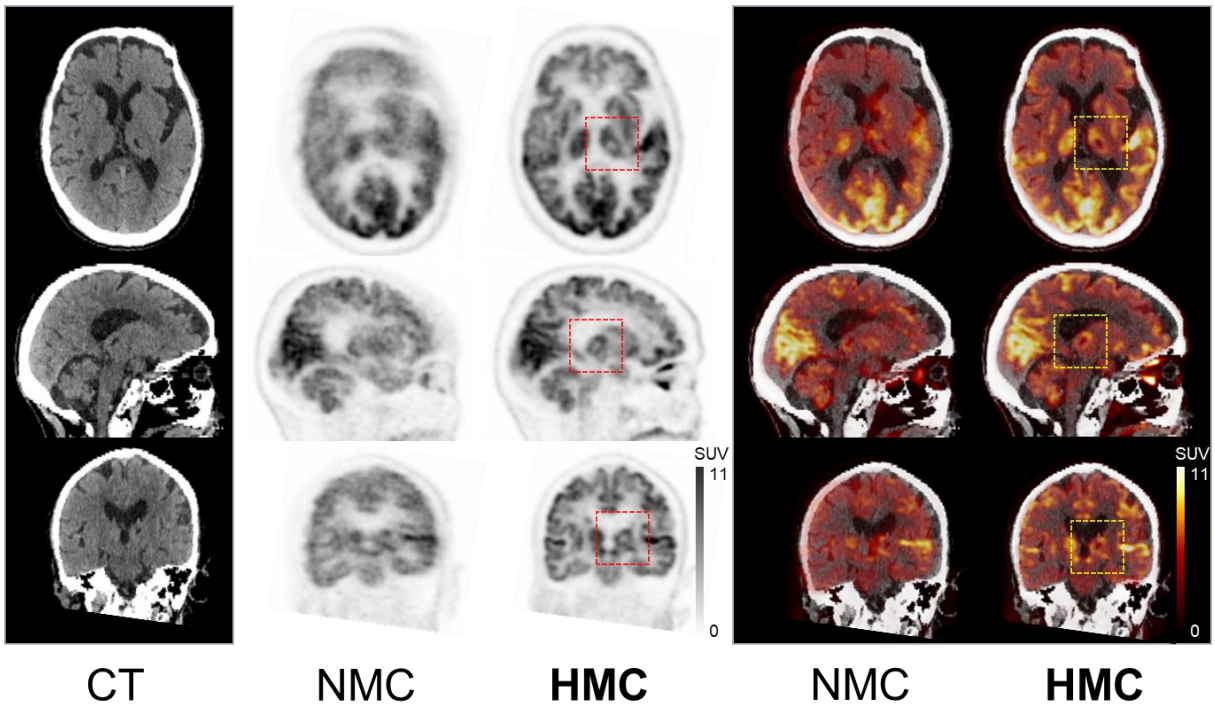

Figure 3. CT, PET and PET-CT with motion before and after HMC in a case of focal hypometabolism were observed in the left thalamic and basal ganglia region after HMC. Injected dose 229.4 MBq, post injection 69 min, frame duration 3 min, body weight 48 kg. Averaged/maximal moving distance of the frontal lobe: 13.7/25.4 mm. NMC: no motion correction; HMC: head motion correction.

4. Discussions

In this study, we performed both a prospective validation and a retrospective evaluation of the HMC algorithm from the uMI Panorama PET/CT scanner. The prospective validation included fifteen studies where participants were instructed to move their heads, while the retrospective evaluation examined 302 clinical brain studies using 18F-FDG, each with a 3-minute acquisition time. Results from the validation study showed that the HMC algorithm was highly effective, with an average quantitative error of less than 1% compared to scans without motion. In the retrospective evaluation, approximately 12% (38 out of 302) of clinical brain studies experienced significant head movement, underscoring the necessity of HMC. The effectiveness of the HMC algorithm was demonstrated across various brain diseases and clinical conditions, confirming its value in real-world applications. The reconstruction time for instructed motion studies averaged 11.0 ± 1.1 minutes, and reconstructions were submitted after acquisition. Across the evaluation studies, an average of 2.0 ± 9.7 seconds of data was discarded per case.

The European Association of Nuclear Medicine (EANM) guidelines emphasize the importance of neurological PET imaging in diagnosing cognitive and movement disorders, localizing epileptic foci, detecting neuro-infections, and assessing brain tumors. The guidelines recommend using small voxel reconstructions to improve brain structure visualization, which typically requires longer acquisition times to maintain adequate signal-to-noise ratios. For standard 18F-FDG brain scans, the guidelines suggest 10-15 minutes per bed position for scanners with short axial fields of view (FOV), with non-18F-FDG scans potentially requiring even longer times (up to 20-30 minutes per bed). However, using the high-sensitivity uMI Panorama scanner, we completed each clinical scan in just 3 minutes, maintaining sufficient image quality for diagnostic use. Despite the short scan duration, 12% of patients exhibited significant head movement, indicating that longer-duration scans may require an even greater reliance on HMC.

The introduction of HMC in PET imaging has significantly enhanced image quality and delivered practical benefits, including fewer rescan needs, reduced patient wait times, and improved comfort from repeated CT scans. The reduction in rescans also improves patient scheduling, streamlines workflows, and reduces the workload for healthcare professionals, optimizing resource management. HMC is particularly beneficial for patients who struggle to remain still during scans, reducing the need for tight head restraints or sedation, which improves both patient comfort and clinical efficiency.

This paper reviews key research efforts on HMC in PET imaging, comparing them to our proposed data-driven approach. One alternative is marker-less motion tracking using optical cameras. Spangler-Bickell et al. (2020) demonstrated this technique by attaching an optical camera to a PET/MR system's head coil, tracking head movement without markers using a curved forehead marker. Zeng et al. (2021) developed a marker-less system using stereovision cameras and infrared structured light to capture facial surfaces for motion tracking. Other researchers, such as Olesen and Kyme, have explored similar approaches, but these methods can be affected by facial expression changes and lack of thorough validation. Another approach used Microsoft's Kinect® system to track head motion, and recent studies by Zeng et al. (2021) applied neural networks to estimate motion between short frames, speeding up motion estimation. Further, deep learning techniques have been used to enhance PET image quality by generating high-count images from low-count data, which improves registration accuracy. Rezaei et al. (2018) proposed estimating rigid motion parameters using inertia tensors from TOF back projections. Each method offers distinct strategies for addressing HMC challenges in PET brain imaging, reflecting ongoing, diverse efforts in this critical area.

In conclusion, some limitations of the current HMC algorithm must be noted: 1) It is less effective for dynamic PET studies, as it does not track physiological changes over time; 2) It cannot correct motion between PET and CT acquisitions, leading to potential attenuation-related artifacts; and 3) It cannot correct continuous motion, such as tremors in

Parkinson's patients, due to its frame-based design. These limitations highlight the need for continuous advancements and innovations in HMC technology to improve the precision and utility of PET imaging.

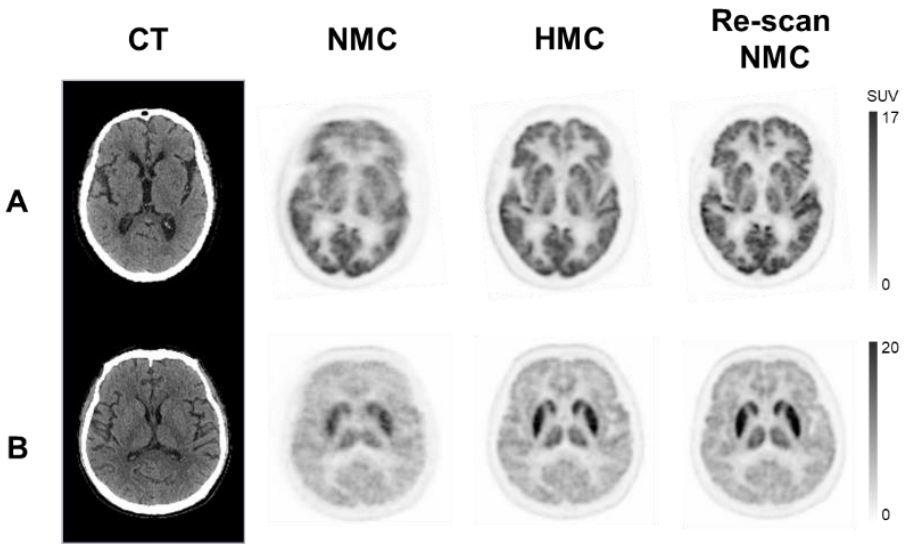

Figure 4. Comparison between PET with motion (NMC), after HMC and re-scan with minimal motion. Axial CT, PET with motion, with HMC, re-scan with minimal motion show A) hypometabolic foci in left thalamic indicating lacunar infarcts; B) bilateral hypermetabolism in the thalami and striatum in a patient with suspected nervous system lymphoma. Both HMC images are comparable to the re-scan images. A) Injected dose 266.4 MBq, post injection 71 min, frame duration 3 min, body weight 65 kg; B) Injected dose 366.3 MBq, post injection 66 min, frame duration 3 min, body weight 80 kg. Averaged/maximal moving distance of the frontal lobe: 9.6/47.2 mm (case A) and 10.0/16.0 mm (case B). NMC: no motion correction; HMC: head motion correction.

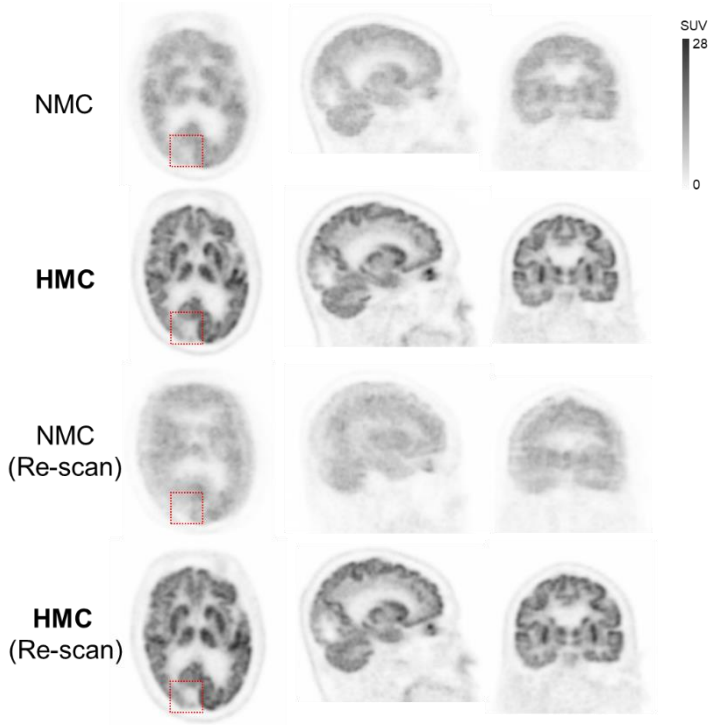

Figure 5. HMC and re-scan in cases with involuntary head movements. Images were corrupted by involuntary head motion in both the initial PET scan and the re-scan (NMC). Spatial resolution and contrast were significantly improved after HMC. The dotted box indicates the region of hypometabolic edema surrounding a suspected metastatic lesion in the occipital lobe in a patient with non-small cell lung cancer revealed after HMC. Injected dose 314.5 MBq, post injection 1st scan/re-scan 61/69 min, frame duration 3 min, body weight 77 kg. Averaged/maximal moving distance of the frontal lobe: 5.0/12.6 mm (1st scan) and 12.1/27.7 mm (re-scan). NMC: no motion correction; HMC: head motion correction.

Table 1. SUVmean change from NMC after HMC for the evaluation study (mean ±standard deviation (SD)) and mean motion distance for each brain region. NMC: no motion correction; HMC: head motion correction.

	Validation (w. MR)	Evaluation (w.o. MR)
Total participants	15	**302**
Age	34.1±13.1	**58.2±14.4**
Male	6	**171**
Female	**9**	**131**

Table 2. Validation study: % error in SUVmean as compared to the NoMo study. InstrMo: instructed motion; HMC: head motion correction

ROI	NoMo SUVmean	InstrMo (% error)	InstrMo with HMC (% error)
Amygdala	4.4±0.5	-4.3±4.7	**-0.1±1.8**
Caudate	6.6±1.2	-14.9±8.4	**-2.8±5.4**
Cerebellum	5.6±0.8	-5.6±3.2	**-2.2±1.5**
Frontal	6.8±0.9	-16.3±5.3	**-1.0±3.8**
Hippocampus	4.9±0.7	-2.4±5.3	**0.7±4.4**
Insula	5.6±0.7	-5.0±3.6	**-0.2±2.8**
Occipital	7.9±1.1	-13.9±3.7	**-3.1±4.2**
Parietal	6.6±0.9	-14.1±4.7	**0.5±3.6**
Putamen	7.3±1.3	-12.1±7.7	**-0.3±2.2**
Temporal	6.0±0.7	-11.3±5.8	**-0.1±3.7**
Thalamus	6.4±0.9	-11.1±4.8	**-0.2±1.4**
Mean average	6.2	-10.1	**-0.8**
SD average	**0.9**	**5.2**	**3.2**

Table 3. . SUVmean change from NMC after HMC for the evaluation study (mean ±standard deviation (SD)) and mean motion distance for each brain region. NMC: no motion correction; HMC: head motion correction.

	Small motion (N=264)		Large motion (N=38)	
ROI	**Mean motion distance / mm**	**SUVmean change / %**	**Mean motion distance / mm**	**SUVmean change / %**
Amygdala	2.5±1.9	0.4±2.6	11.8±6.3	**19.9±20.8**
Caudate	2.6±2.0	0.6±2.6	12.7±7.0	**22.9±13.7**
Cerebellum	2.1±1.7	-0.2±0.7	7.3±3.9	**2.9±3.7**
Frontal	2.9±2.0	0.3±1.3	15.0±8.1	**12.9±8.3**
Hippocampus	2.3±1.8	-0.3±1.4	10.1±5.3	**10.6±9.0**
Insula	2.6±1.9	0.1±1.1	13.0±7.0	**10.0±6.2**
Occipital	2.2±1.7	-0.2±0.7	6.7±4.4	**2.9±3.9**
Parietal	2.4±1.8	-0.0±0.8	9.5±5.2	**6.8±6.0**

Putamen	2.5±1.9	0.3±1.3	12.4±6.7	**12.2±10.4**
Temporal	2.5±1.8	0.1±1.0	11.8±6.2	**10.0±8.1**
Thalamus	2.2±1.8	-0.1±0.8	9.9±5.3	**8.2±7.8**
Mean average	**2.4**	**0.1**	**10.9**	**10.9**
SD average	**1.9**	**1.3**	**5.9**	**8.9**

5. Conclusion

A clinical study was conducted with fifteen participants to assess the accuracy of the NeuroFocus HMC algorithm on the uMI Panorama PET/CT system, using 18F-FDG in the evaluation process. During validation, where participants were instructed to perform head movements, the post-HMC standardized uptake value (SUV) error was found to be minimal, averaging -1±3% across all brain regions and participants. This represents a significant improvement from the previous error rate of -10±5% before applying HMC. In a broader analysis of 302 participants, approximately 12% of short-duration (3-minute) clinical brain scans showed substantial issues requiring correction. The HMC algorithm demonstrated strong efficacy in mitigating HM across various brain disorders, highlighting its potential for clinical use in brain research involving 18F-FDG.

6. Acknowledgement

The authors extend their gratitude to Chen Xi, Yue Li, Hao Liu, and Lei Shi for supporting NeuroFocus software and data acquisition. Special thanks are due to Enette Mae Revilla and Duo Zhang for manuscript editing. The authors thank Bingbing Zhao, Wenjun Yu, and Fenggang Jia for their support with the image processing software.

7. References

1. Li G, Ma W, Li X, Yang W, Quan Z, Ma T, Wang J, Wang Y, Kang F, Wang J. Performance Evaluation of the uMI Panorama PET/CT System in Accordance with the National Electrical Manufacturers Association NU 2-2018 Standard. J Nucl Med. 2024 Feb 22.
2. Polycarpou I, Soultanidis G, Tsoumpas C. Synergistic motion compensation strategies for positron emission tomography when acquired simultaneously with magnetic resonance imaging. Philos Trans A Math Phys Eng Sci. 2021;379:20200207.
3. Rahmim A, Dinelle K, Cheng JC, et al. Accurate event-driven motion compensation in high- resolution PET incorporating scattered and random events. IEEE Trans Med Imaging. 2008;27:1018- 1033.
4. Picard Y, Thompson CJ. Motion correction of PET images using multiple acquisition frames. IEEE Trans Med Imaging. 1997;16:137-144.
5. Montgomery AJ, Thielemans K, Mehta MA, Turkheimer F, Mustafovic S, Grasby PM. Correction of head movement on PET studies: comparison of methods. J Nucl Med. 2006;47:1936-1944.
6. Herzog H, Tellmann L, Fulton R, et al. Motion artifact reduction on parametric PET images of neuroreceptor binding. J Nucl Med. 2005;46:1059-1065.
7. Fulton RR, Meikle SR, Eberl S, Pfeiffer J, Constable C, Fulham MJ. Correction for head movements in positron emission tomography using an optical motion tracking system. IEEE Nuclear Science Symposium. Vol 3; 2000.
8. Costes N, Dagher A, Larcher K, Evans AC, Collins DL, Reilhac A. Motion correction of multi-frame PET data in neuroreceptor mapping: simulation based validation. Neuroimage. 2009;47:1496-1505.
9. Bloomfield PM, Spinks TJ, Reed J, et al. The design and implementation of a motion correction scheme for neurological PET. Phys Med Biol. 2003;48:959-978.
10. Thielemans K, Schleyer PJ, Dunn JT, Marsden PK, Manjeshwar RM. Using PCA to detect head motion from

pet list mode data. IEEE Nuclear Science Symposium and Medical Imaging Conference; 2013.

11.Schleyer PJ, Dunn JT, Reeves S, Brownings S, Marsden PK, Thielemans K. Detecting and estimating head motion in brain PET acquisitions using raw time-of-flight PET data. Phys Med Biol. 2015;60:6441-6458.

12.Revilla EM, Gallezot JD, Naganawa M, et al. Adaptive data-driven motion detection and optimized correction for brain PET. Neuroimage. 2022;252:119031.

Author Biography

Prof. Jing Wang

Director, Department of Nuclear Medicine

Xijing Hospital, China

Prof. Jing Wang is a distinguished professor and chief physician, currently serving as Director of the Department of Nuclear Medicine at Xijing Hospital and a graduate advisor at the Fourth Military Medical University. With a medical degree and Ph.D. from the Fourth Military Medical University, Prof. Wang has over 30 years of experience in nuclear medicine, specializing in oncological molecular nuclear imaging and multimodal imaging applications. She has led numerous high-impact research projects, including key National Natural Science Foundation of China (NSFC) projects, and published over 50 SCI-indexed articles, with her work earning notable recognition, such as the 2018 First Prize for Science and Technology Progress in Shaanxi Province.

Prof. Wang holds several prominent professional roles, including Chair-elect of the Chinese Society of Nuclear Medicine and Expert Consultant for the Central Military Commission's Health Committee. Her contributions to nuclear medicine have been widely recognized, with accolades like the "Chinese Nuclear Medicine Physician Award" and the “Outstanding Physician for Exceptional Achievements” award. She is also Deputy Editor of the Chinese Journal of Nuclear Medicine and Molecular Imaging and has authored multiple textbooks, advancing both clinical practice and research in nuclear medicine.

Unveiling the Mind: Journeying through Brain PET with Dr. Richard E. Carson

A United Imaging article by Edwin K. Leung, Ph.D.

E: Dr. Carson, it's a pleasure to have you with us today as we delve into the fascinating world of brain PET imaging. Before we start, congratulations to you and your colleagues for winning the 2024 SNMMI Image of the Year, and for the featured article in the Journal of Nuclear Medicine utilizing the uNeuroEXPLORER[1] system.

R: Thank you so much! It was very exciting to receive the Image of the Year award and really a thrill to be able to share these amazing images with our field.

E: PET imaging is largely utilized today in oncology to detect cancer, despite that early PET imaging applications focused on the brain. Why do you think there was such a shift?

R: I think there are 2 key factors to consider here. Certainly, the brain was a good target, especially for the early generations of PET systems due to the challenges of imaging in the body. Also, there was a large number of molecules already well defined and of interest – especially from the pharmaceutical industry. So, there were many relevant tracers that were broadly relevant in many brain disorders, and the instrumentation at the time was sufficient to image those targets.

The big switch occurred with the advent of PET/CT, when it became evident that FDG PET was incredibly useful in all aspects of tumor assessment. Simultaneously, the clinical utility of PET improved significantly when combined with CT; this was a turning point in the field. At the same time, this shift has led to huge benefits for brain PET, because the clinical demand in oncology has driven significant progress in the quality of PET instrumentation along with the increased availability of cyclotrons and the production of radiopharmaceuticals.

So, we wouldn't have been able to advance brain PET as far as we have without this incredible push for oncology thanks to PET/CT.

E: Many of our colleagues understand that you and your team at Yale have utilized the HRRT, a dedicated brain PET scanner for research over the last 2 decades or so. What were some benefits and limitations you have found with earlier dedicated brain PET systems compared to its clinical whole-body PET/CT counterparts for brain PET imaging?

R: The HRRT was unique – it was meant to be an experimental research system, trying to push the envelope of what could be done with PET based on the technological capabilities of the mid to late 1990s – specifically, what we could do to handle the effects of depth of interaction (DOI).

We knew that as you move closer and closer to the detectors, if you don't measure the DOI, i.e., where the event occurs within the crystal, you're going to increase the blur in the images. Interestingly, in systems at that time – even between the center of the brain and the cerebral cortex on the edge – you have a noticeable loss of resolution. That motivated the design of the HRRT in order to push the envelope in terms of absolute resolution and uniformity of resolution in the brain.

There were 17 HRRT systems manufactured and distributed across sites all around the world, to experts focusing on high resolution brain PET utilizing interesting radiopharmaceuticals. What we all found was that we could do some exceptional research with interesting clinical applications in neuropsychiatric disorders, because the HRRT provided us much better resolution than any system that was available until very, very recently [the uNeuroEXPLORER].

So, we were able to combine great resolution from the HRRT images with specific radiopharmaceuticals – for example – targeting dopamine, norepinephrine, and serotonin receptors and transporters. Many interesting clinically relevant studies were performed with a wide range of dedicated brain-related molecules.

The HRRT allowed us to move forward in terms of

[1] This product is not available for sale in the U.S. for clinical uses and also may not be available for such sales in other countries.

understanding both the brain patterns of individual patients as well as characterizing disease etiology. The HRRT also accelerated the collaborations of PET researchers with the pharmaceutical industry as they understood that they could measure for a particular drug molecule – did the drug reach the brain target, at what levels, and whether it was reaching a point of significant clinical utility without producing adverse effects.

So, it was an exciting period of time – and the HRRT paved the way because of its high resolution and its ability to make these measurements in relatively small structures compared to clinical systems at the time.

E: A lot of folks today are aware of the EXPLORER total-body PET/CT system [now known as the uEXPLORER system] that was co-developed between Dr. Ramsey D. Badawi and Dr. Simon R. Cherry from UC Davis, and United Imaging. And now, you are collaborating with UC Davis and United Imaging to develop the NeuroEXPLORER (NX) dedicated brain PET/CT system [now known as the uNeuroEXPLORER system]. Can you please shed some light on what made you interested in collaborating with United Imaging?

R: The NX journey started back in 2018. As a professor at Yale, I have the opportunity to take sabbaticals from time to time. At that time, I took a sabbatical in the greater San Francisco Bay Area – and my major destination was UC Davis to visit Simon and Ramsey [to see the uEXPLORER]. We had many excellent discussions – including – what was possible for next-generation brain PET system.

Earlier, I mentioned the good features of the HRRT, but its biggest weakness was its sensitivity. The HRRT could identify small structures, but it did not collect enough counts to be able to measure these structures with good reliability. Of course, one of the huge advantages of the uEXPLORER total-body system is its incredible sensitivity.

So, how could we get the best of both worlds – ultra-high resolution – better than the HRRT, and high enough sensitivity to use it? Achieving the right balance led to many wonderful discussions.

Simon and Ramsey have had a very successful relationship with United Imaging. They had the experience that United Imaging was able to deliver on time and deliver what was promised. Therefore, it was the natural next step to reach out to United Imaging to begin the NX collaboration.

We were able to write a grant proposal targeting the NIH BRAIN Initiative, and in September 2019 we submitted the proposal. About one year later, we were awarded that grant. And so, we were all very excited to actually begin the effort of building the new uNeuroEXPLORER system, testing that system, and taking advantage of the combined expertise in the development of novel systems – the system design, optimization, and evaluation skills brought by UC Davis combined with our experience with brain PET imaging at Yale.

E: The one aspect that most people tend to notice at first glance about the uNeuroEXPLORER system is that it has a split PET/CT gantry configuration, in which the CT and the PET gantries are separated by 80 cm. Can you tell us why there is such a gap?

R: One very important part of the kind of brain imaging we do is to also measure the activity in the subject's blood. When you perform an injection of a radiopharmaceutical, how much activity reaches the brain is going to depend on how the rest of the body handles the tracer.

For example, if your liver metabolizes the radiopharmaceutical faster or slower, that's going to affect your brain content. Also, your body mass is a major factor – that's why SUV is normalized by body mass. With that in mind, we needed to have room between the PET and CT gantries so that our technologists and nurses could easily access the subject's arms, so that we perform the injection in one arm and perform arterial sampling in the other arm.

Also, we fully expect – and I think there's already quite a lot of preliminary data – that eventually we may not need a CT for brain PET imaging. So, from a manufacturing viewpoint, it was advantageous to have a separate PET gantry because synthetic CT for PET attenuation correction is becoming more and more widespread – mostly with deep learning methods. But there are also other approaches such as using the lutetium background, that are able to synthesize an appropriate CT for the purpose of PET attenuation correction. It remains to be shown if these methods are as good as what we might need clinically, i.e., CT images.

So, I think the separate gantry setup is well-suited for the long-term goal of the uNeuroEXPLORER system as a standalone PET – something smaller without the CT there. Also, when we're thinking about utilizing the high sensitivity to reduce injected dose, removing the CT will be very

important – for example – in pediatric imaging.

E: Many people have commented that the uNeuroEXPLORER has a somewhat large bore, at 50 cm, for a dedicated brain scanner. What advantages does a large bore provide compared to a more conventional bore for brain PET (on the scale of 20 cm)?

R: There is a lot of interest right now in other geometries for dedicated brain systems such as helmet designs, trying to be as close to the head as possible. A smaller bore would increase the raw sensitivity of the system.

The question is whether such systems will have all the advantages of the uNeuroEXPLORER. For example, can those systems produce the same time-of-flight advantage, which produces a large boost in effective sensitivity?

In addition, what we really wanted to enhance with a larger bore was patient comfort, especially in the research world where we perform long scans. Having a very tight bore for what could be 90 min or 2 h of scanning could produce a level of claustrophobia that might not be acceptable.

Being able to position the patient's neck comfortably – especially for our older patients – is crucial. We also believe that our ability to measure head motion is much better with a bigger bore. This larger bore was also an advantage since it allowed us to test the United Motion Tracking (UMT) system on an existing clinical system (which also has a larger bore) starting 2 years before the uNeuroEXPLORER arrived at Yale, and we've gained a lot of good experience in learning how to operate and optimize the UMT system.

E: Speaking of patient comfort, what are your thoughts on brain PET system designs in which the patient is sitting upright at a slight angle?

R: Several of these designs have been presented at SNMMI over the years, and there are certainly tremendous advantages for patients who can remain comfortable when sitting and leaning back. Upright designs can be very relevant for applications that just require a short scan, such as in Alzheimer's Disease (AD), Parkinson's Disease (PD), and other disorders where a short scan is paired with a well-established tracer.

So, I think there is merit and relevance to upright designs, and we look forward to seeing more data in the coming years to understand the relative advantages of that design in terms of patient comfort. I think these upright designs are focused on a different type of application than our focus with uNeuroEXPLORER. For example, if you utilize the helmet geometry to provide sensitivity, you cannot readily have a long axial field of view – otherwise the scanner bore will be right in front of the patient's face, and that's never comfortable for long scanning periods.

E: What were some additional distinct aspects and design considerations you had when developing the uNeuroEXPLORER system with United Imaging?

R: I think the biggest factor is the great DOI. The ability to measure where in the detector the event occurs so that you can more correctly position the line of response makes a huge difference with regards to the accuracy of event localization, both for in-plane and axial parallax effects. This is a critical feature for any system that targets ultra-high resolution.

So, DOI was a critical design factor right from the beginning. It did not allow us to produce ultra-small crystals, but I think based on the results that we've have, it is clear that the uNeuroEXPLORER is providing us with exceptional resolution. This approach also impacts the time-of-flight capability of the system. Our slightly larger crystals (compared to ultra small crystals) mean more light output which is needed to obtain a very good time of flight measurement, at 236 ps. The systems that currently have the best time of flight values generally have larger crystals, which leads to resolution tradeoffs.

We are very satisfied with the balance of sensitivity and resolution that has been achieved. We were targeting a 10-fold net sensitivity increase from the HRRT with smaller crystals, longer axial field of view, and time-of-flight. And so far, the data are showing that we are hitting these targets.

E: The time between the funding notification of the NX project to the imaging of the first human subject took under 2.5 years. What made this rapid progress possible?

R: I think the rapid progress can certainly be attributed to the great discussions and planning that we did during the writing of the NIH grant. There is always that waiting period after the submission of a grant when you're not making much progress because the funding has not yet arrived. But

honestly, the relationship with United Imaging was absolutely the key. United laid out the manufacturing timeline and basically finished the system on time. By far, the biggest delay was the time for renovation of the scanner room at Yale.

I also think that all the ongoing discussions within the NX consortium were essential. We were trying to anticipate what kind of problems we would have and what surprises there might be; this is all part of building a new system. We had lots of discussions on whether there would be issues related to cooling, for example, and just really focused as much as possible on the nitty gritty details of the design.

Another good example mentioned earlier is that of working on the UMT camera with a different clinical PET/CT system to gain experience prior to system delivery. We were ready to use that camera as soon as possible, and the camera was used on the very first scan that was acquired on the uNeuroEXPLORER – all thanks to planning ahead.

The bottom line is that if you're going to try to build a new system well, you must have an experienced industry partner, and that's exactly what we had working with United Imaging.

E: Now that the uNeuroEXPLORER system has been operational at Yale University for almost a year, what are some ongoing projects that you and your team are working on that were made possible using the uNeuroEXPLORER system?

R: Some original projects that were planned in the original grant include comparing the uNeuroEXPLORER to the HRRT, and we were able to show those images at SNMMI recently. Now, we are focusing on using our tracers with focal brain uptake to look at small regions, such as the substantia nigra (very relevant in PD) and the locus coeruleus, which might be a key brain region in the development of dementia, including AD.

Other projects starting soon will be looking at pre-clinical AD, trying to visualize and quantify deposition of tau protein in very small regions in the entorhinal cortex. And in PD, there is great excitement surrounding the first generation alpha synuclein tracers. The signals to be imaged will be extremely small, and the uNeuroEXPLORER is going to be the natural system for those studies; we'll be beginning those scans in the coming weeks.

Some of the other areas we're looking into are the potential applications in head and neck tumors, and that's that is also very exciting. So far, the initial comparisons of patients scans on the uNeuroEXPLORER against a state-of-the-art conventional whole-body PET/CT are very encouraging – our oncologists are very excited about seeing how we can really push the envelope with the uNeuroEXPLORER.

We're also beginning scans in adolescents where we're dramatically dropping the radiation dose. Thanks to the high sensitivity of the uNeuroEXPLORER, we're going to aim for as much resolution as possible with reduced counts compared to a standard dose, and I think that's going to open tremendous opportunities. Also, we have the very good UMT camera to handle motion correction, and of course, adolescents do tend to move more than adults.

Also, many of our investigators at Yale are very excited about being able to apply and use the uNeuroEXPLORER. For example, if we're following subjects longitudinally, we expect to be more sensitive in detecting small changes. Certainly, that increased sensitivity of the uNeuroEXPLORER is going to provide an advantage in that area. Alternatively, we can lower the dose to perform more scans in the same subject with one tracer or perform multi-tracer PET, such as combining a synaptic marker with a dopaminergic marker in PD.

E: For some time, clinicians have primarily focused on the use of standardized uptake value (SUV) as a means of performing semi-quantitative analysis of PET images. What could serve as the pivotal point to encourage clinicians to adopt more sophisticated analysis with high-performance systems such as the uNeuroEXPLORER?

R: Let's start with FDG. Many sites are evaluating the impact of using SUV or a more quantitative measure such as the Patlak net uptake value (Ki). With the current generation of machines, the sensitivity of the system can be a crucial limiting factor. In Patlak analysis, you're trying to measure a slope, and in SUV you're measuring the mean value. Intrinsically, slopes are more variable than the mean value. The subtlety is that, in many cases, the slope is more important than the mean value; this is shown most dramatically if we're looking at metastases in the liver where the kinetics of the tumor are rising, and the kinetics in the normal liver are flattening out. If you measure the slope, you can easily identify liver tumors compared to normal liver.

To address this, we need the higher statistical quality. Right

now, to get a good Patlak image on most systems, you need a reasonably long period of scan time – longer than what you'd like to do, especially if you're trying to do whole body imaging.

The uEXPLORER is already showing that you can perform whole body scans within 10 min, and you're starting to get reasonable Patlak images in that short time. We're going to be able to see those same kind of advantages for the head and neck patients, to see how much shorter those scans could be, and what advantages will be provided by a Patlak uptake image over SUV.

The requirements of clinical reimbursement certainly push for short scans that can adapt easily into normal clinical throughput. One approach for other tracers is a "coffee break" protocol which is composed of an early image and a late image, with a break in between. For now, only a few facilities can handle such a protocol, so we'll need to see the data from these sites to assess the clinical utility. So, for now I think the main step forward will be to take advantage of the huge sensitivity advantage of the uNeuroEXPLORER, like what we're seeing already with the total-body uEXPLORER.

There is one other subtlety when you have very good resolution. There could be cases where you choose to not use all the resolution. If we blur the images a bit, we can get much lower noise, and that can produce other advantages. So, I expect that there'll be some interesting dynamic analyses that might operate at different resolution levels to achieve the best balance of image resolution and quantification from the dynamics within a short scan.

E: What are your thoughts on the future of brain PET imaging in clinical and in research over the next 20 years, and how can industry help accelerate the progress?

R: Great question.

In research, we've been exploring the brain with pharmacology for many years, and the uNeuroEXPLORER is now putting us at a level where we can dive down and look at very small brain nuclei to begin to understand their effects in various diseases. One of the exciting results that we've seen already was being able to visualize some small nuclei within the thalamus, specifically the anterior thalamus, with a dopaminergic marker. This nucleus had not been imaged with PET reliably before. As we look at every new scan now, the image quality matters to identify something new that we can evaluate. The brain is so complex, and the range of neuropsychiatric disorders is so broad that being able to make a reliable measurement in these tiny regions with the right tracer is going to open up a lot of opportunities, both in patient identification drug development, and treatment evaluation.

Clinical impact will take longer, in part because of how many different relevant molecules there are in the brain. We're seeing how, in the cancer world, FDG was the only tracer for so long – and of course FDG was extremely valuable for looking at tumors. But, as the PSMA compounds are now readily available for prostate cancer, how FAPI's applications are exploding, and the value of these tracers is that they can be applied in a large number of patients.

In the brain, the biggest clinical target, of course, is dementia. But there are so many questions: which targets are we going to be imaging to identify which patients would be suitable for the new treatments? Will the imaging agents be better than samples of cerebral spinal fluid (CSF) or plasma? Identifying patients as early as possible in the disease progression is critical to be able to clear amyloid and other proteins from the brain. I believe that the imaging agents, at early disease when the changes in the blood and CSF are small, are going to be more valuable.

Overall, I think that the neurological disorders – in AD, PD, and related disorders – are going to be the main focus, where targeted tracers can help you pick the patients who are suitable for the drug treatment and to then monitor the success of those treatments.

E: Is there anything else you would like to share with the readers regarding the NX project?

R: Perhaps, I would like to send a message to people interested in doing brain research with imaging.

I've been fortunate to be in this field since I was a graduate student at UCLA starting 45 years ago. The images of that era were a far cry from those the uNeuroEXPLORER, but it was also an exciting time then to learn about the potential of PET to image virtually any physiological process, to bring quantification into the mix, and then watch this technology turn into routine clinical practice.

So, for me, that excitement has not gone away in 45 years, and it's incredibly fun to be able to continue to study the brain

with PET, and now be able to do that with a system of the quality of the uNeuroEXPLORER.

Working with partners like UC Davis and United Imaging has made this journey an exceptional ride and it has been really fun to be able to do this work that at this phase of my career. It's truly exciting to show these incredible images and start looking at the brain in ways that have never been done before.

E: With that, Dr. Carson, thank you very much for your time, and we look forward to making more history with you in the mind-blowing world of brain PET imaging 😊

R: Thank you so much for the opportunity.

Expert's Biography

Dr. Richard E. Carson
Professor
Departments of Radiology and Biomedical Imaging and of
Biomedical Engineering
Yale University, New Haven, CT, USA

Dr. Richard E. Carson is Professor of Radiology and Biomedical Imaging and of Biomedical Engineering at Yale University. He is a world-leading researcher in brain PET imaging and is the pioneer who partnered with the University of California, Davis (UC Davis) and United Imaging to develop the next-generation dedicated brain PET/CT system, the uNeuroEXPLORER, through a $10.2M USD U01 academic-industry partnership grant funded by the National Institutes of Health (NIH) in late 2020. Dr. Carson has received many prestigious awards, has published over 400 papers in peer-reviewed journals, and has given over 175 invited lectures, including the Henry N. Wagner Jr. Lectureship at the SNMMI Annual Meeting in 2018. Together with the NeuroEXPLORER consortium, Dr. Carson and his colleagues have been honored with the 2024 SNMMI Image of the Year award. Their publication has also been highlighted as a "Featured Article" in the Journal of Nuclear Medicine (DOI: https://doi.org/10.2967/jnumed.124.267767). Additionally, their work has garnered attention across multiple media outlets, including AuntMinnie.com and The Imaging Wire.

Machine learning based diagnosis of Alzheimer's disease using volumetric analysis of gray and white matter

Marufjon Salokhiddinov[1], Gulnara Rahkimbaeva[2]
[1] Department of Radiology, Zangiota №2 Clinical Hospital, Tashkent Medical Academy, Uzbekistan
[4] Department of Neurology, Tashkent Medical Academy, Uzbekistan

1. Introduction

Alzheimer's disease (AD), a primary degenerative disease of the brain, is characterized by progressive deterioration of memory and other cognitive functions, as well as behavioral and other disorders. As per the World Health Organization (WHO) experts, AD is the primary cause of dementia among older individuals. The incidence of the AD exhibits a positive correlation with progressing ages. Currently, clinical presentation and psychological examinations are the primary methods used to diagnose AD. However, as compared to the gold-standard neuropathological diagnosis, the diagnosis of AD exhibits lower specificity (70%) and sensitivity (70%) (1). Numerous studies have been conducted to identify biomarkers for Alzheimer's disease (AD) (2, 3), along with various imaging techniques that employ magnetic resonance imaging (MRI) and positron emission tomography (PET) (4, 5).

Multiple MRI scans of the brains of AD patients have found abnormalities in the gray matter (GM) region. In contrast to healthy control (HC), AD patients had significantly reduced GM volume, decreased total brain volume, and larger ventricles (6-8). During the initial phases of the disease, there was a noticeable reduction in GM volume in specific areas of the brain. This mostly affected the medial temporal structures, such as the hippocampus, amygdala, and entorhinal cortex, as well as the posterior cingulate gyrus and medial thalamus on both sides (9-11). In response to the progression of the disease, abnormal brain areas spread to the frontal and parietal lobes of the brain (12, 13).

Measuring brain volume is an essential task in neurological and psychiatric research. The variations in GM, WM, and cerebrospinal fluid (CSF) volume can be used to identify physiological processes, medical conditions, or severity of an illness (14, 15). The main uses of brain volume measurement in neurological sciences include diagnosis, disease monitoring, and the evaluation of neurodegenerative disease treatment like AD (16-18). Thus, the assessment of brain volume is an essential initial stage in the majority of neuroimaging research. MRI is a precise technique for quantifying the volume of organs or structures.

Brain volume quantification in MR images can be carried out using manual, semi-automated, or fully automated approaches. For manual volume calculation of individual brain compartments from MRI data, two commonly used techniques are stereology and manual tracing (19, 20). Volumetric measurements must be exact and precise for both reliability and reproducibility. Automated methods are becoming increasingly important in brain volume studies, as manual estimation is time-consuming and labor-intensive (21).

The objective of the study was to evaluate the brain volume in HC individuals and patients with mild AD using deep learning network. Additionally, the study aimed to evaluate the performance of this model using machine learning classifiers.

2. Materials and methods

2.1 MRI data

This study employed 3T MRI scans from participants enrolled in the Alzheimer's Disease Neuroimaging (ADNI) – Phase 3. These scans were obtained from the ADNI (22) public website (http://www.loni.ucla.edu/ADNI/). This study included baseline MRI scans from 39 HC subjects and 39 individuals with a diagnosis of mild AD. The mean age was 70.90±7.20 years and the age range varied between 60 to 80 years across all subjects. Each subject underwent the acquisition of high-resolution T1-Weighted MRI scans using a sagittal 3D MP-RAGE sequence on a Siemens scanner. In this study, scans were obtained in the early phase of ADNI3 when availability was limited to the slice thickness of 1.2 mm with Siemens scan. The details of the MR parameters are shown in table 1.

2.2 Deep learning model and parameters

The current study utilized a cascaded weakly supervised confidence integration network (CINet) developed by United Imaging Intelligence, Shanghai, China (23) to quantify the volume of GM and WM regions through brain MR image parcellation. This deep learning-based tool can segment brain regions into sub-regions and quantify those regions.

2.2.1 Confidence network

A confidence network is first trained to predict confidence that assesses the quality of the label at each instant in order to properly utilize images with weak labelling. The weakly labeled images form a dataset $\{(X_1, Y_1), (X_2, Y_2),\ldots,(X_i, Y_i)\}$, where Xi represents the i^{th} image in the dataset (the input data), Yi corresponds to the label associated with Xi and Wi refers to the weak label map for the image Xi. Figure 1 depicts the confidence network's architecture. The network is provided with an unlabeled image and its weak label map. The discrepancies between the weak labels and the actual labels are used as a training metric. The output of the network can be considered a measure of confidence for the process of making inferences about the weak labels of the input image. The confidence network can be used to assess the data with weak labels once it has been trained.

2.2.2 CINet and loss function

V-Net is indeed a well-known deep learning model designed specifically for the segmentation of 3D medical images. Three improvements were implemented to the fundamental framework of V-Net with the aim of detecting variations in volume. First, as illustrated in figure 1, V-Net was divided up into two subnetworks. Only intermediate variables connected to one of the sub-networks are accessible during the training phase. The second adjustment involves substituting all the convolution operations in the second sub-network with 1*1*1 convolutions. The field of view can remain consistent at this point. The final change is to choose a patch at random from the first sub-output networks to serve as the second sub-input. The CINet framework is depicted in figure 2.

The atlas dataset is a collection of high-quality, labeled brain images used as a reference or guide for training segmentation models. Each image in the atlas dataset is paired with a corresponding ground truth label that delineates the structures of interest within the brain. The primary purpose of the atlas dataset is to provide a robust reference for training and validating the segmentation model (CINet). The atlas data is used in the fine-tuning phase of training CINet after it has been initially trained on a weakly labeled dataset. For atlas dataset $\{(M_1, L_1), (M_2, L_2),\ldots,(M_k, L_k)\}$ and the weakly labeled dataset $\{(X_1, Y_1, C_1), (X_2, Y_2, C_2),\ldots(X_i, Y_i, C_i)\}$, two different loss function were utilized in the training stage, where C_i is the confidence map for X_i, indicating the reliability of the weak label. Here, the confidence map Ci as masks by setting a threshold (i.e., α) to select parts of the image to enhance the performance of the segmentation network. The proposed loss is defined as follows:

$$Loss = \sum_x [C(x) > \alpha] * CrossEntropy(CINet(X), Y)(x) \quad (1)$$

Table 1: Details of MR Data. GR = Gradient Echo, IR = Inversion Recovery, TE = Echo time, TI: Inversion time, TR: Repetition time

Acquisition Plane: Sagittal	**Pulse Sequence:** GR/IR
Acquisition Type: 3D	**Slice Thickness:** 1.2 mm
Coil: Phase-array	**TE:** 3.0 ms
Field strength: 3 T	**TI:** 900 ms
Flip Angle: 9 degrees	**TR:** 2300 ms
Matrix Size: 240 x 256 x 170	**Pixel Spacing:** 1.1 mm x 1.1 mm
Manufacturing Model: Prisma Fit	

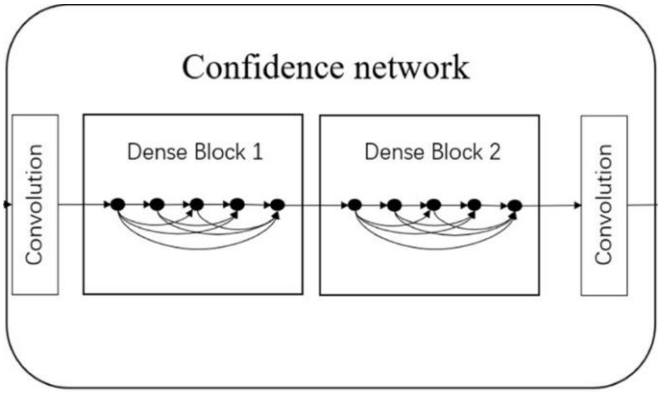

Figure 1: The architecture of the confidence network (Figure adopted from Xiao et al. (2019) (23))

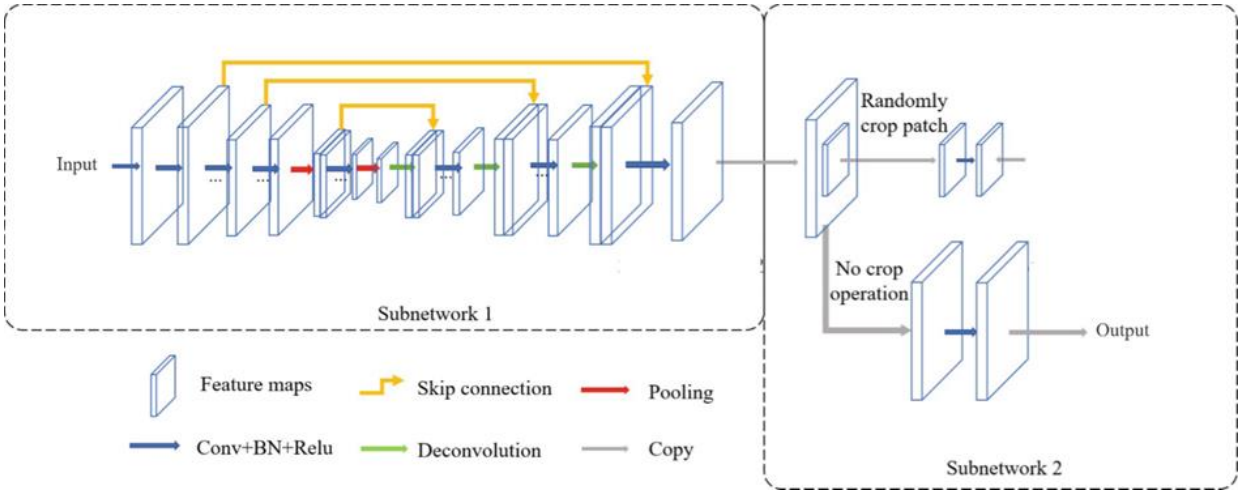

Figure 2: CINet framework (Figure adopted from Xiao et al. (2019) (23))

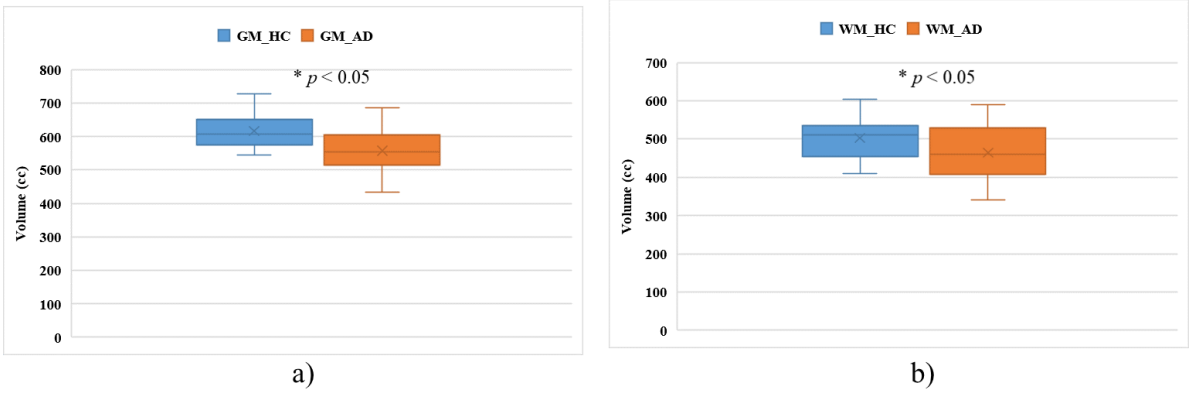

Figure 3. Box plots for GM and WM volumes of healthy and AD subjects

2.3 Statistical analysis

The statistical analyses were carried out using MedCalc for Windows, version 12.2.1 (MedCalc Software in Mariakerke, Belgium). The volumes of GM and WM in HC and individuals with mild AD were compared, and the statistical significance of the results was evaluated using a paired sample t-test with a p-value of less than 0.05.

Moreover, the model's diagnostic performance was assessed using machine learning methods, particularly linear discriminant analysis (LDA), linear support-vector machine (SVM), and Gaussian SVM classifier. These machine learning techniques were employed to assess the performance of the model through classifying between individuals with HC and those with mild AD. The sensitivity, specificity, accuracy and area under the receiver-operating characteristic curve (AUC) were measured to evaluate the performance of the classification.

3. Results

The mean ± SD of GM volume was 616.85 ± 49.67 cc for HC patients and 557.71 ± 62.73 cc for mild AD patients. For HC patients, the mean WM brain volume was 503.30 ± 58.21 cc, while for mild AD subjects, it was 464.72 ± 70.60 cc. Both GM and WM volume values for HC showed significant ($p < 0.05$) higher than mild AD subjects. Figure 3 shows the boxplots distribution of the GM and WM brain volume of HC and mild AD subjects.

The supervised machine learning classifiers were given the inputs of GM and white matter WM volumes, which were then classified into HC and mild AD classes. The performance of this two-class classification, involving GM and WM volumes, was evaluated using three different classifiers. The Gaussian SVM classifier demonstrated the highest performance with sensitivity of 75.00 ± 1.06%, specificity of 76.67 ± 1.87%, accuracy of 75.10 ± 2.05% and AUC of 0.77 using the combination of GM and WM volumes. The classification performance obtained using only GM and WM volume is shown in figure 4.

4. Discussions

AD is indeed a degenerative neurological condition characterized by a progressive decline in cognitive function, which significantly impacts various aspects of daily life. An effective method for early detection is high-resolution 3D MRI, which enables the assessment of alterations in the amount of gray and white matter in the brain. AD is mostly attributed to the gradual deterioration of both white and gray matter, in contrast to the typical aging process.

Numerous brain MRI investigations have revealed anomalies in the GM of AD patients. According to a number of studies, measuring the gray and white matter volume with an MRI can successfully identify AD in its early stages (24, 25). A study found that the automated assessment of GM volume using MRI was able to effectively distinguish between those who are in normal health and those who have AD (26). A number of investigations have been conducted to examine the use of automated artificial intelligence (AI)-based volume measurement for the early detection of AD.

The researchers employed a convolutional neural network (CNN) to partition the brain into regions containing GM and WM, as well as calculate the volumes of these regions, in a cohort of AD and HCs (27). Additionally, individuals with moderate cognitive impairment can be identified based on abnormalities identified in both gray and white matter volume (28). Another study found that patients with AD showed larger ventricles, considerably less whole brain volume, and lower global GM volume than normal controls.

In this study, we utilized a deep learning method known as CINet, as described in section 2.3, to precisely determine the volumes of GM and WM. The findings indicated that the brain volume of GM and WM in healthy subjects were considerably higher than in individuals with mild AD, with a statistical significance level of $p < 0.05$. Our study showed that individuals with AD in the early stages exhibited a more significant decline in brain volume compared to a control group with similar characteristics. The use of the CINet for brain parcellation allows not only accurate brain region segmentation but also precise estimation of different brain region volumes for diagnostic assessment. The combination of the volumes of GM and WM yielded to an accuracy of 75.10 % in classifying two separate categories.

The use of the CINet combined V-Net algorithm for GM and WM volume measurement in early-stage AD has several advantages over traditional manual segmentation methods. Firstly, the automated algorithm is faster and more efficient, completing the processing within 15 seconds. This rapid speed provides a notable advantage, especially in clinical environments, as it allows for more frequent measurements over time. Secondly, the algorithm has shown high levels of accuracy and reliability, which minimizes the risk of human

error and variability. The proposed method may enhance accuracy or precision in volumetric measurements, potentially due to superior image processing techniques, more precise anatomical atlases, or advanced statistical approaches.

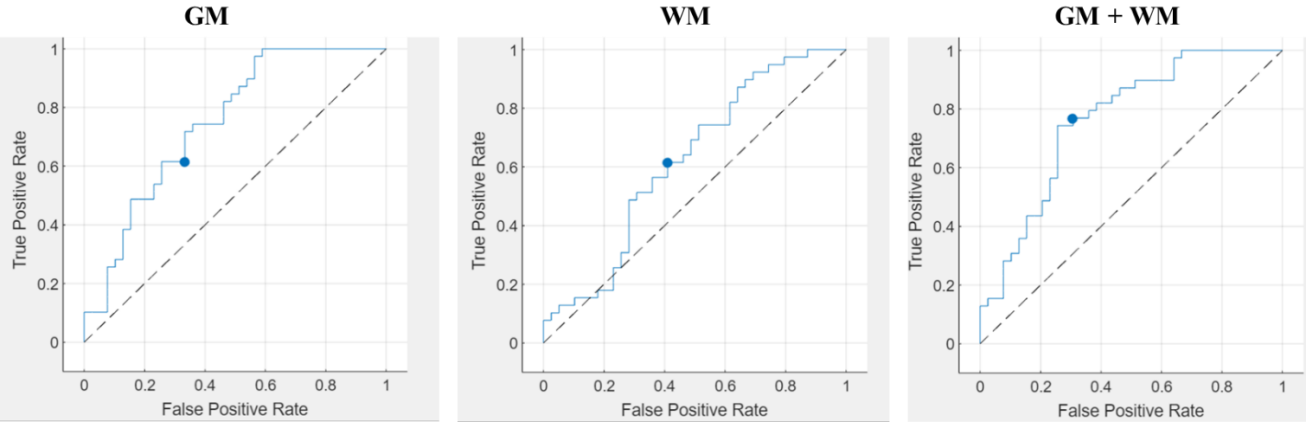

Figure 4: ROC graphs for the two-class classification using GM, WM and combination of GM, WM volumes

5. Challenges and limitations

Despite the potential of automated AI-based volume assessment utilizing high-resolution 3D MRI for early detection and treatment of AD, there are still certain challenges and limitations. Limited access to high-quality MRI images may impact the effectiveness of this technique. Large datasets of MRI scans from both healthy people and AD patients are needed for researchers to establish precise algorithms for measuring gray and white matter volume. Although MRI is an accurate means of detecting alterations in the amount of gray and white matter associated with AD, it is not a precise measure of cognitive performance. It is essential to compare automated AI-based volume assessment to other markers of cognitive impairment in order to ensure accuracy and application in clinical practice.

6. Conclusion

The study findings indicate a significant decline in the amount of GM and WM regions among individuals diagnosed with mild AD. The proposed classification methodology achieved an accuracy of 75.10% and AUC of 0.77 in the classification of HC and mild AD subjects using the combination of GM and WM volumes.

7. Data availability

The data supporting the findings of this study are available from the ADNI database and can also be obtained from the corresponding author.

8. References

1. Knopman DS, DeKosky ST, Cummings JL, et al. Practice parameter: diagnosis of dementia (an evidence-based review). Report of the Quality Standards Subcommittee of the American Academy of Neurology. Neurology 56 (2001) 1143–1153.

2. Hampel H, Burger K, Teipel SJ, et al. Core candidate neurochemical and imaging biomarkers of Alzheimer's disease. Alzheimers Dement 4 (2008) 38–48

3. Xu XH, Huang Y, Wang G, et al. Metabolomics: a novel approach to identify potential diagnostic biomarkers and pathogenesis in Alzheimer's disease. Neurosci Bull 28 (2012) 641–648

4. Jack CR Jr, Lowe VJ, Senjem ML, et al. 11C PiB and structural MRI provide complementary information in imaging of Alzheimer's disease and amnestic mild cognitive impairment. Brain 131 (2008) 665–680.

5. Öziç, Muhammet Üsame , Özşen, Seral. Comparison Global Brain Volume Ratios on Alzheimer's Disease Using 3D T1 Weighted MR Images. Avrupa Bilim ve Teknoloji Dergisi 18 (2020): 599-606 .

6. Good CD, Scahill RI, Fox NC, et al. Automatic differentiation of anatomical patterns in the human brain: validation with studies of degenerative dementias. Neuroimage. 17 (2002): 29–46.

7. Chen KW, Reiman EM, Alexander GE, et al. An automated algorithm for the computation of brain volume change from sequential MRIs using an iterative principal component analysis and its evaluation for the assessment of whole-brain atrophy rates in patients with probable Alzheimer's disease. Neuroimage. 22 (2004)134–143.

8. Karas GB, Scheltens P, Rombouts SA, et al. Global and local gray matter loss in mild cognitive impairment and Alzheimer's disease. Neuroimage. 23 (2004) :708–716.

9. Karas GB, Burton EJ, Rombouts SA, et al. A comprehensive study of gray matter loss in patients with Alzheimer's disease using optimized voxel-based morphometry. Neuroimage. 18 (2003):895–907.

10.Hirata Y, Matsuda H, Nemoto K, et al. Voxel-based morphometry to discriminate early Alzheimer's disease from controls. Neurosci. Lett. 382 (2005):269–274.

11.Baxter LC, Sparks DL, Johnson SC, et al. Relationship of cognitive measures and gray and white matter in Alzheimer's disease. J. Alzheimer's Dis. 9 (2006):253–260.

12. Good CD, Scahill RI, Fox NC, et a. Automatic differentiation of anatomical patterns in the human brain: validation with studies of degenerative dementias. Neuroimage. 17 (2002):29–46.

13. Scahill RI, Schott JM, Stevens JM, et al. Mapping the evolution of regional atrophy in Alzheimer's disease: unbiased analysis of fluid-registered serial MRI. Proc. Natl. Acad. Sci. 99 (2002):4703–4707

14. Nair SSK, Revathy K, editors . Quantitative analysis of brain tissues from magnetic resonance images. Digital Image Processing, 2009 International Conference on; 2009: IEEE

15. Geuze E, Vermetten E, Bremner JD. MR-based in vivo hippocampal volumetrics: 1. Review of methodologies currently employed. Mol Psychiatry 10 (2005):147–59.

16. Hahn HK, Jolly B, Lee M, Krastel D, Rexilius J, Drexl J, et al.editors . How accurate is brain volumetry? International Conference on Medical Image Computing and Computer-Assisted Intervention; 2004: Springer.

17. Karsch K, Grinstead B, He Q, Duan Y. Web based brain volume calculation for magnetic resonance images. Annu Int Conf IEEE Eng Med Biol Soc. 2008 (2008) 1210-3.

18. Zeinali R, Keshtkar A, Zamani A, Gharehaghaji N. Brain Volume Estimation Enhancement by Morphological Image Processing Tools. J Biomed Phys Eng. 7(4) (2017):379-388.

19. Wang D, Doddrell DM. MR image-based measurement of rates of change in volumes of brain structures. Part I: method and validation. Magnetic resonance imaging 20 (2002):27–40.

20. Acer N, Turgut AT, Turgut M, et al. Quantification of volumetric changes of brain in neurodegenerative diseases using magnetic resonance imaging and stereology: INTECH Open Access Publisher; 2011.

21. Guenette JP, Stern RA, Tripodis Y, et al. Automated versus manual segmentation of brain region volumes in former football players. Neuroimage Clin 18 (2018)888-896.

22. Misra C, Fan Y, Davatzikos C. Baseline and longitudinal patterns of brain atrophy in MCI patients, and their use in prediction of short-term conversion to AD: results from ADNI. Neuroimage 44 (2009):1415–22.

23. Xiao B, Cheng X, Li Q, Wang Q, Zhang L, Wei D et al. Weakly Supervised Confidence Learning for Brain MR Image Dense Parcellation. In Machine Learning in Medical Imaging. MLMI 2019. Lecture Notes in Computer Science, 1861. Springer, Cham.

24. Arrondo P, Elía-Zudaire Ó, Martí-Andrés G, et al. Grey matter changes on brain MRI in subjective cognitive decline: a systematic review. Alzheimers Res Ther. 2022;14(1):98

25. Putcha D, Katsumi Y, Brickhouse M, et al. Gray to white matter signal ratio as a novel biomarker of neurodegeneration in Alzheimer's disease. Neuroimage Clin. 2023;37:103303

26. Battineni G, Chintalapudi N, Amenta F, Traini E. A Comprehensive Machine-Learning Model Applied to Magnetic Resonance Imaging (MRI) to Predict Alzheimer's Disease (AD) in Older Subjects. J Clin Med. 2020;9(7):2146

27. Desikan, R. S., Cabral, H. J., Hess, C. P., et al. Automated MRI measures predict progression to Alzheimer's disease. Neurobiology of Aging 31(8) (2010) 1364-1374.

28. Liu, M., Cheng, D., Yan, W. Automatic segmentation of hippocampus in Alzheimer's disease using deep learning with clinical interpretation. Frontiers in Neuroscience, 12 (2018), 44.

Author Biography

Dr. Marufjon Salokhiddinov
MD, Diagnostic Radiologist
(Neuroradiology)
Tashkent Medical Academy,
Uzbekistan

Dr. Marufjon completed his Bachelor of Medicine, Bachelor of Surgery (MBBS) from Tashkent Medical Academy, followed by a one-year internship in Neurology. He then pursued Master of Science (MS) in Medical Imaging at the University of Aberdeen, UK. After completing his MS, he joined the Department of Radiology at Tashkent Medical Academy. Since 2020, Dr. Marufjon has been serving as an MD Radiologist at Republic Zangiota №2 Clinical Hospital in Tashkent, Uzbekistan. He has received several accolades, including the "El-yurt Umidi" scholarship funded by the Government of Uzbekistan for his MSc, the Young Investigator Award from the WFN, and best poster awards from WCN, ESR, WFITN, and AAN. Additionally, Dr. Marufjon has published numerous research articles at both national and international conferences.

Experience with Quantitative Brain PET using the uMI 550 PET/CT at Stony Brook

Paul Vaska[1,2,3]

[1] Department of Biomedical Engineering, Stony Brook University, Stony Brook, NY, United States
[2] Department of Radiology, Renaissance School of Medicine at Stony Brook University, Stony Brook, NY, United States
[3] PET Imaging Core, Renaissance School of Medicine at Stony Brook University, Stony Brook, NY, United States

1. A Brief History of SBU PET Core

The PET Imaging Core of the Renaissance School of Medicine at Stony Brook University (SBU) was created in 2012 by Dean Ken Kaushansky and placed under the leadership of Drs. Ramin Parsey and Mark Slifstein who transitioned from the PET group at Columbia University. PET imaging researchers were initially recruited from Columbia as well as Brookhaven National Laboratory (BNL). Dr. Peter Smith-Jones was recruited to design the PET radiochemistry facilities which are currently led by Dr. Wenchao Qu. The Core facility was constructed in a spacious wing of the new MART building adjacent to the main University Hospital and is now fully functional. It houses a GE PETtrace 800 cyclotron, a research radiochemistry laboratory with 5 hot cells, a Good Manufacturing Practice (GMP) radiosynthesis laboratory with 5 hot cells (2 standard, 2 mini and 1 dispensing), a Quality control (QC) laboratory, and a comprehensive blood analysis lab to generate metabolite-corrected plasma input functions for quantitative brain studies. The first PET scanner dedicated for research studies was a 1990's vintage Siemens HR+ moved from BNL and upgraded by MiE with new electronics and software. Research studies are also performed on a nearby Siemens mMR PET/MRI owned by the Department of Radiology. In 2022, the Core purchased a United Imaging uMI 550 PET/CT which has been the workhorse of our research studies since, with over 140 scans performed. In 2023, SBU and United formalized a research agreement to develop methods to optimize the use of the uMI 550 for brain PET studies, which make up the majority of research studies in the core. Human studies with locally synthesized tracers began in 2015 for ^{18}F tracers, and in 2022 for ^{11}C tracers. Much of the funding for the core was philanthropic, in particular from Kavita and Lalit Bahl and the Laurie family. SBU supports a complete range of imaging facilities for human and animal research, including a small-animal PET core led by Dr. Vaska that provides imaging with a Siemens Inveon PET/SPECT/CT system and access to custom high-resolution PET systems such as the RatCAP (1).

2. Practical Considerations for Quantitative Brain PET on the uMI 550

Like almost all PET/CT scanners, the uMI 550 is optimized for clinical application, primarily whole-body oncology scans. In our experience so far, it is also appropriate for quantitative brain research studies, although there are some important practical issues to consider. For studies without blood sampling, the standard headfirst supine position works best. The head is positioned within the supplied head holder and additionally, expanding foam can be used to give a custom fit to further minimize motion. However, this patient position is not ideal for studies using an arterial line in the arm for blood sampling nor for injection while in the scanner, as in typical dynamic scans used for kinetic modeling, because the PET component is farther from the base of the bed, and the arms are not as accessible due to the CT component. Thus, for these studies we use feet first positioning, allowing shorter tubing (hence less dead volume and less flushing), better ability to monitor the catheter, and a less claustrophobic experience for the patient whose body is mostly outside the bore. While the bed is sufficiently long and sturdy to support this very extended position, it requires considerable space in the room, and this should be considered when constructing the room. Another consideration for the feet first position is that the supplied head holder can't be used (now positioned near the feet), so a custom setup is required - in our case a shaped piece of foam attached to the bed. For studies requiring visual stimulation, we use a small mirror at 45 degrees mounted to a curved 3D printed plastic base which is secured with Velcro

to the top of the bore just outside the PET FOV (thus not affecting the PET data).

3. Physics Considerations

3.1 Spatial resolution

The state-of-the-art resolution of the uMI 550 (2.9 mm FWHM transaxial near center NEMA (2)) is a substantial advance over the previous generation of scanners which provided closer to 4 mm FWHM (eg, Siemens mMR is 4.3 mm (3)) and better even than the Siemens Vision which provides 3.6 mm resolution (4). This is a particular benefit for brain studies by helping to reduce the partial volume effect and distinguish among the large number of nuclei and divisions of the cortex. In order to evaluate the resolution in a way that is more appropriate for brain studies, we used the Joshi method (5) with the Hoffman brain phantom scanned for an hour. Fig. 1 shows the same slice of the phantom reconstructed in different ways and the associated FWHM spatial resolution. As expected, the highest resolution is for OSEM with PSF modeling, which achieves a resolution of 3.4 mm FWHM.

3.2 Axial field of view

The long axial field of view of the uMI 550 (24 cm) is typical of modern PET systems but a big improvement over older systems like the HR+ (15 cm). Even though the whole brain can be captured in a 15 cm FOV, the sensitivity (in 3D mode) drops dramatically from the center to the edge, resulting in substantial differences in noise levels across the brain. The longer FOV reduces this effect and also provides greater overall sensitivity if the brain is positioned in the axial center. Moreover, the long FOV coupled with the improved spatial resolution facilitates the use of an image-derived input function (IDIF) from ROIs on the carotid arteries, although this has not yet been explored by our group. One potential concern we are investigating is the normalization of image slices within 1-2 cm from each axial edge, so axial centering of the brain in the FOV remains important, and IDIF measurements may require additional corrections until this is resolved.

3.3 Sensitivity and Noise Equivalent Count Rate

The NEMA line source sensitivity is 10.24 cps/kBq and NECR peak is 124.4 kcps at 18.85 kBq/mL (2). This is somewhat lower than the Siemens mMR (15 cps/kBq and 184 kcps at 23.1 kBq/mL (3)) primarily due to shorter crystals (16.3 mm vs 20 mm), but we have deemed this to be an acceptable trade-off for the improved spatial resolution and lower cost.

3.4 Time-of-flight (TOF)

Although the uMI 550 may not be at the cutting edge of TOF resolution (372 ps FWHM (2)) and we have not yet fully evaluated its performance, qualitatively the feature performs without artifact and it should be helpful even for brain studies. According to the classical formulation by Budinger (6), the improvement in effective sensitivity is a factor of ~4 for brain, suggesting an SNR improvement factor of ~2.

3.5 Quantitative corrections

Given that the kinetic modeling of dynamic brain PET studies requires quantitatively accurate images, the correction methods need to be accurate, including those for randoms, attenuation, scatter, detector efficiency, deadtime, branching fraction, and overall efficiency (calibration). All corrections are implemented and appear to employ validated approaches, and we are in the process of evaluating their accuracy.

3.6 Data processing

The uMI 550 exclusively uses listmode data and sinograms. Listmode should be optimal for image accuracy because data is not rounded to fit into discrete histogram bins. On the other hand, the absence of sinograms makes it more challenging for the user to detect or diagnose hardware issues. While such issues should be largely dealt with by the QC software and/or service engineers, there would be greater confidence in the data if it could be visually inspected by the user, especially in a research environment. The system supports dynamic studies with time bins as small as 3 sec which is acceptable for quantitative brain studies.

3.7 Image reconstruction

A variety of algorithms are available, including the standard filtered backprojection (FBP) and ordinary-Poisson ordered subsets expectation maximization (OP-OSEM) which have sufficient flexibility for clinical studies. Examples are shown in Fig. 1, including a PSF modeling option which can improve resolution substantially. For research studies, there are some limitations on OSEM parameters including a maximum of 99 iterations and 2 choices for number of subsets (10 and 20, thus a plain MLEM algorithm is not strictly available at this time). There are also options with potential clinical benefit

that should be validated before use in quantitative brain PET studies. For example, AI-based noise reduction approaches are likely trained on common clinical scenarios which may be quite different from research applications, even if the radiotracer is the same. Another example is the ROSEM algorithm which adjusts the regularization (effectively the degree of image smoothing) based on acquired count levels – this should be used with caution in dynamic scans which can have greatly varying count levels across time frames, possibly resulting in varying partial volume effects across time points in the time activity curve.

3.8 Reducing CT dose

The standard attenuation correction protocol provides low noise CT images but in the case of brain PET research, these images are typically not used except for attenuation correction. In order to minimize radiation dose we performed a study using a realistic head CT phantom, and showed that reducing the mAs target from 150 to 40 preserved the value of the attenuation correction factor for each line-of-response (see Fig. 2) while lowering dose by almost a factor of 4 (to <9 mSv CTDIvol for head 16 cm phantom). Subjective PET image quality was also unaffected. The result is an effective CT dose of ~0.4 mSv which represents an almost negligible fraction of the total PET/CT study dose (typically 5-10 mSv).

3.9 Head motion

Dynamic brain studies can be as long as 3 hours, so head motion is more likely than in the clinical situation. Moreover, in order to take advantage of the improved intrinsic spatial resolution of this scanner, greater care must be taken to reduce and/or correct for head motion. United provides an optional motion correction algorithm to detect when significant motion occurs using the PET data itself (based on changes in center of mass of the projection data). It uses these time points to divide the scan into multiple time frames which are reconstructed individually, co-registered, and recombined into a single 3D image. While this may be useful for static clinical studies, it is not available as an option for dynamic scans and in any case would likely be problematic for time frames with low counts due to statistical noise in the projection data (e.g., early time frames after injection).

Thus, we are collaborating with United on evaluating a motion detection/correction approach based on an infrared structured-illumination system, called the United Imaging Healthcare Marker-less Motion Tracking System (UMT), shown in Fig 3. We measured the intrinsic positioning accuracy to be ~0.2 mm as measured by moving a head phantom in known increments, which is far smaller than the PET spatial resolution and thus sufficiently accurate for motion correction. Results from a real human study in head first supine position are shown in Figure 4.

4. Examples of Imaging Studies at SBU

The PET Core currently produces 10 different ^{11}C and ^{18}F based radiotracers for human studies, shown in Table 1, with several more in the pipeline. Many of these studies are fully quantitative, including acquisition of metabolite-corrected arterial input function and kinetic modeling. Some examples are described below.

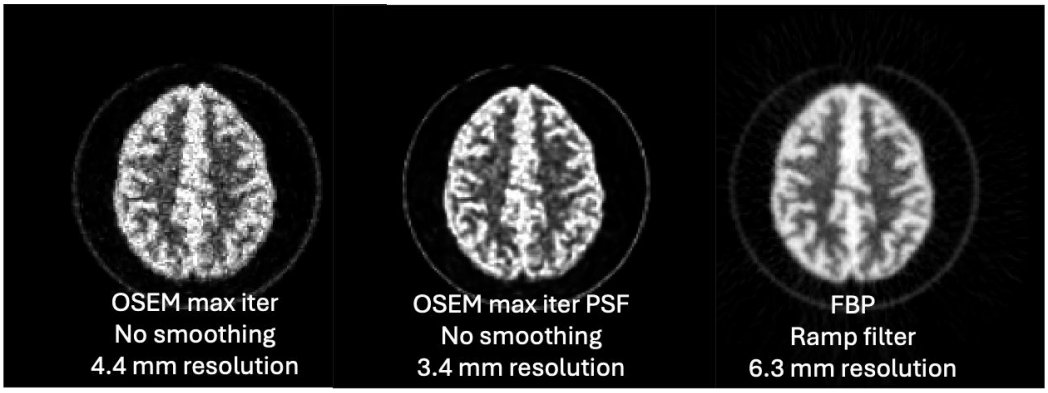

Figure 1. High statistics Hoffman phantom reconstructed with different methods and associated spatial resolutions measured using the method of Joshi et al. (5). Max iterations is 99 (10 subsets) and no post-smoothing is applied. Voxel sizes are the same for all reconstructions, and are almost isotropic at ~1.5 mm.

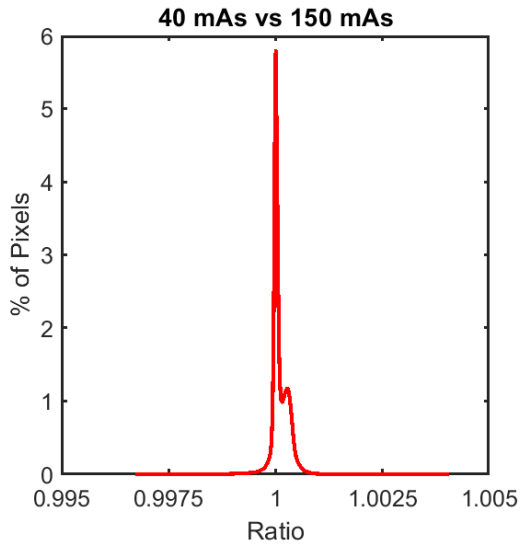

Figure 2. Histogram of ratios of LOR attenuation correction factors measured at 40 mAs relative to those at 150 mAs (default value and assumed to be the most accurate), for a CT head phantom. The ratios fall within a narrow range around 1, indicating that the correction factors are very nearly the same at both settings.

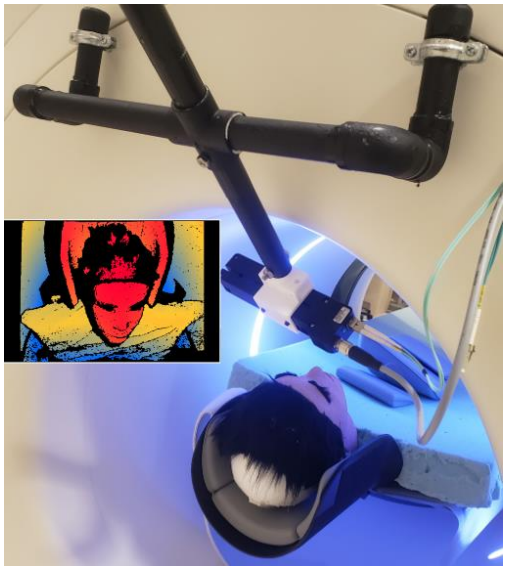

Figure 3. The UMT motion tracking system with custom holder mounted to the back of the uMI 550 PET/CT scanner. Head phantom is in head first supine position and inset photo is the raw data from the system.

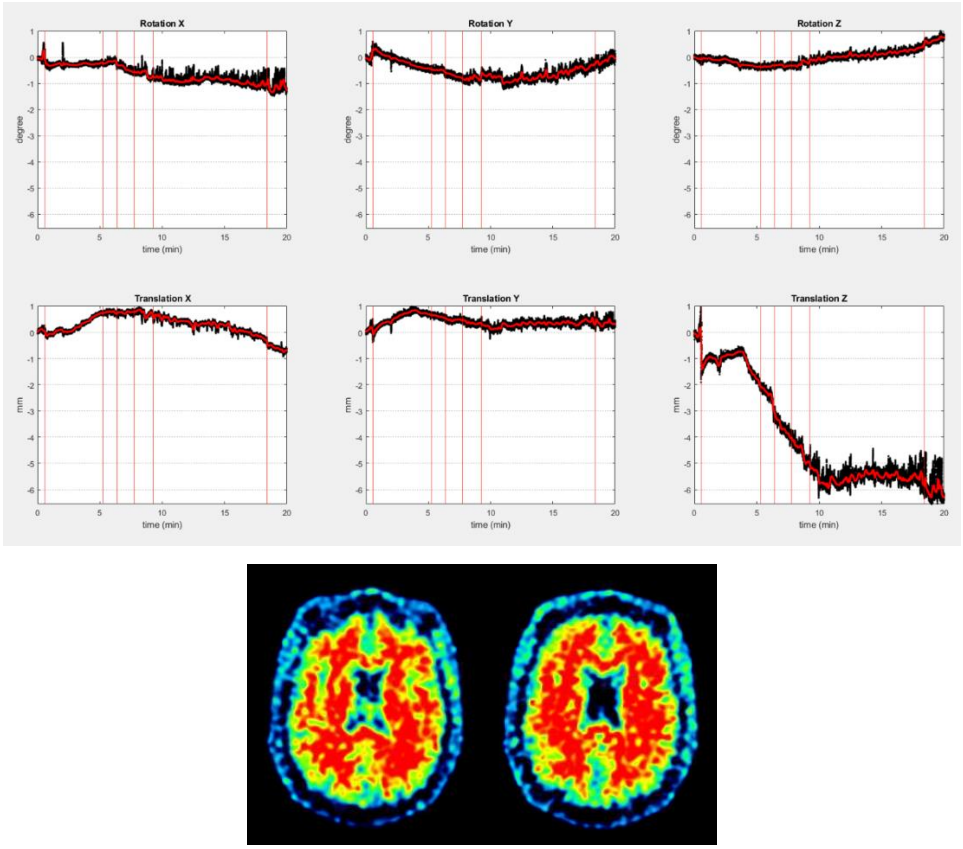

Figure 4. Top - The 6 rigid body motion parameters measured by the UMT system as a function of time during a 20 minute [^{11}C]PiB human brain study of a healthy subject. The predominant motion is a slow shift of almost 7 mm in the z direction. A motion detection algorithm applied to these traces resulted in 6 detections, indicated by the vertical red lines, which were used to define 7 time frames (each with low intra-frame motion). Bottom – the associated brain images without motion correction (left) and after reconstructing each time frame and realigning using the measured motion parameters (right). Note the improved delineation of the white matter pattern that is typical of this tracer in a non-AD subject.

Table 1. List of Radiopharmaceuticals Currently Produced by Stony Brook PET Core

Tracer	Target Molecules or Biological Processes	Application Area(s)
[18F]F-AraG	Activated T cells	Immunotherapy in Oncology
[18F]Florbetaben	Amyloid β plaques in brain	Dementia, Normal Aging
[18F]T807	Tau fibrillary tangles in brain	Dementia, Normal Aging
[18F]LY245	k opioid receptors in brain	Psychiatry (Schizophrenia, Depression, Substance Use)
[18F]VAT	Vesicular acetylcholine transporter in brain	Psychiatry, Neurology, Dementia and Normal Aging
[18F]FEPPA	Translocator Protein in brain	Neuroinflammation; Activated Microglia
[11C]ABP688	Metabotropic Glutamate Receptor 5 in brain	Psychiatry
[11C]PiB	Amyloid β plaques in brain	Dementia, Normal Aging
[11C]UCB-J	Synaptic vesicle protein 2A in brain	Synaptic Density (Psychiatry, Neurology, Epiliepsy)
[11C]PS13	Cyclooxegenase-1 in brain	Neuroinflammation

[^{18}F] FEPPA assesses changes in neuroinflammation after treatment for depression (PI Drs. Parsey and Delorenzo)

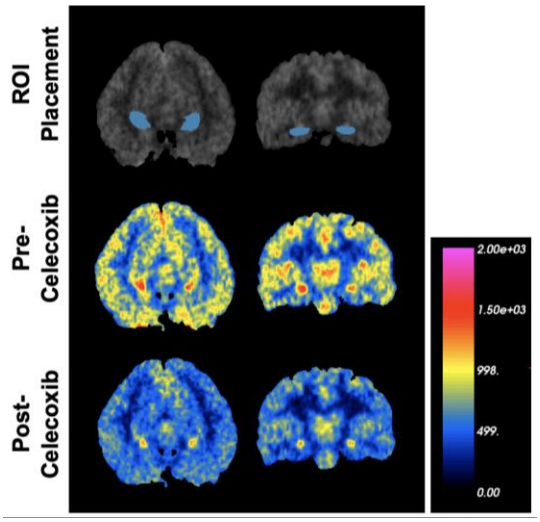

Figure 5. Neuroinflammation is decreased following treatment in major depressive disorder. Center images reflect neuroinflammation prior to treatment and bottom images are post-treatment, showing a ~25% reduction in TSPO density. A structural MRI is shown on the top row for reference. Neuroinflammation was quantified by TSPO volume of distribution (VT, which varies directly with TSPO density) using the PET tracer [18F]FEPPA at Stony Brook PET Core (blue to fuchsia, low to high). (Figure courtesy of Drs. R. Parsey and C. DeLorenzo).

[^{11}C]PiB used to investigate effects of subconcussive injury in college athletes (PI Dr. Vaska)

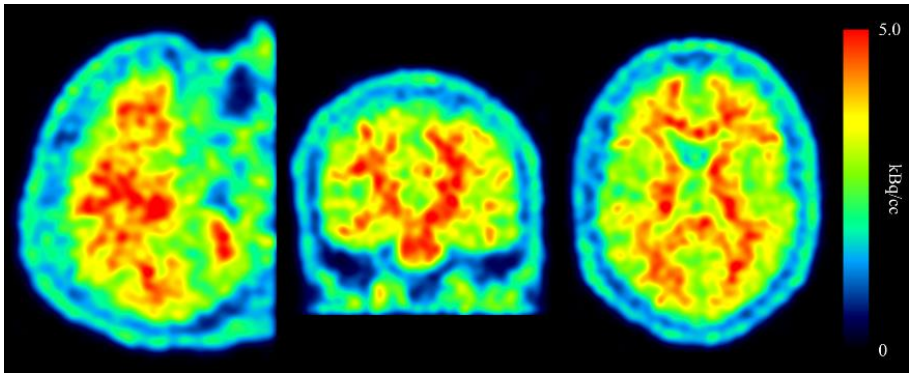

Figure 6. Image of college football player after season of play in this ongoing study. Injection was 11.7 mCi of [11C]PiB, imaged on our UMI 550 PET/CT.

5. Acknowledgements

The author acknowledges the assistance and support of Jaclyn Brunner, Juin Zhou, Lemise Saleh, Tim Cotroneo, Mark Slifstein, Wenchao Qu, Bao Hu, and William Stanley.

6. References

1.Schulz, D., et al., Simultaneous assessment of rodent behavior and neurochemistry using a miniature positron emission tomograph. Nat Meth, 2011. 8(4): p. 347-352.

2.Chen, S., et al., Performance characteristics of the digital uMI550 PET/CT system according to the NEMA NU2-2018 standard. EJNMMI Phys, 2020. 7(1): p. 43.

3. Delso, G., et al., Performance measurements of the Siemens mMR integrated whole-body PET/MR scanner. J Nucl Med, 2011. 52(12): p. 1914-22.

4.van Sluis, J.J., et al., Performance characteristics of the digital Biograph Vision PET/CT system. J Nucl Med, 2019.

5.Joshi, A., R.A. Koeppe, and J.A. Fessler, Reducing between scanner differences in multi-center PET studies. Neuroimage, 2009. 46(1): p. 154-9.

6.Budinger, T.F., Time-of-Flight Positron Emission Tomography - Status Relative to Conventional Pet. Journal of Nuclear Medicine, 1983. 24(1): p. 73-76.

Author Biography

Paul Vaska, Ph.D.
Professor of Biomedical Engineering and Radiology
PET Imaging Core at Stony Brook University
Stony Brook, NY
USA

Dr. Paul Vaska obtained a B.S. in Physics from Clarkson University followed by a Ph.D. in Nuclear Physics from Stony Brook University. He then transitioned to medical applications as Research Physicist for UGM Medical Systems in Philadelphia - a small PET scanner manufacturer led by Dr. Gerd Muehllehner, one of the pioneers of PET, which was affiliated with the University of Pennsylvania and ultimately absorbed by Philips Medical Systems. Dr. Vaska then joined the scientific staff of Brookhaven National Laboratory, in the PET group led by Drs. Joanna Fowler and Nora Volkow (now Director of the NIH National Institute on Drug Abuse). He is currently Professor of Biomedical Engineering and Radiology and one of the directors of the PET Imaging Core at Stony Brook University.

An AI-Empowered Head-Only Ultra-High-Performance Gradient MRI System for High Spatiotemporal Neuroimaging

Liyi Kang[1] and Dan Wu[1]

[1] Department of Biomedical Engineering, College of Biomedical Engineering & Instrument Science, Zhejiang University, Hangzhou, China

1. Introduction

Magnetic resonance imaging (MRI) based human brain mapping is crucial for comprehending brain organization, function, cognition, and diseases, playing an increasingly vital role in global large-scale brain projects (1). Conventional MRI scanners face challenges in achieving submillimeter resolution due to physical constraints like imaging resolution, scan time, and signal-to-noise ratio (SNR). High-field MRI systems and advanced gradient systems, along with fast acquisition and AI-based methods, have been engineered expressly to push the resolution limit. The benefits of high-performance gradient for dMRI and fMRI have been nicely demonstrated in previous studies (2,3).

However, despite these advances, MRI spatial resolution remains far from the microscopic scale required for histopathological examination. Based on restricted water diffusion shaped by the local environment, dMRI is probably the only non-invasive approach to probe tissue microstructures at sub-voxel resolution (4). Advanced dMRI models are developed in both q-space (by varying diffusion gradient strength and directions) and t-space (by varying diffusion times) to reconstruct microstructural properties, such as axonal diameter, cell size, compartment fractions, and transmembrane water exchange.

High-gradient technology has experienced enormous development over the past two decades. In addition to the mainstream clinical superconducting MRI scanner that is typically equipped with a gradient system featuring maximum gradient strength (Gmax) of approximately 40 mT/m and slew rate (SRmax) of around 200 T/m/s, newly developed clinical systems with stronger gradient performance are emerging, including Siemens Prisma+ (130 mT/m, 200 T/m/s), GE Signa UltraG (114 mT/m, 260 T/m/s), etc. Furthermore, the field has endeavored to release ultra-high gradient-performance MRI systems for research purposes. (Fig. 1)

Keys in developing a high-performance head-only gradient system mainly lie in: 1) development of high-performance Gradient Power Amplifier (GPA) to supply the required voltage, current, and duty cycle; 2) optimized gradient coil design that minimizes the peripheral nerve stimulation (PNS); and 3) specialized design of the whole MRI system to adapt to the head-only gradient coil, including the miniaturized radiofrequency (RF) transmitter/receiver coils and specialized patient bed. In addition to the hardware endeavor, dedicated imaging sequences and reconstruction algorithms are also critical towards achieving high spatial and temporal resolution neuroimaging. The current surge in artificial intelligence (AI) empowered techniques opened new avenues to improve image acquisition.

In context of the previous effort, challenges, and emerging demands in neuroimaging, United Imaging Healthcare aims to develop an integrated head-only 3.0T MRI system NeuroFrontier[1] with unprecedently high Gmax of 650 mT/m and SRmax of 600 T/m/s. The proposed system features an ultra-high-power output from parallel setup of GPAs of 7MW, an optimal gradient coil design for minimizing PNS, a miniaturized high-density RF system, AI-assisted Compressed Sensing (ACS) technique for ultra-fast imaging, and a prospective head motion correction technique for motion free acquisition.

2. Methods

The NeuroFrontier system integrates several advanced features designed to optimize neuroimaging performance:

1. Ultra-high-power Output: The system achieves an ultra-

[1] This product is not available for sale in the U.S. for clinical uses and also may not be available for such sales in other countries.

high-power output of 7MW by running two gradient power amplifiers in parallel using a novel method that eliminates the need for a large current-sharing reactor. This setup ensures efficient current distribution and stability, enabling the system to reach a maximum gradient strength of 650 mT/m and a slew rate of 600 T/m/s along each axis.

2. Gradient Coil Design: The gradient coil design employs a two-step mechanical structure to balance forces and torques, which minimizes mechanical vibrations and peripheral nerve stimulation (PNS). The gradient coils are optimized for high efficiency and low inductance, using a ten-layer cooling tube design to enhance cooling efficiency and thicker coils to improve magnetic field shielding. (Fig. 2).

3. RF System Integration: A high-density, miniaturized radiofrequency (RF) system is integrated into the head-only setup. This includes a custom 16-ring birdcage transmit coil and a 64-channel head-only receive-array coil, designed to achieve high signal-to-noise ratio (SNR) and high acceleration factors. The RF system is shielded to minimize interference with the gradient coils, using segmented copper shielding to reduce eddy currents and resistive heat.

4. AI-Empowered Compressed Sensing (ACS): The system employs AI-assisted compressed sensing (ACS) to enable ultra-fast imaging. ACS uses convolutional neural networks (CNN) to reconstruct images from under-sampled k-space data, significantly accelerating the acquisition process while maintaining image quality. This technique allows for high-resolution imaging at reduced scan times.

5. Prospective Motion Correction: To address motion artifacts, the NeuroFrontier system incorporates a prospective head motion correction technique. This method uses a compact 3D optical tracking system to capture high-resolution 3D facial contours in real-time, which are then processed to correct for head movements during scanning. This ensures high-quality imaging even in the presence of patient motion.

6. System Design and Customization: The system is built around a 3T whole-body magnet with zero liquid helium boil-off, featuring a narrowed bore and specialized apertures for the head and body. The scanner bed is customized to accommodate these apertures, providing an optimized setup for head-only imaging (Fig. 3). The overall system design prioritizes high spatiotemporal resolution and accurate microstructural mapping, making it ideal for advanced neuroimaging applications.

3. Results

3.1 High Spatiotemporal Resolution Neuroimaging

1. Prospective Motion Correction: The information of head motion is used in real-time to update sequence RF and gradient direction in the rate of repetition time (TR), to minimize the influence of the movement of the head. (Fig. 4A)

2. AI-Assisted Compressed Sensing: The system utilizes AI-assisted compressed sensing (ACS) to accelerate image acquisition using convolutional neural networks (5,6). ACS achieved high-quality, fast imaging with minimal SNR and CNR compromise. (Fig. 4B)

3. EPI Readout and High-Resolution fMRI: The gradient system allows shorter echo times (TE), leading to higher SNR and improved image resolution. Simulations showed significant SNR improvement, especially for high-resolution imaging (Fig. 5).

3.2 High-Resolution dMRI

The system's high gradient performance reduces diffusion encoding duration, further reducing TE and increasing SNR. Simulations indicated substantial SNR gains for various resolutions and b-values, enhancing the capability for high-resolution dMRI (Fig. 6).

3.3 Neuroimaging Applications

1. Laminar Specific fMRI: The system's SNR gain supports submillimeter resolution to distinguish laminar-specific interactions in cortical regions (7).

2. Laminar Specific dMRI: High-resolution dMRI at 0.8 mm isotropic resolution revealed detailed microstructural layers in the cortex and hippocampus, which were not distinguishable at lower resolutions (Fig. 7).

3. Submillimeter Tractography: The system improved tractography accuracy, reducing false positives and enhancing the visualization of detailed fiber tracts (Fig. 8).

3.4 Microstructural Estimation

1. t-Space Microstructural Mapping: The system's high gradient strength enhances sensitivity to small structures and improves the accuracy of microstructural metrics like cell diameter and intracellular fraction (Novikov et al., 2019).

2. q-Space Diffusion MRI: High b-values achievable with the system provide stronger contrast for lesion visualization and improved microstructural estimation. The system supports complex q-space models requiring high b-values and enables accelerated sampling in q-t space with deep learning-based reconstruction (Fig. 9).

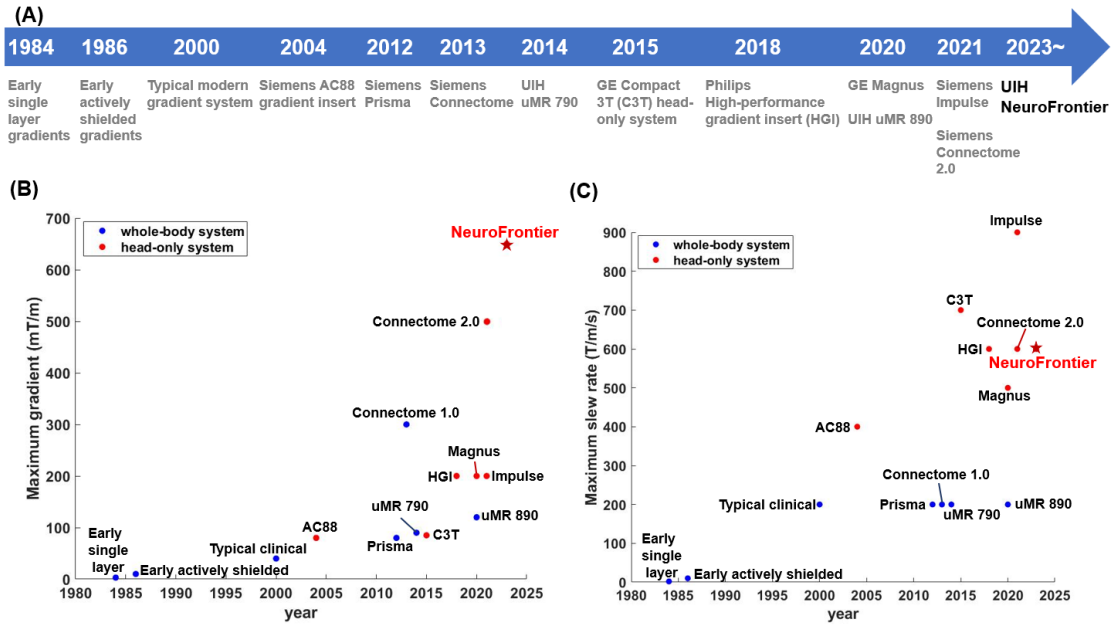

Figure 1. The history of gradient performance advances. (A) The release year of typical whole-body and head-only MRI systems. (B)-(C) The maximum gradient strength and slew rate of these systems.

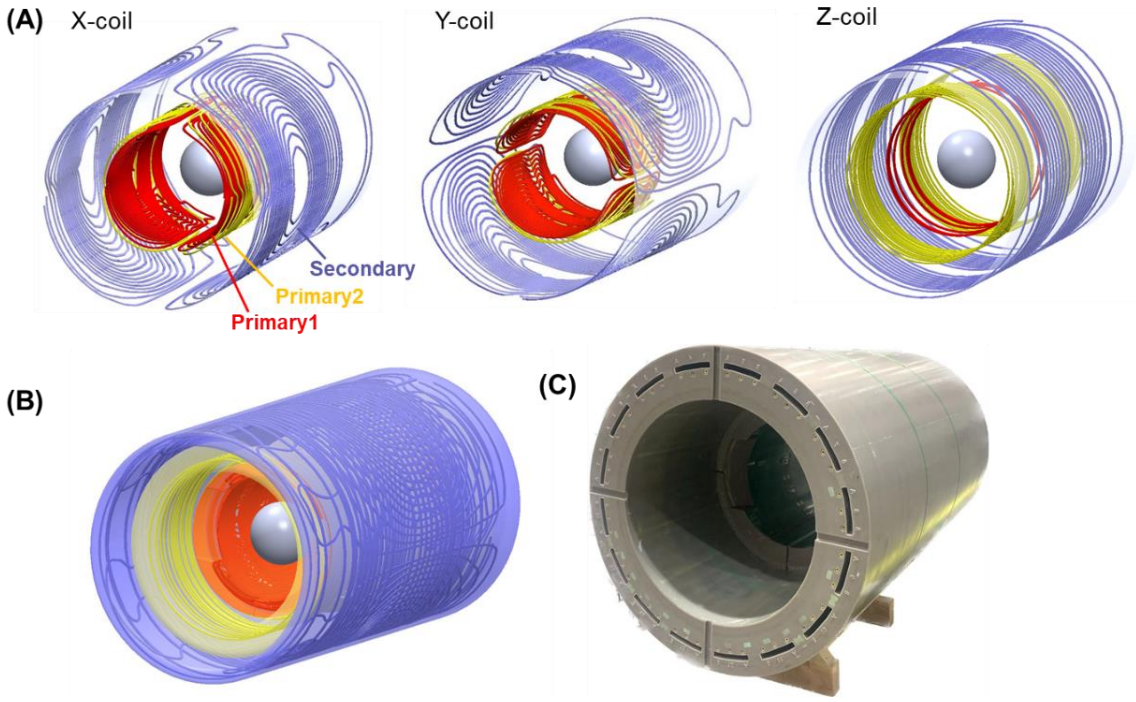

Figure 2. Gradient coils of the NeuroFrontier System. The (A) separate and (B) combined views of the two-step-structured x, y and z coils. (C) The real assembled gradient coil.

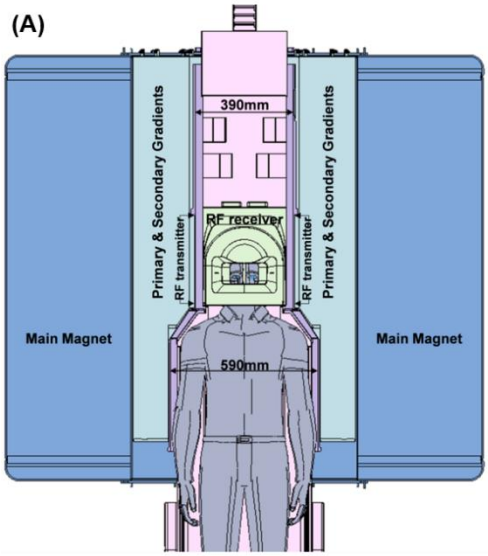

(C)

Magnet	B0 strength	3.0 T
System size parameters	Imaging FOV	220 mm
	Head aperture	390 mm
	Body aperture	590 mm
Gradient coil Performance	G_{max}	650 mT/m
	Slew rate	600 T/m/S
	G_{RMS}	120 mT/m
	Linearity over 200-mm DSV (x, y, z)	$\leq$ 7 %
Radiofrequency characteristics	Number of transmit channel	2
	Number of receive channel	64
	Max B1	20 μT

Figure 3. (A) The systematic overview, (B) real setup and (C) major performance parameters of the NeuroFrontier system.

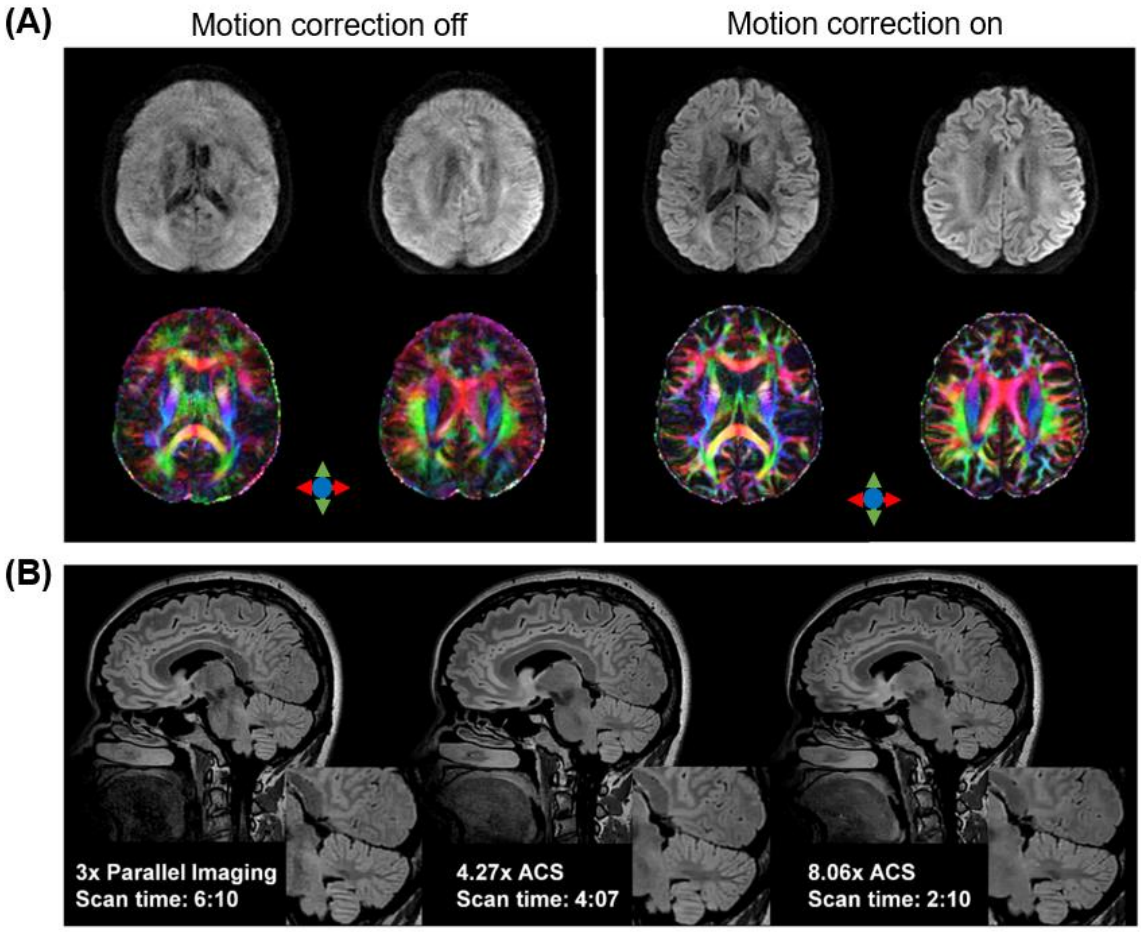

Figure 4. (A) Diffusion-weighted images and directional encoded colormaps from multi-shot dMRI acquired with prospective motion correction off and on. (B) Examples of

imaging using ACS with acceleration factors of 4.27 and 8.06. Compared to the conventional parallel imaging (left), the images from ACS (middle and right) significantly reduced imaging time while achieving equivalent image quality.

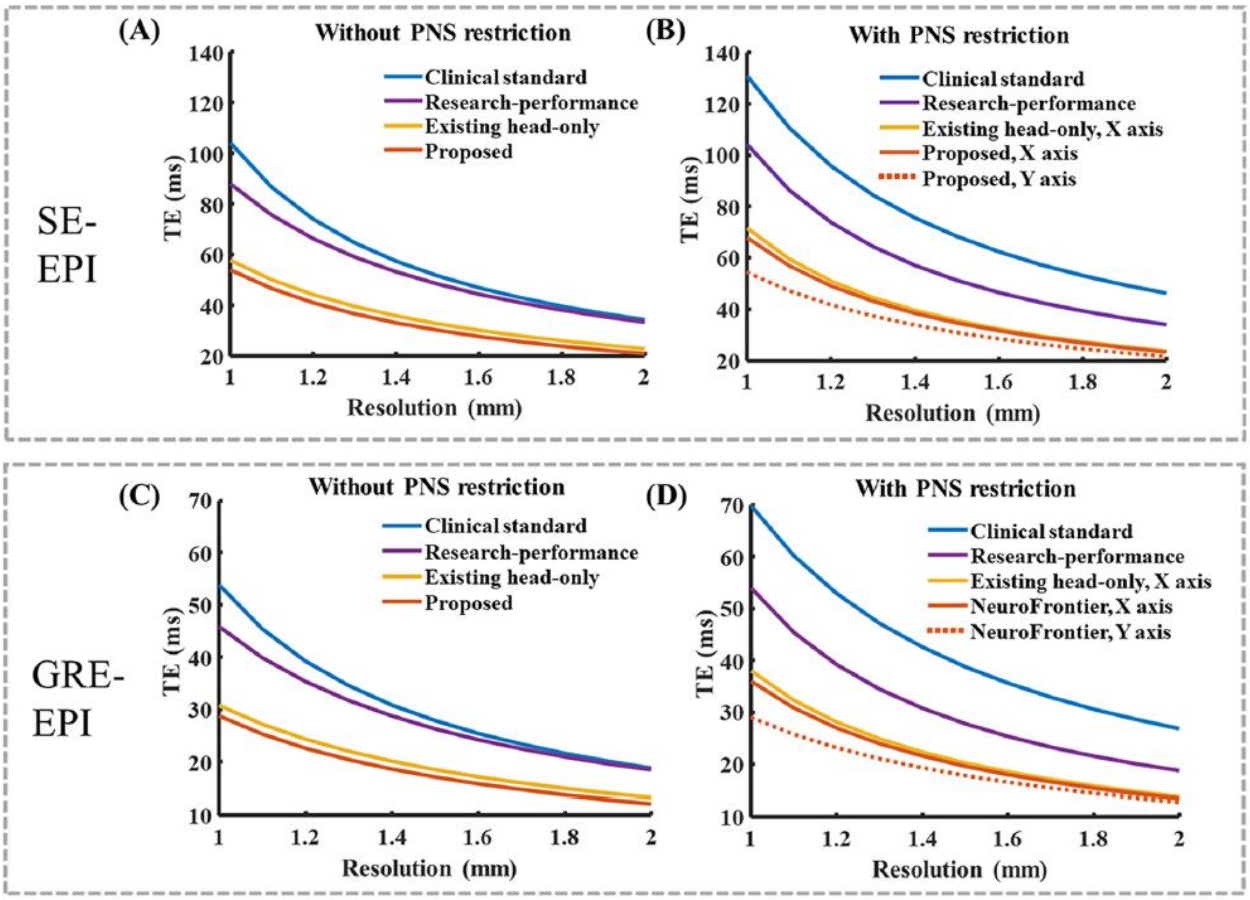

Figure 5. The minimum echo time (TE) as a function of image resolution was calculated for both standard spin-echo (SE) EPI and gradient-echo (GRE) EPI sequences. This calculation was performed with and without peripheral nerve stimulation (PNS) restrictions across various gradient systems. These systems include a standard whole-body clinical system (45 mT/m and 180 T/m/s), a research-performance whole-body system (80 mT/m and 200 T/m/s), an existing head-only gradient system (200 mT/m and 500 T/m/s), and the Neuro-Frontier system (650 mT/m and 600 T/m/s).

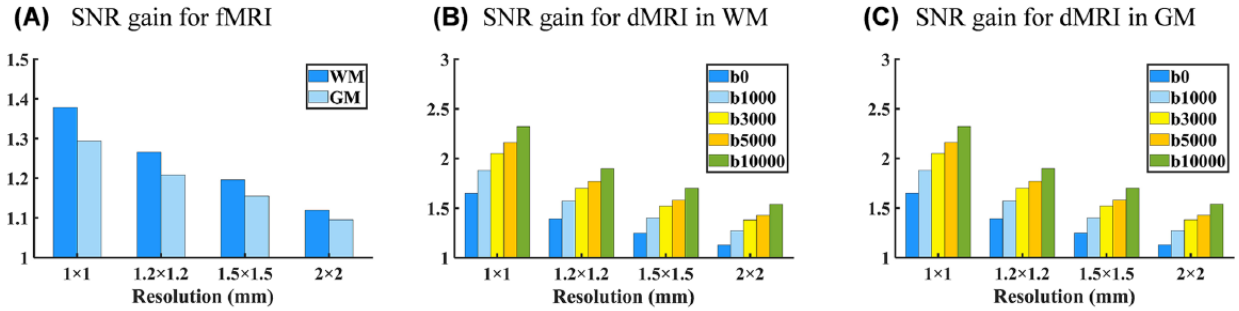

Figure 6. The signal-to-noise ratio (SNR) gain of the proposed NeuroFrontier system, com-pared to a whole-body research-performance scanner (80 mT/m and 200 T/m/s), was simulated for standard fMRI sequences using gradient-echo EPI (GRE-EPI) and dMRI sequences using spin-echo EPI (SE-EPI). The simulations were conducted at various resolutions (1 × 1 mm, 1.2 × 1.2 mm, 1.5 × 1.5 mm, and 2 × 2 mm) and different b-values (b = 0, 1000, 3000, 5000, and 10,000 s/mm²).

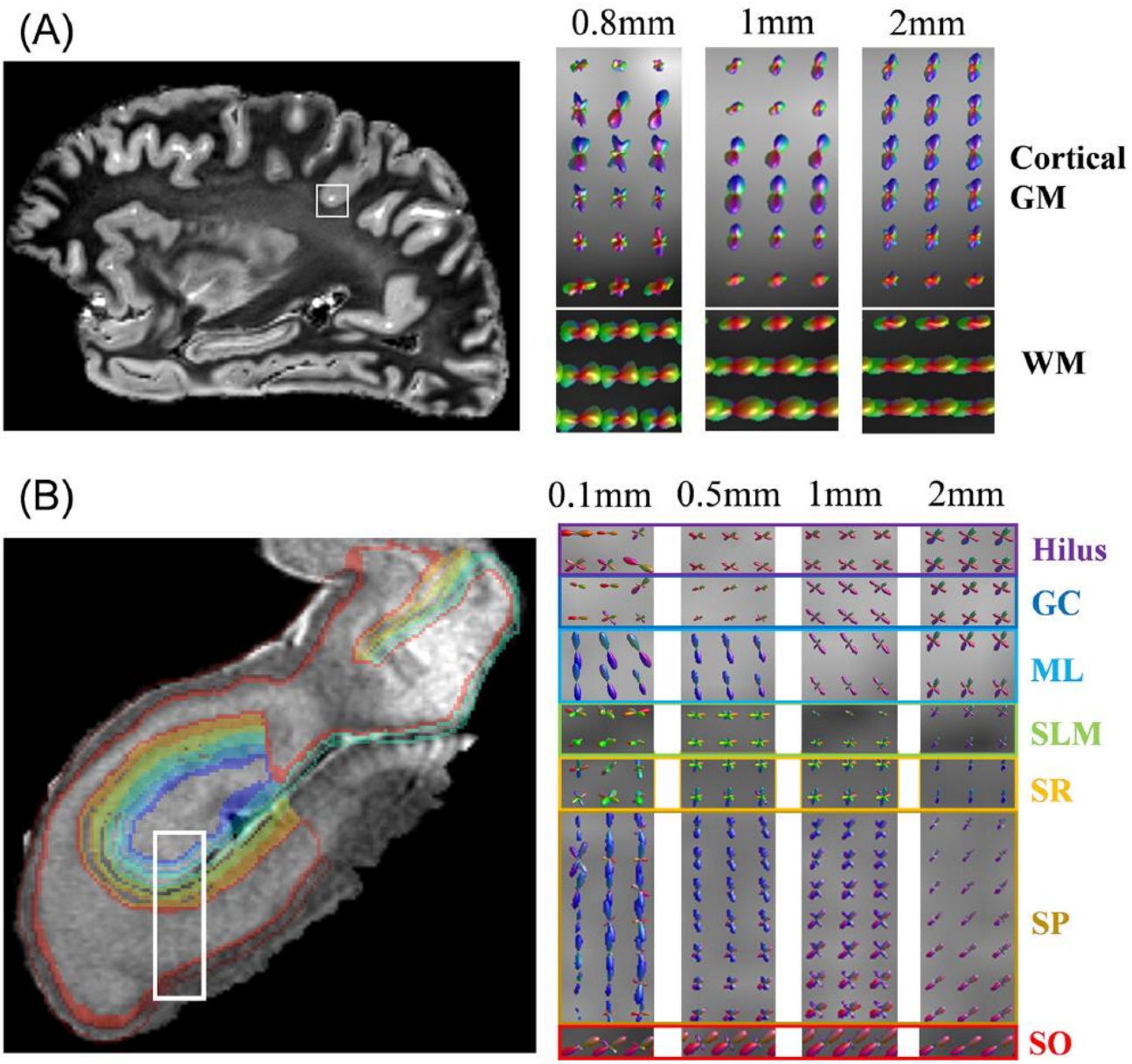

Figure 7. Layer-specific organization of fiber orientation densities (FODs) in the cortex and hippocampus of a human brain specimen was examined at various resolutions. (A) In the cerebral cortex, ex vivo MRI at 0.8 mm isotropic resolution revealed five distinct layers in the gyrus of the parietal lobe. However, as the resolution decreased to 1 mm and 2 mm isotropic (down-sampled from the original data), this layer-specific information gradually became in-distinguishable. (B) In the hippocampal sample, three layers of the dentate gyrus and four layers of CA1 were clearly identifiable at 0.1 mm resolution. This detailed structural information was progressively lost at lower resolutions of 0.5 mm, 1 mm, and 2 mm isotropic, also down-sampled from the original data.

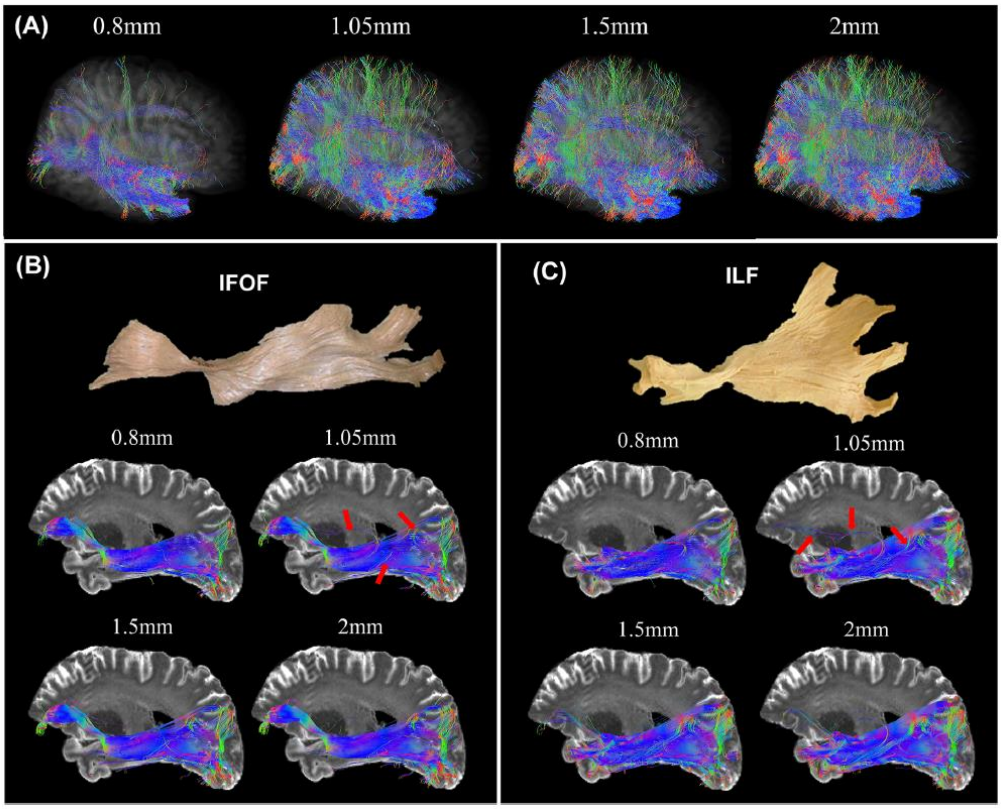

Figure 8. Diffusion tensor imaging (DTI)-based probabilistic tractography was performed at various resolutions for the whole brain (A), and for two representative association fibers: the inferior fronto-occipital fasciculus (B, IFOF) and the inferior longitudinal fasciculus (C, ILF). Red arrows indicate the presence of spurious fiber tracts.

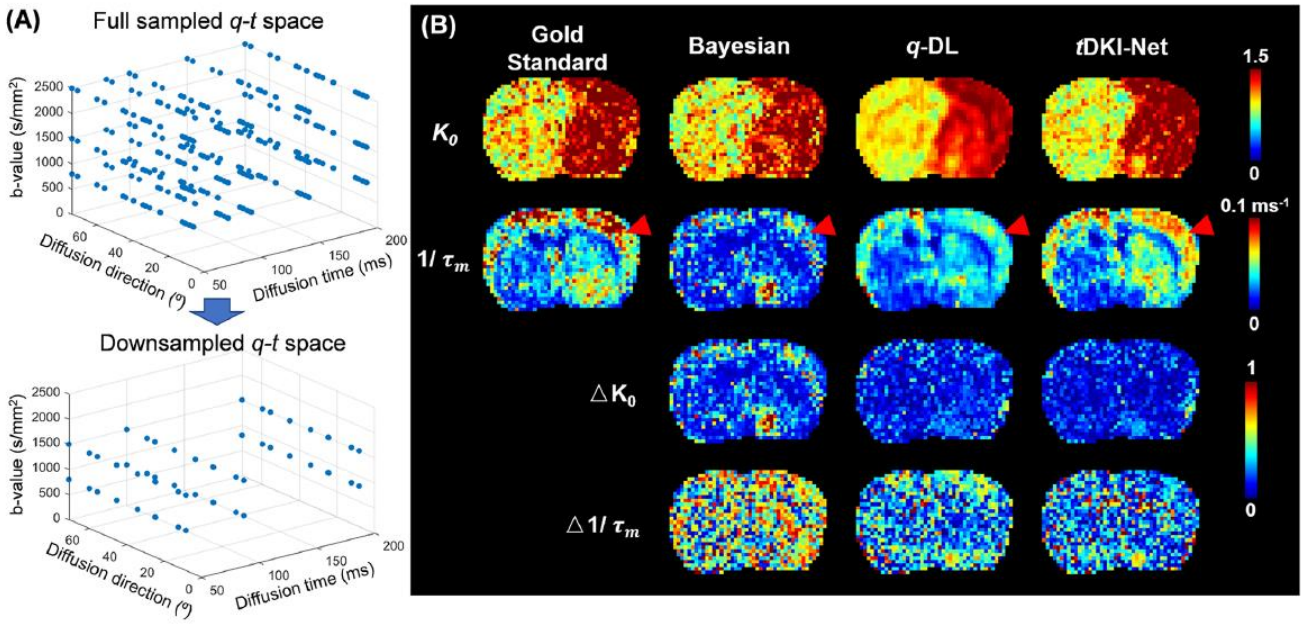

Figure 9. Accelerated q-t space acquisition with deep-learning-based reconstruction. (A) shows the fully sampled q-t space for time-dependent kurtosis imaging using the Karger model to infer transmembrane water exchange (τm), along with the downsampled q-t space used to estimate K0 and τm. Time-dependent DKI data were acquired from a mouse brain after ischemic injury using a Bruker system (Gmax = 570 mT/m and SRmax = 513 T/m/s). (B) The K0 and τm maps were estimated using the fully sampled q-t space (gold standard) and downsampled q-t space with Bayesian estimation, q-space learning, and the network used in the NeuroFrontier system.

4. Discussions and Conclusion

The NeuroFrontier system demonstrates significant advancements in neuroimaging capabilities, achieving high spatiotemporal resolution and improved microstructural mapping accuracy. The integration of AI techniques for fast imaging and prospective motion correction enhances the system's practicality for research and clinical applications. The system's ultra-high gradient performance facilitates detailed exploration of brain microstructures, supporting advanced neuroscience research and potential clinical diagnostics.

One of the primary advantages of the NeuroFrontier system lies in its ability to achieve high-resolution imaging with improved signal-to-noise ratio (SNR). The combination of ultra-high gradient strength and AI-assisted compressed sensing (ACS) allows for rapid acquisition of high-resolution images, making it possible to capture fine structural details within the brain that were previously challenging to visualize. This capability is particularly beneficial for studies requiring precise anatomical and functional mapping of brain regions.

The system's prospective head motion correction technique further enhances image quality by minimizing motion artifacts in real-time. This feature is especially important for functional MRI (fMRI) studies, where subject motion can significantly degrade image quality and affect the accuracy of the data. By incorporating a 3D optical tracking system, the NeuroFrontier ensures that head motion is accurately monitored and corrected, leading to more reliable and reproducible results.

Another notable strength of the NeuroFrontier system is its application in diffusion MRI (dMRI)-based microstructural mapping. The high-gradient performance enables enhanced lesion contrast at short diffusion times or high b-values, improving the estimation accuracy for cellular microstructures. This capability is crucial for studies focused on understanding the microstructural changes associated with neurological diseases and disorders.

Moreover, the system's ability to perform high-resolution tractography with reduced false positives highlights its potential for detailed connectome mapping. This application is essential for elucidating the intricate network of neural connections within the brain and understanding how these connections are altered in various pathological conditions.

In conclusion, the NeuroFrontier system represents a significant advancement in MRI technology, offering unparalleled capabilities for high-resolution neuroimaging. Its integration of ultra-high gradient strength, AI-assisted imaging techniques, and real-time motion correction positions it as a powerful tool for both research and clinical applications. The system's potential to enhance our understanding of brain structure and function, as well as its ability to improve the diagnosis and treatment of neurological conditions, underscores its importance in the future of neuroimaging.

5. References

1 Poo, M.M., Du, J.L., Ip, N.Y., Xiong, Z.Q., Xu, B., Tan, T., 2016. China brain project: basic neuroscience, brain diseases, and brain-inspired computing. Neuron 92 (3), 591–596.

2. Setsompop, K., Kimmlingen, R., Eberlein, E., Witzel, T., Cohen-Adad, J., McNab, J.A., et al., 2013. Pushing the limits of in vivo diffusion MRI for the Human Connectome Project. Neuroimage 80, 220–233.

3. Ugurbil, K., Xu, J.Q., Auerbach, E.J., Moeller, S., Vu, A.T., Duarte-Carvajalino, J.M., et al., 2013. Pushing spatial and temporal resolution for functional and diffusion MRI in the Human Connectome Project. Neuroimage 80, 80–104.

4. Xiang, L., Chen, Y., Chang, W., Zhan, Y., Lin, W., Wang, Q., et al., 2018. Ultra-fast T2-weighted MR reconstruction using complementary T1-weighted information. Med. Image Comput. Comput. Assist. Interv. 11070, 215–223.

5. Cheng, J.Y., Chen, F., Pauly, J.M., Vasanawala, S.S., 2020. Method for performing magnetic resonance imaging reconstruction with unsupervised deep learning. Google Patents, Patent No10,740,931 US Patent and Trademark Office, Washington, DC.

6. Novikov, D.S., Fieremans, E., Jespersen, S.N., Kiselev, V.G., 2019. Quantifying brain microstructure with diffusion MRI: theory and parameter estimation. NMR Biomed. 32 (4).

7. Yang, J., Huber, L., Yu, Y., Bandettini, P.A., 2021. Linking cortical circuit models to human cognition with laminar fMRI. Neurosci. Biobehav. Rev. 128, 467–478.

Author Biography

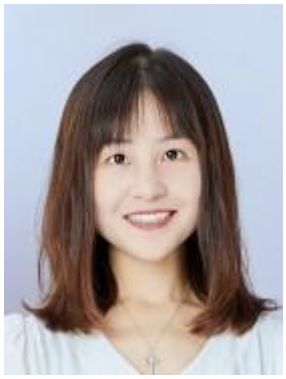

Dr. Dan Wu

Department College of Biomedical Engineering and Instrument Science

Position Tenure-track Professor

Zhejiang University

Dr. Wu's research focuses on Magnetic Resoance Imaging (MRI) acquisition technqiues and neuroimage processing methods. Particularly, she is an expert on diffusion MRI, including high-resolution MRI pulse sequences and microstructural modeling methods. Her lab is also developing advanced acquisition and analytical methods for fetal and infant brain MRI to study the brain development and developmental disorders.

She has published over 60 peer-reviewed journal articles (2/3 of them are first or corresponding author papers) on top journals of the MRI field, such as NeuroImage, Magnetic Resonance in Medicine, Human Brain mpapping, etc. She has also applied 17 patients domestically and internationally (8 of them are patented).

At present, she is the PI of 6 national and provincial projects, including a Youth Project, a General Project and a Key Project (site-PI) of the National Natural Science Foundation of China, a Key Project of the Ministry of Science and Technology, an Innovation and Entrepreneurship Team Project of Zhejiang Province, and the Kunpeng Project of Zhejiang Province (total funding over ￥15,000,000). She was the PI of several NIH grants, including R01, R21 and R03 between 2016-2018.

Dr. Wu was awarded the Innovator Under 35 China by MIT Technology Review in 2019, the Young scientists of World Economic Forum in 2020, the Outstanding Young Researcher of the Chinese Socieity of Biomedical Engineering in 2020, and the Kunpeng Scholar of Zhejiang Province in 2021.

Dr. Wu is a Junior Fellow of the International Society of Magnetic Resonance in Medicine (ISMRM) since 2016, she he serves as a Annual Meeting Program Committee (AMPC) member of ISMRM, the Secretary of the Pediatic MR Study Group, the Secretary of the Placeta & Petus Study Group, and committee member of ISMRM Publication Committee and Education Committee.

5T MRI Compared to 3T MRI in Routine Brain Imaging: An Evaluation of Image Quality

Zhensong Wang[1], Jianxian Liu[1], Zhengyi Li[1], Xin Wang[1], Zhangzhu Li[1], Yuan Guo[1], Dan Yu[2], Jie Gan[1,*]
[1] Department of Radiology, Shandong Provincial Third Hospital: Shandong University Affiliated Shandong Provincial Third Hospital, China
[2] United Imaging Research Institute of Intelligent Imaging, Beijing, China
* Corresponding author

1. Introduction

Ultra-high field Magnetic Resonance Imaging (MRI), defined as systems with main magnetic field strengths exceeding 3T, offers significant advantages over conventional clinical magnets. With comparable imaging parameters, ultra-high field MRI can deliver a higher signal-to-noise ratio (SNR), enabling higher spatial resolution and diminished partial volume effects, thereby enhancing the depiction of intracranial pathologies (1). Research comparing 7T with 3T MRI has highlighted the superiority of the former in visualizing cerebral small vessel diseases, multiple sclerosis, subtle anatomical abnormalities, and lesions associated with temporal lobe epilepsy (2). Furthermore, by optimizing the parameters of the relevant scanning sequence, such as the T2*-weighted gradient echo sequence, the contrast-to-noise ratio (CNR) is also observed to increase with an augmentation in field strength (1). Notably, ultra-high field MRI facilitates clearer visualization of anatomical structures like the amygdala, hippocampus, and substantia nigra, along with their subregions, as CNR improves (3, 4). Functional MRI (fMRI) at these field strengths can even resolve signals from distinct neuronal columns and layers (5). Consequently, ultra-high field MRI provides an abundance of morphological, functional, metabolic, and biochemical information about the brain (2, 6-11), attributable to its superior spatial and contrast resolutions.

Theoretically, both 5T and 7T MRI should produce images with higher SNR and CNR compared to 3T MRI (12, 13). In particular, studies have demonstrated that 5T time-of-flight magnetic resonance angiography (TOF MRA) outperforms 3T in subjective and objective assessments of distal large and small vessel branch visualization, with image quality comparable to 7T (14). Additionally, the use of a 48-channel orthogonal head coil at 5T mitigates radiofrequency (RF) pulse non-uniformity compared to 7T, facilitating the acquisition of high-quality brain images; this holds significant clinical potential. Currently, 5T clinical research is limited. This study aims to compare quantitative and qualitative parameters (SNR, CNR, artifacts, gray/white matter clarity, image quality) of routine cranial sequences at 3T and 5T, using similar scanning sequences and duration, based on previous ultra-high field MRI studies.

2. Materials and Methods

2.1 Study Population

This prospective study was approved by the Institutional Review Board of Shandong Provincial Third Hospital (Approval No. KKLL-2023078), and written signed consents were obtained from all participants prior to each examination. Between July and December 2023, a total of 17 participants (7 males, 10 females; age: 31.94±15.34 years; range: 20-69 years) were recruited through advertisements. The participant pool comprised healthy volunteers and asymptomatic individuals with a history of ischemic cerebrovascular events. The exclusion criteria encompassed those with a history of intracranial aneurysm surgery, intracranial vascular stent placement, heart/respiratory failure, severe consciousness impairment, intracranial hemorrhage, MRI contraindications, or significant motion artifacts in images.

2.2 MRI examinations

All participants underwent both the 3.0T and 5.0T MRI examinations. The 5.0T MRI examinations were conducted using a prototype whole-body MRI scanner (uMR Jupiter®, United Imaging Healthcare) with a 48-channel orthogonal head coil, whereas the corresponding 3T data were acquired utilizing a 3T MRI scanner (Philips “Ingenia”CX, Best, The Netherlands) with a 24-channel receive head coil. Each participant completed clinical routine sequence imaging at both 5T and 3T within a 48-hour period, encompassing T2WI

(T2 Weighted Imaging), T1WI (T1 Weighted Imaging), T2_FLAIR (T2 fluid attenuated inversion recovery), and DWI (Diffusion Weighted Imaging) (Table 1).

2.3 Image Analysis

2.3.1 Quantitative Assessment

After completion of all data collection, images were transmitted to the PACS system (FABRIC2.0 & SYNAPSE4.1). Quantitative measurements were conducted twice, with a time interval of 14 days. All the qualitative analyses were performed by two experienced radiologists with more than 15 years' experience. Two observers were blinded to both the MRI protocols and field strength, and independent measurements within predefined regions of interest (ROIs) were conducted to calculate SNR and CNR, ensuring unbiased quantitative outcomes.

The predefined ROIs encompassed the gray matter of the bilateral frontal lobes at the level of the semioval centers, along with their adjacent subcortical white matter; the bilateral putamen; and the central pons, bilateral cerebellums, and at the level of the middle cerebellar peduncles. SNR and CNR were calculated as follows:

$$SNR = SI/SD$$

$$CNR_{WM/GM} = (SI_{WM} - SI_{GM})/SD_{WM}$$

Where SI is the average signal intensity of brain white/gray matter, and SD is the standard deviation of these intensities within the tissue.

2.3.2 Subjective Assessment

Subjective evaluations were conducted by the same two radiologists, and were also repeated twice within a 14-day interval to ensure consistency. The assessments focused on three MR image index scores: artifacts (5 = no artifacts, 4 = minimal artifacts, 3 = slight artifacts, 2 = moderate artifacts, and 1 = very severe artifacts and non-diagnostic), gray-white matter definition (3 = Clear, 2 = boundary vague, 1 = non-distinguishable), overall image quality (4 = excellent quality, 3 = mild impact on diagnosis, 2 = substantial impact on diagnosis, 1 = non-diagnostic).

2.4 Statistical Analysis

Statistical analyses were performed using SPSS version 27. Qualitative assessment indices (image artifacts, gray-white matter definition, overall image quality) scores of each sequence image of 3.0T and 5.0T were compared by Wilcoxon rank sum tests. P values ≤ 0.05 were considered to be statistically significant for differences between the two groups.

The interobserver agreement of subjective SNR and CNR evaluations was quantified by intraclass correlation coefficients (ICCs). The interobserver agreement was considered to be poor for ICCs = 0.0–0.2, fair for ICCs = 0.2–0.4, moderate for ICCs = 0.4–0.6, substantial for ICCs = 0.6–0.8, and excellent for ICCs = 0.8–1.0. Subjective assessment indicator scores of interobserver agreement were statistically compared by Kappa consistency analysis (0–0.2, slight agreement; 0.21–0.4, fair agreement; 0.41–0.60, moderate agreement; 0.61–0.8, substantial agreement; > 0.8, excellent agreement).

3. Results

In the T2WI and T1WI sequences, the SNR of frontal lobe gray matter at the level of the semioval center, frontal lobe white matter at the level of the semioval center, putamen, pons, and middle cerebellar peduncles all demonstrated the superiority of 5T over 3T (P<0.001). In quantitative measurements of T2_FLAIR, there was a statistically significant difference in SNR of the putamen between the two field strengths (P<0.001), with a lower value in 5T.

There were no significant differences in SNR between 5T and 3T for frontal lobe gray matter at the level of the semioval center, frontal lobe white matter at the level of the semioval center, pons, and middle cerebellar peduncles, although SNR in the pons was slightly lower in 5T. In the T1WI sequence, there was no significant difference in CNR between gray and white matter at the level of the semioval center, with a slightly lower value in 5T (P=0.197). In both T2WI and T2_FLAIR, 5T exhibited higher CNR for gray and white matter at the level of the semioval center compared to 3T. (P<0.001) (Table 2).

Regarding the overall image quality scores, 5T demonstrated superior performance compared to 3T in the T1WI(P=0.006), T2WI (P=0.007), DWI (P=0.041), and T2_FLAIR (P=0.008) sequences (Table 4). For image artifacts, the 3T images in the DWI sequence exhibited significantly more artifacts than the 5T images (P=0.014), particularly in the regions adjacent to the frontal sinus and temporal bone (Figure 2, Table 4). There

were no significant differences in the degree of image artifacts between the two field strengths in the T2WI (P=0.382), T1WI (P=0.104), and T2_FLAIR (P=0.668) sequences (Table 4). The clarity of gray and white matter scores indicated that 5T images were significantly better than 3T images in the DWI (P<0.001) and T2_FLAIR (P=0.007) sequences. However, there were no significant differences between 5T and 3T images in the T1WI (P=0.332) and T2WI (P=0.332) sequences (Table 4).

Intraclass correlation coefficient (ICC) analysis demonstrated moderate to high levels of consistency in the SNR and CNR values of the 5T image sequences and 3T image sequences of intraobserver (Table 3). Kappa consistency analysis revealed moderate to high levels of consistency in the mean scores of interobserver qualitative assessment indicators (image artifacts, gray-white matter definition, overall image quality) for both the 5T and corresponding 3T image sequences (Table 5).

4. Discussions

High-resolution MRI of the central nervous system enables more precise localization of lesions (15) and depiction of their characteristics. This is particularly crucial for a variety of craniocerebral diseases such as multiple sclerosis (MS), temporal lobe epilepsy, cerebrovascular diseases, and tumors. In the case of MS, high-resolution MRI provides detailed insights into the relationship between plaques and blood vessels, iron deposition, and the dynamic evolution of pathological changes over time (16-18). Furthermore, it offers valuable information about microvascular structures in gliomas (19). By generating more detailed images, high-resolution MRI assists doctors in more accurately understanding the nature and location of lesions, thereby facilitating more precise diagnoses and the development of personalized treatment plans. Studies have shown that the central nervous system exhibits exceptional resolution on ultra-high field MRI (3). In certain applications, its spatial resolution can attain 100-200μm, enabling the observation of microstructures, functions, and molecular metabolism within the human body (20).

This study compares the quantitative and qualitative parameters (SNR, CNR, overall image quality, image artifacts, and gray-white matter clarity) of routine cranial sequences between 5T and 3T MRI, using similar scanning sequences and approximately the same scanning duration. The results demonstrate that without increasing scanning time and while enhancing spatial resolution (see Table 1), the SNR of the frontal lobe gray matter, frontal lobe white matter, putamen, pons, and middle cerebellar peduncle in the 5T T2WI and T1WI sequences is superior to that of 3T (P<0.001). This finding is consistent with a recent study on 5T-MRI (14). Numerous high-field MRI studies have also shown varying degrees of increased SNR compared to 3T (4, 21). SNR is a crucial metric for evaluating MRI images. Traditional theory, based on the Boltzmann distribution, suggests that as the magnetic field strength (B0) increases, the difference in the number of protons in low and high energy states increases proportionally. Moreover, the Larmor frequency (ω0) increases with B0, resulting in an increase in the dipole magnetic moment and thus the signal intensity (SI) collected by the coil, which is proportional to $B0^2$ ($SI \propto B0^2$). Considering that noise (N) is also proportional to B0, it was initially derived that SNR is proportional to B0 ($SNR \propto B0$) (22). However, the currently accepted relationship between SNR and B0 in ultra-high field strengths indicates a more exponential than linear relationship, with $SNR \propto B01.65$ (23). In this study, the greatest SNR improvement was observed in the frontal lobe gray matter of the T1WI sequence, whereas the smallest increase was noted in the middle cerebellar peduncle of the same sequence, with 5T SNR values approximately 1.9 times and 1.2 times those of 3T, respectively. These results do not entirely align with previous perspectives. Studies indicate that B0 uniformity significantly impacts SNR in high field strengths, and this uniformity diminishes as field strength increases (23), resulting in variations in radiofrequency (RF) excitation intensity across distinct regions and consequently influencing SNR. Additionally, the uniformity of the RF field decreases with increasing B0 (24). When B0 significantly exceeds 1.5T, wavelength effects in the RF field distribution complicate MR performance, leading to SNR losses (23, 25). Studies have shown that SNR is relatively uniform in the cranium at lower field strengths (e.g., 3.0T), but as field strength increases (e.g., 7.0T), wavelength effects lead to a reduction in SNR uniformity, which becomes more pronounced with increasing field strength. This is manifested as higher SNR at the periphery and lower SNR at the center of cranial images (23).

Table1 Parameters for 5T/3T scanning

	T2W	T1W	T2W_FLAIR	DWI
5 Tesla				
Repetition time (TR)	4200ms	2300ms	9000ms	3284ms
Echo time (TE)	105.12ms	16ms	140.4ms	61.4ms
Field of view（FOV）	230mm×200mm	230mm×200mm	230mm×200mm	230mm×230mm
Image matrix	544×100	384×100	352×100	256×100
Slice thickness	5mm	5mm	5mm	5mm
Number of slices	19	19	19	19
Flip angle (FA)	90°	90°	90°	90°
Acquisition time	2:02min	3:04min	3:18min	2:11min
Pixel resolution in plane	0.42mm×0.42mm	0.65mm×0.65mm	0.65mm×0.65mm	0.9mm×0.9mm
3 Tesla				
Repetition time (TR)	4200ms	2000ms	9000ms	3000ms
Echo time (TE)	105ms	20ms	120ms	86ms
Field of view（FOV）	230mm×200mm	230mm×199mm	230mm×199mm	230mm×230mm
Image matrix	384×313	304×250	308×209	162×162
Slice thickness	5mm	5mm	5mm	5mm
Number of slices	19	19	19	19
Flip angle (FA)	90°	90°	90°	90°
Acquisition time	2:14min	3:04min	3:09min	2:04min
Pixel resolution in plane	0.64mm×0.64mm	0.76mm×0.80mm	0.76mm×0.95mm	1.42mm×1.42mm

Table 2. Statistical results of SNR and CNR for different sequences in 5T and 3T MRI

	5T	3T	t	P
T2WI				
Gray matter SNR (centrum semiovale level)	33.96±5.60	25.16±4.04	4.845	<0.001
White matter SNR (centrum semiovale level)	37.53±5.62	26.55±4.72	6.013	<0.001
Gray-white matter CNR (centrum semiovale level)	14.81±3.46	8.53±2.94	9.220	<0.001
Putamen SNR	27.67±4.83	19.26±4.55	7.590	<0.001
Pons SNR	22.19±3.64	15.43±2.97	7.428	<0.001
Cerebellar peduncle SNR	30.06±4.73	22.05±4.06	7.029	<0.001
T1WI				
Gray matter SNR (centrum semiovale level)	35.93±6.11	18.95±3.39	9.639	<0.001
White matter SNR (centrum semiovale level)	65.20±9.49	49.29±7.7.38	6.408	<0.001
Gray-white matter CNR (centrum semiovale level)	19.31±3.84	21.30±4.08	-1.346	0.197
Putamen SNR	37.28±5.17	27.03±5.10	8.528	<0.001
Pons SNR	32.03±5.33	23.65±4.99	4.793	<0.001
Cerebellar peduncle SNR	40.21±5.45	31.54±5.83	5.769	<0.001
T2_FLAIR				
Gray matter SNR (centrum semiovale level)	41.69±8.01	39.87±6.21	0.711	0.487
White matter SNR (centrum semiovale level)	40.33±6.43	38.81±10.38	0.462	0.650

Gray-white matter CNR (centrum semiovale level)	11.24±3.48	5.52±2.42	9.181	<0.001
Putamen SNR	24.89±4.85	29.84±6.36	-4.596	<0.001
Pons SNR	20.42±3.85	22.37±4.90	-1.471	0.161
Cerebellar peduncle SNR	31.73±5.86	29.62±4.35	1.178	0.256

Table 3. Statistical results of subjective evaluation for 5T and 3T MRI

	5T (Mean ± SD)	**3T (Mean ± SD)**	**P**
Overall image quality			
T1W_FLAIR	3.82±0.85	3.47±0.37	0.006
T2WI	3.94±0.16	3.50±0.58	0.007
DWI	4.00±0.00	3.76±0.43	0.041
T2W_FLAIR	3.82±0.35	3.41±0.30	0.008
Artifacts			
T1W_FLAIR	3.70±0.46	3.47±0.51	0.104
T2WI	4.41±0.44	4.32±0.35	0.382
DWI	3.88±0.21	3.38±0.33	0.014
T2W_FLAIR	4.17±0.24	4.11±0.54	0.668
Gray-white matter clarity			
T1W_FLAIR	3.00±0.00	2.97±0.12	0.332
T2WI	3.00±0.00	2.94±0.24	0.332
DWI	3.00±0.00	2.32±0.30	<0.001
T2W_FLAIR	3.00±0.00	2.76±0.31	0.007

Table 4. ICC analysis results for 5T and 3T MRI sequences

	ICC		**95% CI**		**P**	
	5T-MRI	**3T-MRI**	**5T-MRI**	**3T-MRI**	**5T-MRI**	**3T-MRI**
T2WI						
Gray matter SNR (centrum semiovale level)	0.950	0.803	0.867,0.982	0.536,0.924	<0.001	<0.001
White matter SNR (centrum semiovale level)	0.877	0.892	0.693,0.954	0.728,0.960	<0.001	<0.001
Gray-white matter CNR (centrum semiovale level)	0.919	0.892	0.790,0.970	0.729,0.960	<0.001	<0.001
Putamen SNR	0.574	0.899	0.144,0.821	0.745,0.962	0.006	<0.001
Pons SNR	0.900	0.873	0.747,0.963	0.686,0.952	<0.001	<0.001
Cerebellar peduncle SNR	0.906	0.845	0.760,0.965	0.622,0.941	<0.001	<0.001
T1WI						
Gray matter SNR (centrum semiovale level)	0.764	0.665	0.460,0.908	0.285,0.264	<0.001	0.001
White matter SNR (centrum semiovale level)	0.847	0.817	0.629,0.942	0.564,0.930	<0.001	<0.001
Gray-white matter CNR (centrum semiovale level)	0.523	0.752	0.072,0.796	0.432,0.903	0.013	<0.001
Putamen SNR	0.888	0.819	0.718,0.958	0.568,0.930	<0.001	<0.001
Pons SNR	0.906	0.858	0.760,0.965	0.651,0.946	<0.001	<0.001

Cerebellar peduncle SNR	0.932	0.924	0.823,0.975	0.803,0.972	<0.001	<0.001
T2WI_FLAIR						
Gray matter SNR (centrum semiovale level)	0.777	0.673	0.485,0.913	0.300,0.868	<0.001	0.001
White matter SNR (centrum semiovale level)	0.815	0.890	0.560,0.929	0.722,0.959	<0.001	<0.001
Gray-white matter CNR (centrum semiovale level)	0.881	0.878	0.702,0.955	0.695,0.954	<0.001	<0.001
Putamen SNR	0.909	0.926	0.769,0.966	0.808,0.972	<0.001	<0.001
Pons SNR	0.748	0.798	0.430,0.901	0.527,0.922	<0.001	<0.001
Cerebellar peduncle SNR	0.917	0.754	0.787,0.969	0.442,0.903	<0.001	<0.001

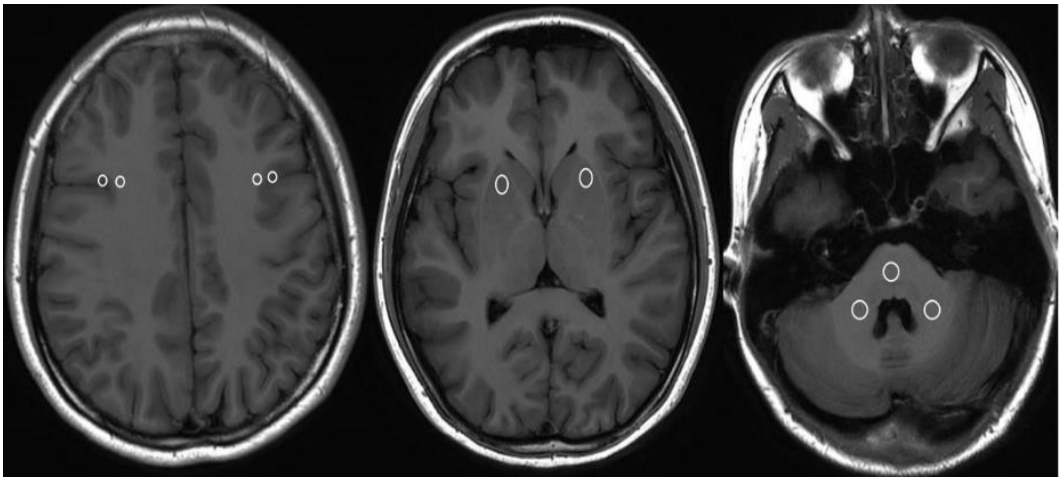

Figure 1. Placement of the regions of interest (ROI). 1a: Gray matter of the frontal lobe and adjacent subcortical white matter at the level of the bilateral centrum semiovale (ROI size: 5-8 mm^2). 1b: Bilateral putamen (ROI size: 20-30 mm^2). 1c: Central pons, bilateral cerebellum, and cerebellar peduncles at the same level (ROI size: 20-30 mm^2).

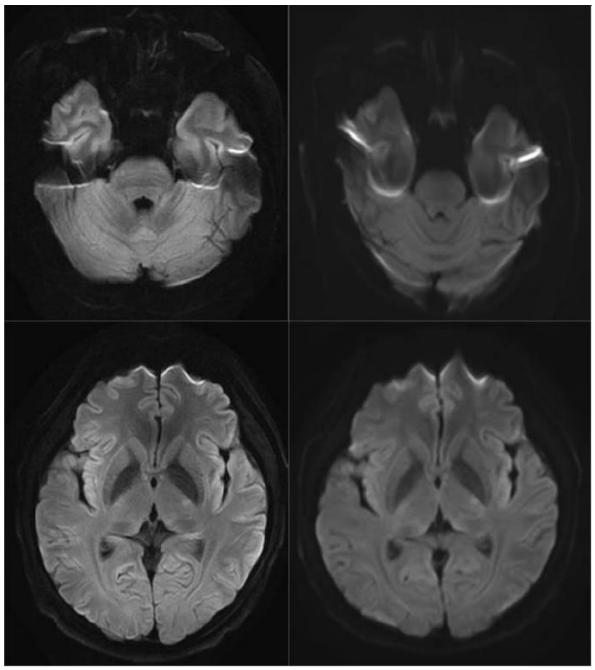

Figure 2. Reduced distortion caused by susceptibility artifacts in the frontal sinus and temporal bone regions in the 5T images compared to the 3T images. 2a, 2b: DWI images of the same participant. 2c, 2d: DWI images of the same participant. 2a, 2c were acquired using a 5T scanner, and 2b, 2d were acquired using a 3T scanner. The images show reduced distortion caused by susceptibility artifacts in the frontal sinus and temporal bone regions in the 5T images compared to the 3T images.

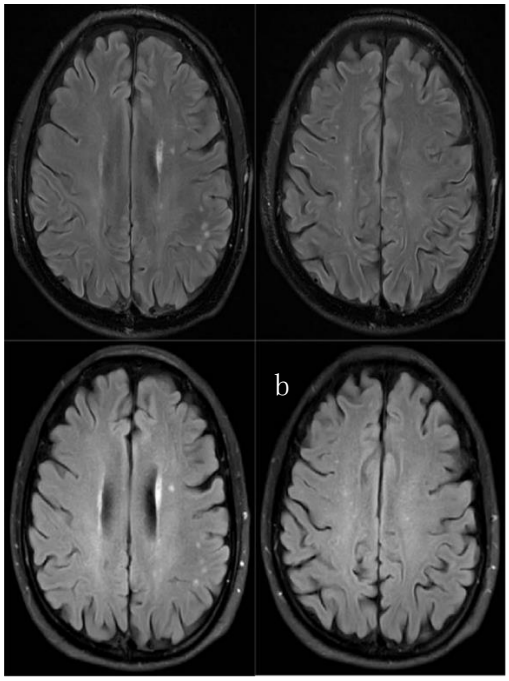

Figure 3. 5T images reveal a greater number of lesions and display clearer lesion boundaries compared to the 3T images. 3a, 3c: T2-FLAIR images of the same participant. 3b, 3d: T2-FLAIR images of the same participant.3a, 3b were acquired using a 5T scanner, and 3c, 3d were acquired using a 3T scanner.

Furthermore, SNR is also influenced by factors such as scanning sequences and tissue relaxation characteristics. Studies have shown that as magnetic field strength increases, tissue T1 values increase and T2 values decrease, SNR continues to elevate with magnetic field strength, albeit at a rate lower than linear, while tissue T1 contrast decreases and T2 contrast increases (26). Therefore, in high-field imaging, imaging sequence TR and TE need to be optimized (e.g., moderately extended) to achieve the best T1/T2 contrast. In this study, to enhance T1 contrast, the TR time of the high-field T1WI sequence was extended by 300 ms compared to 3T. In addition, SNR is closely tied to the coil type (23), where multi-channel surface coils facilitate super-linear SNR enhancements, whereas volume coils exhibit marginally sub-linear SNR gains. Regarding the T2_FLAIR sequence, no significant differences in SNR were observed between the two field strengths in frontal lobe gray matter, frontal lobe white matter, pons, and middle cerebellar peduncle. Intriguingly, SNR in the putamen was notably lower at 5T compared to 3T ($P<0.001$), a finding congruent with a recent study contrasting various field strengths (5T vs 7T) (14). Apart from the previously mentioned factors, this discrepancy might stem from the elevation of tissue T1 values accompanying the increase in B0 (23), as well as reduction in the transverse magnetization vector (Mxy) during the TR interval. Besides, considerations should be given to: (1) the shortened T2 relaxation time and subsequent faster signal attenuation due to age-related physiological iron deposition in the putamen; and (2) the higher spatial resolution at 5T. Consequently, in clinical practice, changes in the SNR of MRI images are anticipated to be more intricate than theoretically predicted (24).

Both T2WI and T2_FLAIR sequences showed superior CNR in the frontal lobe gray and white matter at 5T compared to 3T ($P<0.001$). These results are consistent with numerous ultra-high field MRI studies, which indicate that both 5T and 7T provide higher CNR than 3T (12-14). This superiority may be related to the following factors: 1) the augmentation of magnetic field strength B0 enhances the intensity of magnetic resonance signals. Consequently, when the signal intensities of two different tissues both increase, the difference in signal intensity between them also increases, while the increase in noise is relatively smaller; 2) as B0 increases, T2 values decrease (23), and increasing TE can enhance T2 contrast. Conversely, in the T1WI sequence, there was no significant difference in CNR between the two field

strengths for frontal lobe gray and white matter (P=0.197), with a marginally lower value observed at 5T. This observation is in accordance with a recent study investigating CNR at varying field strengths (Zhang S hi et al., 2023). This outcome may be attributed to the moderate prolongation of TR in ultra-high field strengths, which leads to elevated T1 values and diminished differences among various tissues (23). The overall image quality scores indicated that 5T was superior to 3T, suggesting that the higher spatial resolution and good SNR and CNR achievable at ultra-high field 5T, without increasing scanning time, can provide more detailed intracranial anatomical and pathological information and enable the detection of small lesions that are undetectable by lower field MRI. In this study, one participant showed significantly more white matter high signal intensity at 5T than at 3T (see Figure 2), with clearer lesion boundaries. This observation may be attributed to the enhanced image spatial resolution and improved tissue contrast at 5T. Nevertheless, as field strength escalates, magnetic susceptibility effects and chemical shift phenomena become more sensitive. Additionally, the diminished uniformity of the B0 and RF fields owing to the heightened field strength can significantly compromise image quality at tissue interfaces. For example, brain tissue proximal to the frontal sinus and temporal bone exhibits distortion and warping (see Figure 3). To address this issue, the present study employed a 48-channel orthogonal head coil at 5T, which significantly mitigated RF inhomogeneity, thereby substantially enhancing central nervous system imaging quality and reduced artifact (27-29). Secondly, the application of the multi-shot EPI sequence, with multiple RF excitations, shorter TE, and segmented multiple filling of K-space, contributed to the amelioration of magnetic susceptibility artifacts. Furthermore, this might also be related to the higher stability of the 5T magnetic field uniformity, gradient system, and RF system. Based on these factors, magnetic susceptibility artifacts in the DWI sequence were significantly reduced at 5T compared to 3T. In the assessment of gray-white matter clarity, 5T images from the T1WI and T2WI sequences were not significantly different from those of 3T, while the T2-FLAIR and DWI sequences showed significantly better performance at 5T.

This is consistent with the increased CNR values in the T2-FLAIR sequence at 5T, which enhances gray-white matter contrast. It should be noted that in conventional 3T MRI, the depiction of small lesions is hindered by several factors in the DWI sequence, including limited spatial resolution, convoluted K-space filling patterns, the absence of corrective measures during image acquisition, and prominent magnetic susceptibility artifacts. For instance, it is prone to missed diagnoses or misdiagnoses of MS cortical lesions, epileptogenic foci, and structural changes in the hippocampus in patients with dementia and Parkinson's disease.

Therefore, in this study, the voxel size within the 5T layer was set smaller than that of the 3T layer (5T vs 3T: 0.90mm×0.90mm vs 1.42mm×1.42mm) to evaluate the image quality of the 5T MRI. The scoring results indicated that the overall image quality and the clarity of gray and white matter in the 5T images were superior to those in the 3T images (P=0.041; P<0.001). These findings can be attributed not only to the smaller pixel size and consequently higher spatial resolution in the 5T images, but also to factors such as the use of a multi-shot EPI sequence with multiple RF excitations, shorter TE, and segmented multi-filling of the K-space. Furthermore, the use of a 48-channel orthogonal head coil, along with the higher stability of the gradient and radiofrequency systems in the 5T MRI, contributed to these outcomes. Consequently, the results of this study suggest that in ultra-high field DWI sequences, it is feasible to achieve higher spatial resolution while maintaining a certain level of SNR.

This study demonstrates moderate to high consistency in the ICC values of SNR and CNR across various sequences (excluding DWI) at 5T and 3T, as well as in the Kappa values for qualitative assessment metrics (image artifacts, gray-white matter definition, overall image quality) at both field strengths (see Tables 4-6, 8-10). These findings indicate the robustness and reproducibility of the study results. However, the study cohort comprised solely healthy volunteers or asymptomatic individuals with a history of ischemic cerebrovascular events, thus limiting the generalizability of 5T's efficacy in specific intracranial pathologies. Future research should validate these findings in relevant cranial lesion populations.

The results suggest that within similar scan times, 5T MRI provides higher spatial resolution and improved tissue contrast, thereby laying a solid technological foundation for precise localization and detailed information acquisition in

cranial diseases. Further clinical applications require optimization of sequences to obtain better image data. It is worth mentioning that participants did not experience significant discomfort after the examination, contrasting with previous reports of vertigo in 7T studies (2). This discrepancy may be attributed to the study population.

The study recruited 17 participants for data collection, which constitutes a relatively small sample size for a cross-sectional study. Therefore, the results are presented as preliminary conclusions. Future research should expand the sample size to validate the study's findings. Additionally, as participants were asymptomatic, with only some older individuals showing ischemic infarcts on cranial MRI, the study does not fully demonstrate 5T-MRI's sensitivity to pathological changes. Thus, the focus of future research should be on assessing the lesion detection capabilities of ultra-high field 5T-MRI. Furthermore, the use of MR scanners from different manufacturers, different head coils, and varying sequence acquisition parameters may have influenced image SNR, CNR, and subjective assessment metrics. Moreover, the absence of acceleration techniques to isolate field strength effects resulted in longer overall scan times.

In conclusion, this study demonstrates that, within a comparable scanning duration, 5T MRI offers superior spatial resolution, along with enhanced SNR and CNR, conferring advantages in terms of overall image quality and definition of brain gray matter. Nonetheless, the escalation in field strength also results in an increase in T1 values, intensified inhomogeneity of the RF field, and heightened sensitivity to the chemical shift phenomenon. Consequently, optimizing scanning parameters in clinical settings is imperative to balance SNR, CNR, spatial resolution, and acquisition time, thereby ensuring optimal image quality and enhancing diagnostic accuracy.

5. References

1. Duyn JH, The future of ultra-high field MRI and fMRI for study of the human brain. Neuroimage (2012). 62, 1241–1248. http://dx.doi.org/10.1016/ j.neuroimage. 2011.10.065.
2. Springer E, Dymerska B, Cardoso PL, Robinson SD, Weisstanner C, Wiest R, Schmitt B, Trattnig S, Comparison of Routine Brain Imaging at 3T and 7T. Invest Radiol (2016). Aug; 51(8):469-82. doi: 10.1097/RLI.0000000000000256.
3. Thomas BP, Welch EB, Niederhauser BD, et al., High-resolution 7T MRI of the human hippocampus in vivo. J Magn Reson Imaging (2008). 28(5):1266-1272. DOI: 10.1002/jmri.21576.
4. Cho ZH, Lee YB, Kang CK, et al., Microvascular imaging of asymptomatic MCA steno-occlusive patients using ultra-high-field 7T MRI. J Neurol (2013). 260(1):144–150.
5. Yacoub E, Shmuel A, Pfeuffer J, Van De Moortele PF, Adriany G, Andersen P, Vaughan JT, Merkle H, Ugurbil K, Hu X, Imaging brain function in humans at 7T. Magn Reson Med (2001). 45, 588–594.
6. Trattnig S, Bogner W, Gruber S, et al., Clinical applications at ultrahigh field (7 T). Where does it make the difference? NMR in Biomedicine (2016). Sep; 29(9):1316-1334. DOI: 10.1002/nbm.3272.
7. Beisteiner R, Robinson S, Wurnig M, Hilbert M, Merksa K, Rath J, Hollinger I, Klinger N, Marosi C, Trattnig S, Geissler A, Clinical fMRI: evidence for a 7T benefit over 3T. NeuroImage (2011). 57, 1015–1021.
8. Goncalves NR, Ban H, Sanchez-Panchuelo RM, Francis ST, Schluppeck D, Welchman AE, 7T FMRI reveals systematic functional organization for binocular disparity in dorsal visual cortex. - J. Neurosci (2015). 35, 3056–3072.
9. Bogner W, Chmelik M, Andronesi OC, Sorensen AG, Trattnig S, Gruber S, In Vivo (31) P Spectroscopy by Fully Adiabatic Extended Image Selected In Vivo Spectroscopy: a Comparison Between 3T and 7T. Magn Reson Med (2011). 66, 923–930.
10. Biller A, Badde S, Nagel A, Neumann JO, Wick W, Hertenstein A, Bendszus M, Sahm F, Benkhedah N, Kleesiek J, Improved Brain Tumor Classification by Sodium MR Imaging: prediction of IDH Mutation Status and Tumor Progression. AJNR Am. J. Neuroradiol (2016). 37, 66–73.
11. Zaiss M, Windschuh J, Paech D, Meissner JE, Burth S, Schmitt B, Kickingereder P, Wiestler B, Wick W, Bendszus M,

Schlemmer HP, Ladd ME, Bachert P, Radbruch A, Relaxation-compensated CEST-MRI of the human brain at 7T: unbiased insight into NOE and amide signal changes in human glioblastoma. Neuroimage (2015). 112, 180–188.

12. Triantafyllou C, Hoge RD, Krueger G, et al., Comparison of physiological noise at 1.5T, 3T and 7T and optimization of fMRI acquisition parameters. Neuroimage (2005). 26(1):243–250.17.

13. Vizioli L, Moeller S, Dowdle L, et al., Lowering the thermal noise barrier in functional brain mapping with magnetic resonance imaging. Nat Commun (2021). 12(1):5181.

14. Zhang Shi, Xueying Zhao, Shuo Zhu, Xiyin Miao, Yunfei Zhang, Shihong Han, Bei Wang, Boyu Zhang, Xiaodan Ye, Yongming Dai, Caizhong Chen, Shengxiang Rao, Jiang Lin Mengsu Zeng, He Wang, Time-of-Flight Intracranial MRA at 3T versus 5T versus 7T: Visualization of Distal Small Cerebral Arteries. Radiology (2023). DOI: 10.1148/radiol. 220114.

15. van Veluw SJ, Zwanenburg JJ, Engelen-Lee J, et al., In vivo detection of cerebral cortical microinfarcts with high-resolution 7T MRI. J Cereb Blood Flow Metab (2013). 33:322–329.

16. Dal-Bianco A, Hametner S, Grabner G, et al., Veins in plaques of multiple sclerosis patients—a longitudinal magnetic resonance imaging study at 7Tesla. Eur Radiol (2015). 25:2913–2920.

17. Bagnato F, Hametner S, Yao B, et al., Tracking iron in multiple sclerosis: a combined imaging and histopathological study at 7Tesla. Brain (2011). 134: 3599–3612.

18. Absinta M, Sati P, Gaitán MI, et al., Seven-tesla phase imaging of acute multiple sclerosis lesions: a new window into the inflammatory process. Ann Neurol (2013). 74:669–678.

19. Di Ieva A, Göd S, Grabner G, et al., Three-dimensional susceptibility-weighted imaging at 7T using fractal-based quantitative analysis to grade gliomas. Neuroradiology (2013). 55:35–40.

20. Zidong Wei, Qiaoyan Chen, Shihong Han, Shuheng Zhang, Na Zhang, Lei Zhang, Haining Wang, Qiang He, Peng Cao, Xiaoliang Zhang, Dong Liang, Xin Liu, Ye Li, Hairong Zheng, 5T magnetic resonance imaging: radio frequency hardware and initial brain imaging. Quant Imaging Med Surg (2023). 13(5):3222-3240.

21. Grochowski C, Staśkiewicz G. Ultra high field TOF-MRA: A method to visualize small cerebral vessels. 7T TOF-MRA sequence parameters on different MRI scanners - Literature review. Neurol Neurochir Pol (2017). 51(5):411–418.

22. Collins CM, Smith MB, Signal-to-noise ratio and absorbed power as functions of main magnetic field strength, and definition of "90" RF pulse for the head in the birdcage coil. Magn Reson Med (2001). 45:684–691.

23. Pohmann R, Speck O, Scheffler K, Signal-to-noise ratio and MR tissue parameters in human brain imaging at 3, 7, and 9.4 T using current receive coil arrays. Magn Reson. Med (2016). 75,801–809.

24. Daniel Gallichan, Diffusion MRI of the human brain at ultra-high field (UHF): A review. NeuroImage (2018). DOI: 10.1016/j.neuroimage.

25. Hoult DI, Sensitivity and power deposition in a high-field imaging experiment. J Magn Reson Imaging (2000). 12:46–67.

26. Robin A. de Graaf, Peter B. Brown, Scott McIntyre, Terence W. Nixon, Kevin L. Behar, and Douglas L. Rothman, High Magnetic Field Water and Metabolite Proton T1 and T2 Relaxation in Rat Brain In Vivo. Magnetic Resonance in Medicine (2006). DOI: 10.1002/mrm.20946.

27. de Zwart JA, Ledden PJ, Kellman P, van Gelderen P, Duyn JH, Design of a SENSE-optimized high-sensitivity MRI receive coil for brain imaging. Magn Reson Med (2002). 47, 1218–1227.

28. Wiggins GC, Potthast A, Triantafyllou C, Wiggins CJ, Wald LL, Eightchannel phased array coil and detunable TEM volume coil for 7T brain imaging. Magn Reson Med (2005). 54, 235–240.

29. Wiggins GC, Triantafyllou C, Potthast A, Reykowski A, Nittka M, Wald LL, 32-channel 3T receive-only phased-array head coil with soccer-ball element geometry. Magn Reson Med (2006). 56, 216–223.

Author Biography

Prof. Jie Gan

Chief Physician at the Imaging Center

The Affiliated Hospital of Shandong University, China

Prof. Jie Gan is a Chief Physician at the Imaging Center of the Third Affiliated Hospital of Shandong University. He earned his Master's degree in Imaging Medicine and Nuclear Medicine from Shandong University in 2003 and his Bachelor's degree in Clinical Medicine from Shandong Medical University in 1993. Prof. Gan has accumulated extensive experience in the field of radiology over three decades. His research focuses on advanced multimodal imaging, including 5T MRI, to study lipid metabolism, atherosclerosis, and brain function in Type 2 diabetes. He has led several major projects funded by the Shandong Provincial Health Commission and has published widely in medical journals. Prof. Gan is recognized for his contributions to radiology and continues to innovate in MRI applications.

One-stop dynamic whole-brain CT perfusion with a 320-row scanner for patients with acute ischemic stroke and the clinical value of artificial intelligence iterative reconstruction

Jin Fang[1], Wuming Li[1], Tiantian Wang[2], Liying Peng[2], Guihua Jiang[1,*]
[1]Department of Radiology, The Affiliated Guangdong Second Provincial General Hospital of Jinan University, Guangzhou, China.
[2]Central Research Institute, United Imaging Healthcare, Shanghai, China.
*Corresponding author

1. Introduction

Acute ischemic stroke (AIS) is the leading cause of morbidity and mortality worldwide, accounting for over 80% of all stroke incidents (1). Previous research has indicated that patients who present with salvageable brain or adequate collaterals and undergo early recanalization could have an improved clinical outcome (2). The risk of a poor clinical outcome could increase by around 14% with every 30-minute delay in treatment (3). Therefore, it is essential to identify the salvageable ischemic brain tissue quickly and reliably using an optimal imaging technique.

Many randomized controlled trials have confirmed the importance of computed tomography perfusion (CTP) in diagnosing AIS (4). Specifically, CTP can provide a quantitative assessment of the ischemic core, tissue at risk, and cerebral hemodynamic status (5), benefiting patients undergoing endovascular thrombectomy. In addition, CT angiography (CTA) derived from CTP data can provide intracranial status and assessment for a possible underlying vessel occlusion or other vascular pathologies (6). However, since CTP requires multi-phase scans, the accumulated radiation burden raises a considerable concern (7). In the past few years, considerable efforts have been devoted to minimizing the radiation dose for CTP scans. With the development of their 320-row scanner (uCT 960+, United Imaging Healthcare, Shanghai, China), United Imaging has made it possible to perform one-stop dynamic whole-brain CTP imaging with phase-specific tube current modulation settings to allow the user to effectively optimize and reduce the radiation dose for CTP scans. With the one-stop protocol, brain CTP and CTA images can be obtained simultaneously within a single examination, requiring only a single injection of contrast medium.

Moreover, with the recent rapid developments in artificial intelligence technologies and algorithms, deep learning-based image reconstruction (DLR) has gained considerable interest for the field of CT imaging demonstrating the potential for image quality improvements and low dose imaging capabilities (8). United Imaging has recently introduced an artificial intelligence iterative reconstruction (AIIR, United Imaging Healthcare, Shanghai, China) algorithm (9), which has been developed to combine the advantages of traditional model-based iterative reconstruction algorithms to accurately characterizing image detail and perform low dose imaging with the ability of a convolution neural network CNN to robustly handle the expected image noise and texture. Previous studies using AIIR have provided remarkable outcomes showing improved diagnostic confidence and the ability to perform low dose imaging for abdominal scans, pulmonary and aortic CT angiography and ultra-low dose lung screening applications (10-13). In this work we plan to investigate the ability of AIIR to improve the image quality of CTP scans providing additional clinical value of CT perfusion-derived CTA.

Our study aims to test the reliability of one-stop dynamic whole-brain CTP with a 320-row scanner for AIS patients, and the feasibility of replacing routine CTA with perfusion-derived CTA reconstructed with AIIR for AIS patients.

2. Materials and Methods

2.1 Study Population

The Medical Ethics Committee of our institution approved this retrospective study, eliminating the need for written informed consent.

From February to March 2024, a total of 42 patients with suspected AIS who underwent a one-stop dynamic whole-brain CTP followed by a routine craniocervical CTA examination were enrolled in this study. Seven cases were

excluded due to cerebral hemorrhage. Ten cases were excluded due to a combination with other diseases. The final set consisted of 25 patients with confirmed AIS.

2.2 Imaging Protocol and Reconstruction

All imaging procedures were performed using the 320-row detector CT (uCT 960+, United Imaging Healthcare, Shanghai, China). As shown in Figure 1, the entire one-stop dynamic whole-brain CTP protocol consisted of the following five stages (19 phases): (1) Stage 1 (non-contrast), 150 mAs, 1 phase, 3.0s interval; (2) Stage 2 (flow phases), 75 mAs, 3 phases, 2.0s intervals; (3) Stage 3 (arterial phases, boosted for CTA acquisition), 150 mAs, 5 phases, 2.0s intervals; (4) Stage 4 (venous phases), 75 mAs, 4 phases, 2.0s intervals and (5) Stage 5 (washout phases), 5 mAs, 6 phases, 5.0s intervals. The remaining parameters were kept consistent for each phase: 100 kVp, 0.5s rotation time, and 16 cm z-coverage. The scans were initiated 7.0 s after the injection of iodinated contrast medium.

The routine craniocervical CTA images were acquired 5 minutes after the CTP scan with the following helical scanning parameters: 100 kVp, 240 mAs, 80mm longitudinal collimation, 0.89 pitch, and 0.5s rotation time. The acquisition was triggered using a bolus-tracking technique, initiated 3.6s after the CT value in the level of the aortic arch reached the preset 150 Hounsfield units (HU).

All CTP images were reconstructed with hybrid iterative reconstruction (HIR, United Imaging Healthcare, Shanghai, China), with the slice thickness/increment of 5.0/5.0 mm for further CTP parameter calculations. CTP-derived CTA images were extracted from the CTP scan using the peak arterial phase in stage 3 and reconstructed with AIIR (Group A), with the slice thickness/increment of 1.0/1.0 mm for further vessel evaluation. The routine craniocervical CTA images were reconstructed with HIR, with the slice thickness/increment of 1.0/1.0 mm (Group B).

The volume CT dose index (CTDIvol, mGy) and dose length product (DLP, mGy·cm) were recorded for all scans. The effective dose (ED, mSv) was calculated as the DLP multiplied by the conversion factor of 0.0021 $mSv \cdot mGy^{-1} \cdot cm^{-1}$ (14)

2.3 Perfusion Parameter Calculation

All CTP images were transferred to a clinical workstation (uWS-CT, United Imaging Healthcare, Shanghai, China) for perfusion parameter calculations, where the post-processing software corrects motion, removes background, selects the arterial input function (AIF) and venous input function (VIF), and ultimately generates perfusion parametric maps using the deconvolution method previously described in the literature (15) which are then overlaid on the source CTP images. The perfusion parameters generated include cerebral blood flow (CBF), cerebral blood volume (CBV), mean transit time (MTT), time to peak (TTP), and time-to-maximum of the residual function (Tmax). Areas with a decrease of CBF and/or CBV, or areas with an increase of MTT, TTP and/or Tmax indicate abnormal perfusion.

One radiologist was asked to draw a region of interest (ROI) within the core infarction area, while avoiding the blood vessels, brain sulci and gyri. This ROI was copied to the contralateral side using the midline of the brain as an axis of symmetry to obtain an ROI in a healthy area. The perfusion parameters of the ROI for the core infarction area and the corresponding ROI of the normal healthy area on the contralateral side were recorded.

2.4 Perfusion-derived CTA Image Quality Evaluation

For the CTP-derived CTA images (Group A) and the routine craniocervical CTA images (Group B). Two radiologists were independently asked to locate and evaluate the responsible vessels where the vessel occlusion was defined with a focal loss of vascular opacity without distal vessel delineation. They also independently graded the subjective image quality, including image noise, sharpness of the vascular edge, and small vessel visibility, each using a five-point Likert scale (1: poor, 5: excellent) for images in both Group A and B.

In addition, For the Group A and Group B images, the objective image noise was measured by placing an ROI on the internal carotid artery (ICA), the middle cerebral artery M1 segment (MCA-M1), and the basilar artery (BA). The contrast-to-noise ratio (CNR) between the three arteries relative to brain parenchyma were calculated by:

$$\mathrm{CNR} = (HU_{artery} - HU_{parenchyma}) / \sqrt{(SD_{artery}{}^2 + SD_{parenchyma}{}^2)/2}$$

where HU and SD denote the mean and standard deviation of CT value within the ROI, respectively.

2.5 Statistics Analysis

Statistical analysis was performed using IBM SPSS Statistics 27.0 (IBM Corp., Armonk, NY, USA). Continuous variables were presented as mean ± standard deviation (SD) or median and interquartile range (IQR) depending on the normality of the data. The normality was examined using the Kolmogorov-Smirnov test. For data with normal distribution, the student's t-test was used, otherwise, the Wilcoxon signed-rank test was used. Categorical variables were expressed as numbers and percentages, where the difference was analyzed using the Wilcoxon signed-rank test. A two-tailed $p < 0.05$ was considered statistically significant.

3. Results

3.1 Patient Characteristics and Radiation Dose

A total of 25 patients (mean age: 67.5 ± 12.5 y, range 50-90 y, male/female: 13/12) with confirmed AIS were enrolled in the evaluation. The mean CTDIvol of the one-stop dynamic whole-brain CTP protocol was 163.2 ± 0.1 mGy, which was comparable to that of previously published CTP protocols with a fixed tube voltage (80 kVp) and tube current (150 mAs) (16). The ED of the one-stop dynamic whole-brain CTP protocol was 5.5 ± 0.0 mSv, which was lower than the cumulative radiation dose (> 10 mSv) for whole-brain CTP and CTA scans reported in the literature (17). For routine craniocervical CTA, the mean CTDIvol and DLP were 9.7 ± 0.0 mGy and 454.7 ± 24.9 mGy/cm, respectively.

3.2 Perfusion Parameter

As shown in Table 1, the perfusion parameters were significantly different between the core infarction area and the contralateral healthy area (all $p < 0.05$). Compared with the contralateral healthy area, CBF and CBV in the core infarction area were significantly decreased, while TTP, MTT and Tmax were significantly increased. One representative case is shown in Figure 2.

3.3 Perfusion-derived CTA Image Quality

The diagnosis of responsible vessels was consistent between Groups A and B, where a total of 13 patients were diagnosed with complete vascular occlusion, while the other 12 patients were diagnosed with above-moderate vascular stenosis.

Both Group A and B demonstrate good diagnostic quality, as evaluated by the scores of the three subjective metrics with all mean scores exceeding 4. This implies that the CTP-derived CTA with AIIR could provide a comparably good diagnostic quality as the routine CTA with HIR. When comparing group A and B, the likert scores were significantly higher in Group B than those in Group A (all $p < 0.05$), where the average scores were 4.96 ± 0.20 versus 4.00 ± 0.00, 4.96 ± 0.20 versus 4.71 ± 0.55 and 4.92 ± 0.28 versus 4.04± 0.20 for image noise, sharpness of the vascular edge and small vessel visibility, respectively. Among all metrics, the improvement of the subjective score seemed to be most profound on the small vessel visibility. As shown in Figure 3, Group A provided sharper arterial boundaries and improved intracranial artery visualization, especially for small arterial details on distal second-order branches with reduced image noise than Group B.

AIIR showed a remarkable capability for image noise suppression, leading to a significantly higher CNR (all $p < 0.001$) for ICA, MCA-M1, and BA in Group A (28.7 ± 10.5, 12.9± 7.2, and 15.0 ± 10.6) than those in Group B (17.8 ± 8.9, 7.5 ± 3.5, and 9.1 ± 7.5).

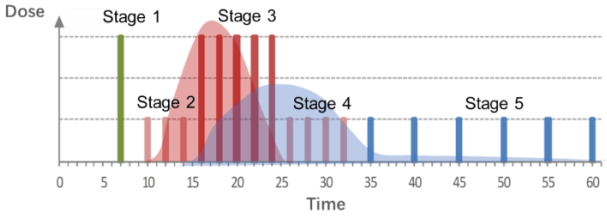

Figure 1. Acquisition protocol of the one-stop dynamic whole-brain CTP. The red and light blue curves mean the arterial input function and venous input function curves, respectively.

Table 1. Comparison of perfusion parameters between the infarct lesions and their corresponding contralateral healthy regions

Perfusion parameter	Core infarction area	Contralateral healthy area	*p* value
CBV (ml/100 g)	1.1 ± 0.4	2.7 ± 2.2	< 0.05
CBF [ml/100 g/min]	7.6 ± 4.5	13.0 ± 6.0	< 0.05
MTT (s)	15.9 ± 6.0	11.0 ± 1.7	< 0.05
TTP (s)	30.3 ± 10.2	23.3 ± 7.4	< 0.05
Tmax (s)	10.5 ± 5.2	2.3 ± 1.0	< 0.05

Note: CBV, cerebral blood volume; CBF, cerebral flood volume; MTT, mean transit time; TTP, time to peak; Tmax, time-to-maximum of the residual function

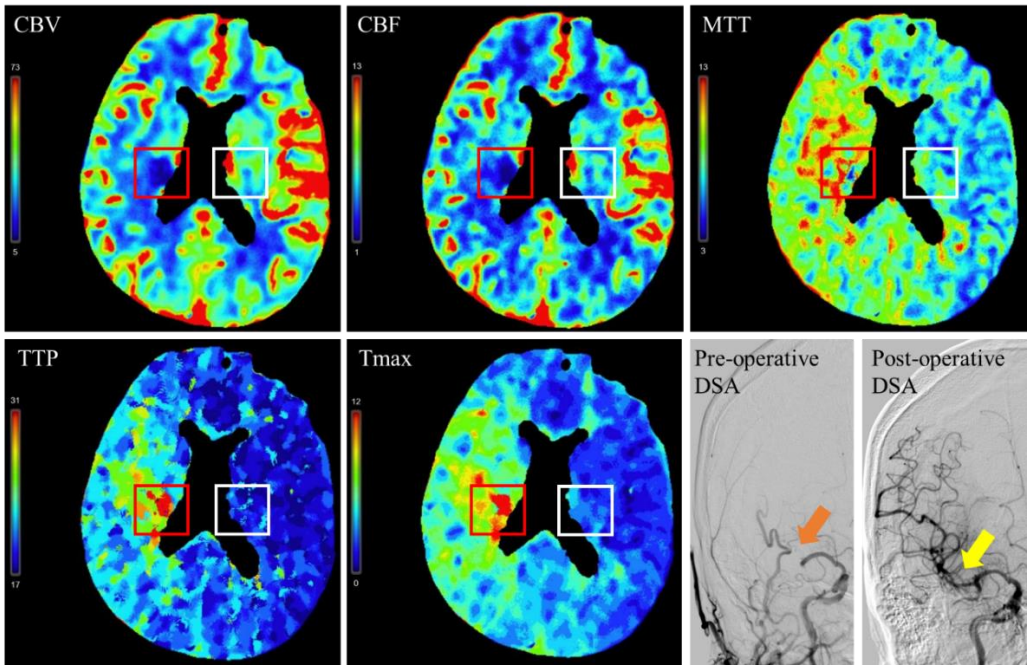

Figure 2. Perfusion parameter maps from a 68-year-old man with acute occlusion of the right middle cerebral artery (R-MCA) confirmed by digital subtraction angiography (DSA), where the R-MCA was totally occluded (orange arrow) in pre-operative DSA while was recanalized (yellow arrow) in post-operative DSA. The perfusion parameters were significantly different between the core infraction area (right frontal lobe, red box) and the contralateral healthy area (left frontal lobe, white box), where CBV and CBF were decreased, and MTT, TTP and Tmax were increased.

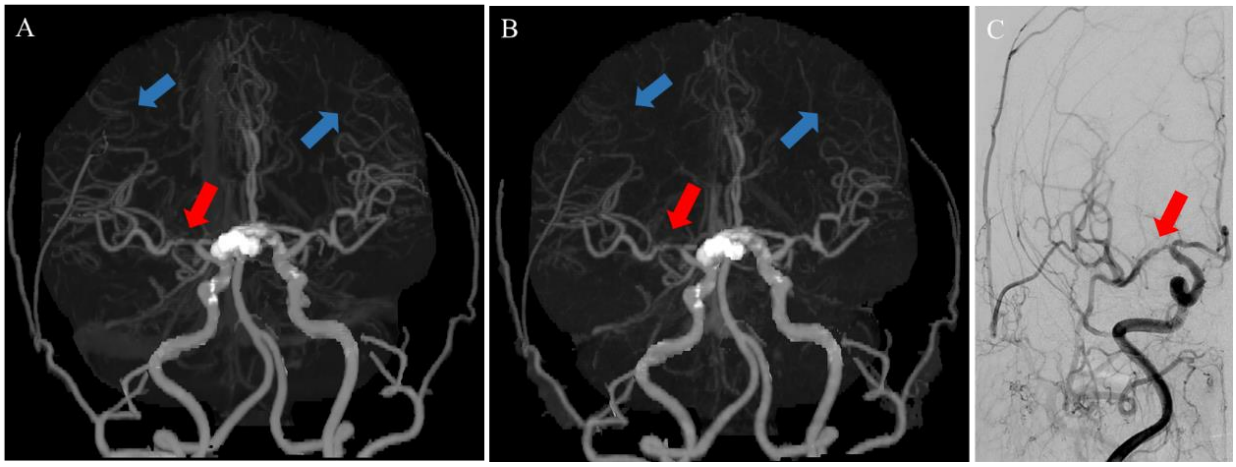

Figure 3 Maximum intensity projection of perfusion-derived cerebral CTA with artificial intelligence iterative reconstruction from Gorup A (A), and routine cerebral CTA with hybrid iterative reconstruction from Group B (B) of a 69-year-old female with severe stenosis of the right middle cerebral artery (red arrow) confirmed by digital subtraction angiography (C). When A and B are compared, Image A shows an improved intracranial artery visualization, especially for small arterial details on distal second-order branches with reduced image noise (blue arrows). The rating of the sharpness of the vascular edge, and the small vessel visibility was 5 vs. 4 and 5 vs. 4 for images A and B, respectively.

4. Discussions

In this study, one-stop dynamic whole-cerebral CTP with a 320-row scanner was performed on patients with AIS, which allows the rapid and accurate detection of acute ischemic areas. By using the advanced AIIR algorithm, perfusion-derived CTA images achieved comparable diagnostic image quality to that of routine CTA for AIS patients, while also providing enhanced small vessel visibility.

Although there is currently no reference standard for the selection of imaging type in patients with AIS, CTP is used in many stroke centers for patient selection (18). The DEFUSE 3 trial (Endovascular Therapy Following Imaging Evaluation for Ischemic Stroke 3) showed that AIS patients with a large penumbra and a small ischemic core revealed by perfusion imaging would benefit from mechanical thrombectomy outside of a 6-h therapeutic window (up to 16 h pose-onset) (19). CTA in diagnosing patients with AIS is also crucial, given that CTA helps in detecting the responsible vessels or occluded vessels. In this study, one-stop dynamic whole-brain CTP enables simultaneously CTP and CTA imaging, accelerating the clinical workflow for AIS patients. Although a fixed tube voltage (100 kVp) was used in this study, we were able to achieve a radiation dose comparable to that of previously reported CTP protocols with a fixed 80 kVp (CTDIvol: 163.2 vs 184.2 mGy) by adapting the tube current in different phases (16).

In contrast to the conventional scan protocols of performing CTA separately, the intracranial CTA images were derived from CTP at the peak arterial phase in this study. Results have shown perfusion-derived CTA with AIIR could achieve comparable diagnostic image quality to that of the routine CTA for AIS patients, thereby eliminating the need to perform an additional CTA scan which in turn reduces the need for additional radiation exposure and contrast agent.

There were several limitations in this study. First, the study population was relatively small, and a larger cohort may provide additional insights into the clinical utility of one-stop dynamic whole-cerebral CTP. Additionally, the investigation was conducted only in the routine dose setting that we believed to be most relevant in practice. Expanding this evaluation to a low-dose setting would be one of our future interests.

5. Conclusion

In conclusion, one-stop dynamic whole-cerebral CTP allows for rapid and accurate detection of ischemic core and tissues at risk. Moreover, by using the advanced artificial intelligence iterative reconstruction, the perfusion-derived CTA could achieve comparable diagnostic image quality to that of the routine cerebral CTA, thereby reducing radiation exposure and accelerating the clinical workflow for AIS patients.

6. Image/Figure Courtesy

All images are provided courtesy of The Affiliated Guangdong Second Provincial General Hospital of Jinan University, Guangzhou, China.

7. References

1. Virani SS, Alonso A, Aparicio HJ et al (2021) Heart Disease and Stroke Statistics-2021 Update: A Report From the American Heart Association. Circulation 143:e254-e743.

2. Broderick JP, Schroth G (2013) What the SWIFT and TREVO II trials tell us about the role of endovascular therapy for acute stroke. Stroke 44:1761-1764.

3. Menon BK, Almekhlafi MA, Pereira VM et al (2014) Optimal workflow and process-based performance measures for endovascular therapy in acute ischemic stroke: analysis of the Solitaire FR thrombectomy for acute revascularization study. Stroke 45:2024-2029.

4. Albers GW, Marks MP, Kemp S et al (2018) Thrombectomy for Stroke at 6 to 16 Hours with Selection by Perfusion Imaging. The New England journal of medicine 378:708-718.

5. Campbell BCV, Khatri P (2020) Stroke. The Lancet 396:129-142.

6. Kilburg C, Scott McNally J, de Havenon A, Taussky P, Kalani MY, Park MS (2017) Advanced imaging in acute ischemic stroke. Neurosurgical focus 42:E10.

7. Chen Y, Wang Y, Su T et al (2023) Deep Learning Reconstruction Improves the Image Quality of CT Angiography Derived From 80-kVp Cerebral CT Perfusion Data. Acad Radiol 30:2666-2673.

8. Koetzier LR, Mastrodicasa D, Szczykutowicz TP et al (2023) Deep Learning Image Reconstruction for CT: Technical Principles and Clinical Prospects. Radiology 306:e221257.

9. United Imaging Healthcare, AIIR-the world's pioneering CT image reconstruction technology, Technical White Paper (2023).

10. Li J, Zhu J, Zou Y et al (2024) Diagnostic CT of colorectal cancer with artificial intelligence iterative reconstruction: A clinical evaluation. Eur J Radiol 171:111301.

11. Gong H, Peng L, Du X et al (2024) Artificial Intelligence Iterative Reconstruction in Computed Tomography Angiography: An Evaluation on Pulmonary Arteries and Aorta With Routine Dose Settings. J Comput Assist Tomogr 48:244-250.

12. Yang L, Liu H, Han J et al (2023) Ultra-low-dose CT lung screening with artificial intelligence iterative reconstruction: evaluation via automatic nodule-detection software. Clin Radiol 78:525-531.

13. Li W, You Y, Zhong S et al (2022) Image quality assessment of artificial intelligence iterative reconstruction for low dose aortic CTA: A feasibility study of 70 kVp and reduced contrast medium volume. Eur J Radiol 149:110221.

14. Brouwer PA, Bosman T, van Walderveen MAA, Krings T, Leroux AA, Willems PWA (2010) Dynamic 320-Section CT Angiography in Cranial Arteriovenous Shunting Lesions. American Journal of Neuroradiology 31:767.

15. Eastwood JD, Lev MH, Azhari T et al (2002) CT perfusion scanning with deconvolution analysis: pilot study in patients with acute middle cerebral artery stroke. Radiology 222(1):227-36.

16. Li Z-l, Li H, Zhang K et al (2014) Improvement of image quality and radiation dose of CT perfusion of the brain by means of low-tube voltage (70 KV). Eur Radiol 24:1906-1913.

17. Chung KJ, Khaw AV, Lee DH, Pandey S, Mandzia J, Lee T-Y (2022) Low-dose CT Perfusion with Sparse-view Filtered Back Projection in Acute Ischemic Stroke. Academic Radiology 29:1502-1511.

18. Menon BK, d'Esterre CD, Qazi EM et al (2015) Multiphase CT Angiography: A New Tool for the Imaging Triage of Patients with Acute Ischemic Stroke. Radiology 275:510-520.

19. Lu S-s, Zhang X, Xu X-q et al (2019) Comparison of CT angiography collaterals for predicting target perfusion profile and clinical outcome in patients with acute ischemic stroke. Eur Radiol 29:4922-4929.

Author Biographies

Dr. Guihua Jiang

Professor

Director of Medical Imaging Center,
The Affiliated Guangdong Second Provincial General Hospital of Jinan University,
Guangzhou, China

Dr. Guihua Jiang is a chief physician, doctoral supervisor, and the director of Medical Imaging Center of the Guangdong Second Provincial General Hospital affiliated to Jinan University, receiving his Ph.D. in neuroimaging from the Southern Medical University. He is an experienced expert in molecular imaging and artificial intelligence, receiving several national and provincial research awards and serving on the editorial board of several journals.

Dr. Jin Fang

Deputy chief physician of Medical Imaging Center,
The Affiliated Guangdong Second Provincial General Hospital of Jinan University,
Guangzhou, China

Dr. Jin Fang is a deputy chief physician as well as the director of the diagnostic team at the Medical Imaging Center of the Guangdong Second Provincial General Hospital affiliated to Jinan University, after graduating from the Capital Medical University. He specializes in neuroimaging and focus on the molecular imaging and artificial intelligence.

Role of MULTIPLEX MRI in the characterization of brain tissues

Anand H.K.[a] , Ramachandra C.R.[a], Lohith H.P. [a], Pooja B. P.[a], Harshith G. [a], Arjun Raju[a]
[a]Tenet Diagnostic Centre, Bengaluru, India

1. Introduction

Brain tumors present a significant diagnostic and therapeutic challenge due to their heterogeneity, variability in progression, and response to treatment (1). Accurately distinguishing between control brain tissue and tumor regions, as well as characterizing the grade and type of tumors, is crucial for optimizing treatment strategies (2).

Advances in magnetic resonance imaging (MRI) technology have significantly enhanced the ability to non-invasively characterize brain tissues, providing critical information for diagnosing and understanding neurological disorders. Brain tumors are routinely evaluated using T1-weighted pre- and post-gadolinium contrast (T1w and T1wGd), T2-weighted (T2w), fluid-attenuated inversion recovery (T2w FLAIR), perfusion, and diffusion-weighted MRI sequences (3). The lengthy acquisition times (~30 min) of conventional quantitative MR techniques hinder their clinical adoption. Currently, MRI-based diagnosis primarily relies on visual inspection and interpretation, as the analysis of complex multi-parametric and multimodal data continues to be challenging (4, 5).

To overcome these limitations, advanced multi-parametric MRI techniques are being developed, which can simultaneously offer T1 mapping, T2/T2* mapping, quantitative susceptibility mapping (QSM), and proton density (PD) mapping etc. These techniques offer quantitative data and improve the objective assessment of brain tumors, showing potential to differentiate between tumor types, grades, and other pathological conditions with greater precision (5-7).

Pirkl CM et al. (5) investigated accelerated 3D imaging techniques for mapping T1, T2, and PD in glioma patients, assessing the feasibility of these fast protocols for clinical use. Deistung A et al. (8) emphasized the importance of integrating QSM into routine MRI protocols for glioblastoma, which could enhance diagnosis and treatment strategies. Quantitative MRI measurements, including T1, T2, T2*, PD, and QSM, provide valuable insights into the microstructural changes associated with Parkinson's disease (9-10).

Acquiring multiple quantitative MR parameters in a single, shorter scan would enhance patient comfort and reduce the risk of misalignment of critical anatomical details between imaging sequences taken at different times. Among the most promising developments in this field is MULTIPLEX (MTP)[1] MRI (11), a single-scan, multi-parametric 3D high-resolution MRI technique that offers detailed anatomical and quantitative information across multiple imaging modalities. By capturing high resolution (e.g. 1 mm isotropic voxels or less) images, MTP MRI generates 14 distinct sets of images, including T1W, PD, T2*-weighted, and susceptibility-weighted images (SWI), as well as quantitative maps of T1, T2*, PD, and QSM. It utilizes a design featuring dual repetition times (TR), dual flip angles (FA), and multi-echo gradient echo (GRE), combined with advanced image processing techniques such as multi-dimensional integration and cutting-edge algorithms (11). This approach provides comprehensive structural, functional, and biochemical information about brain tissues within a single scan lasting approximately 7.5 minutes (11).
On the other hand, machine learning (ML) has demonstrated significant potential in medical imaging, particularly for the automated classification of brain tumors (12). With the potential of quantitative MR mapping in brain tumor diagnosis, we aim to investigate machine learning models for brain tissue classification using multi-parametric (MTP) data. The objective of this study was to assess the role of T1, T2*, PD, and QSM mapping obtained from MTP MRI in the characterization of control and malignant brain tissues using ML algorithms.

[1] This product is not available for sale in the U.S. for clinical uses and also may not be available for such sales in other countries.

2. Materials and Methods

2.1 MRI data

This prospective study used an MRI dataset of 14 subjects (age: 45 ± 10 years) who were suspected of having brain diseases. Scanning was performed on a 3T MR scanner (uMR 780, United Imaging Healthcare Co., Ltd., Shanghai, China) at Tenet Diagnostics, Bengaluru, India from April 2024 to June 2024. All patients underwent MRI as part of their routine clinical care, and written informed consent was obtained from all participants. The MTP was acquired using a 3D GRE sequence with the following parameters: dual flip angles of 4° and 16°, repetition times (TR1/TR2) of 7.21 ms and 28.29 ms, seven echoes with echo times (TE) ranging from 3.05 ms to 22.97 ms, a bandwidth of 260 Hz/px, a matrix size of 218 × 256, 36 slices, and a 3D voxel size of 1.03 × 0.82 × 2 mm^3.. Without additional scan time, the MTP sequence produced T1, T2*, PD and susceptibility-weighted images together with their corresponding quantitative maps. All reconstructed T1, T2*, PD, and QSM maps were aligned in the same spatial coordinates.

2.2 Data processing

MRI data in DICOM format were transferred to a workstation and processed using MATLAB (v. 2022; MathWorks, Natick, MA, USA). An elliptical region of interest (ROI) was utilized to measure the quantitative parameter values in the T1, T2*, PD, and QSM maps for both healthy and malignant brain tissues.

Figure 1 provides an illustration of the maps generated from MTP, along with ROI markings displayed on the quantitative maps.

2.2.1 Diagnostic performance of the maps derived from MTP

Parameters derived from MTP, such as T1, T2*, PD, and QSM values are used as input features for ML algorithms. Linear support-vector machine (SVM), Gaussian SVM and k-nearest neighbor (KNN) were employed to evaluate the diagnostic accuracy of the proposed framework by classification of control (n =14) and malignant (n =14) tissues using stratified 5-fold cross-validation. Figure 2 illustrates the workflow of the proposed methodology.

2.2.2 Statistical analysis

The performance of the classification model was evaluated by calculating key metrics such as sensitivity, specificity, accuracy, and the area under the receiver-operating characteristic curve (AUROC). To further analyze the differences in T1, T2*, PD, and QSM values between the two groups, a paired t-test was conducted. Additionally, boxplots were used to visually represent the distribution and variability of these quantitative parameters,

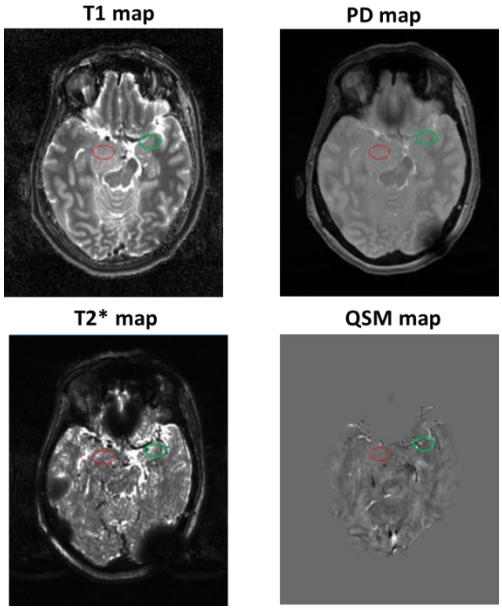

Figure 1: Example of the T1, T2*, PD and QSM maps derived from MTP MRI., Red ROI represents the malignant lesion and green ROI represents the healthy tissues

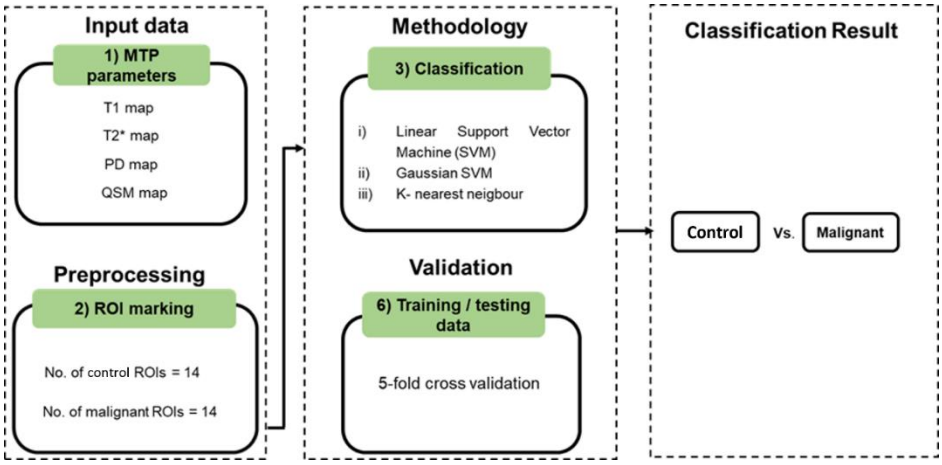

Figure 2: Overview of the proposed framework for classification using parameters derived by MTP

3 Results

3.1 T1, T2*, PD and QSM values

The mean values of T1, T2*, and QSM in malignant tissues were observed to be 1357.50 ± 99.70 ms, 67.08 ± 14.53 ms, and 0.061 ± 0.003 ppm, respectively. In comparison, healthy tissues exhibited mean values of 918.08 ± 101.23 ms for T1, 42.08 ± 15 ms for T2*, and 0.014 ± 0.007 ppm for QSM. The differences in T1, T2*, and QSM values between malignant and healthy tissues were statistically significant, with a *p*-value of less than 0.05. However, there were no significant differences in the PD values between the two groups. Boxplots illustrating the quantitative parameter values for both groups are shown in Figure 3.

3.2 Diagnostic performance using machine learn learning methods

The performance of the proposed classification model was evaluated using individual parametric maps (T1, T2*, PD, and QSM) as well as their combinations, such as combination of T1/T2* and T1/T2*/QSM. The combination of T1 and T2* parameters achieved a sensitivity of 74.23 ± 2.06%, a specificity of 78.56 ± 1.50%, an accuracy of 81.50 ± 1.10%, and an AUC of 0.80 when using a Gaussian SVM classifier. Additionally, the classification performance of PD alone was assessed, but it demonstrated poor accuracy, suggesting that this parameter has limited utility in the current pathological context. In contrast, the highest classification performance was achieved using the combination of T1, T2*, and QSM values. The Gaussian SVM classifier demonstrated a sensitivity of 82.10 ± 1.10%, a specificity of 84.34 ± 2.10%, an accuracy of 84.18 ± 1.10%, and an AUC of 0.83 for two-class classification. Figure 4 presents the ROC curves for the two-class classifications using three different classifiers. The results indicate that combining T1, T2*, and QSM parameters yields superior classification accuracy compared to using individual parameters.

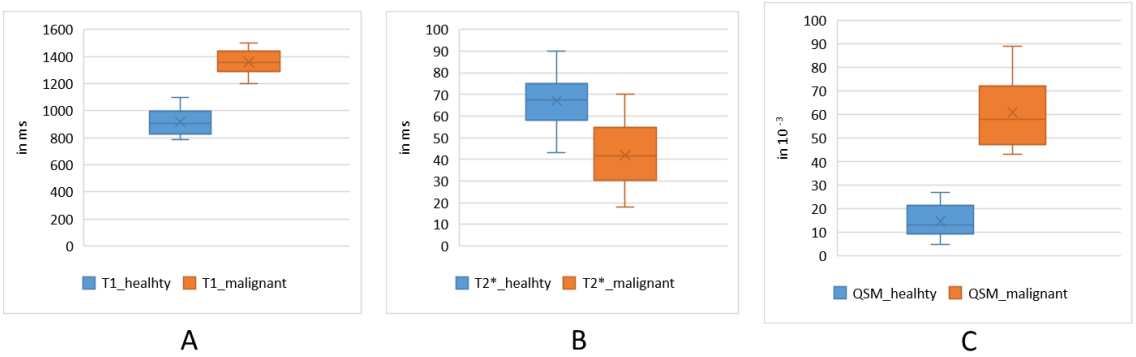

Figure 3: Boxplots for the comparison for A) T1, B) T2* and C) QSM values between healthy and malignant tissues

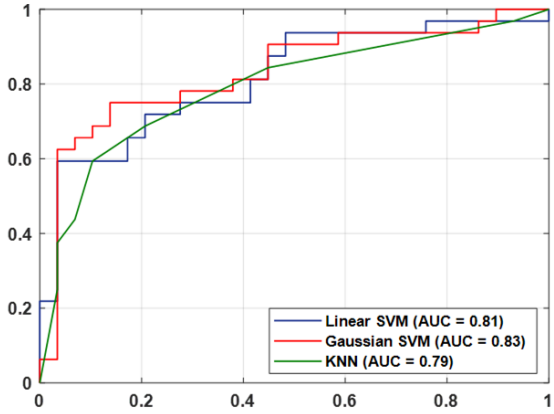

Figure 4: ROC graphs for the two-class classification using the combination of T1, T2*, and QSM maps

4. Discussions

The integration of MTP MRI and ML techniques for the characterization of healthy and malignant brain tissues offers significant advantages over conventional imaging methods. This study demonstrates that combining quantitative MTP parameters, such as T1, T2*, and QSM, can improve the diagnostic accuracy and differentiation between normal and tumor tissues.

One of the primary strengths of MTP MRI (11) is its ability to acquire multiple imaging parameters in a single scan, thus reducing scan time and minimizing patient discomfort. Traditional MRI sequences often require multiple scans, increasing the likelihood of patient movement and image misregistration. The ability to extract several quantitative maps in one session enhances diagnostic efficiency and allows for a more comprehensive evaluation of tissue microstructure. These quantitative maps provide objective, reproducible measurements that overcome the subjectivity associated with conventional MRI interpretation.

This study highlights the performance of ML algorithms, particularly linear SVM, Gaussian SVMs and KNN. These algorithms were selected based on the previous literature (13-14). Notably, the combination of T1, T2*, and QSM parameters achieved higher classification accuracy, with AUC of 0.83, significantly outperforming the use of single parameters. These results emphasize the importance of combining multiple parameters to capture the full spectrum of tissue characteristics, especially in complex tumor environments where individual parameters may provide limited information.

The study reinforces the critical role of QSM and T2* maps in tissue characterization. Both parameters have proven sensitive to microstructural changes in the tumor environment. While the results of this pilot study are promising, few limitations must be acknowledged. First, the dataset was small. Larger, multi-center datasets are needed to validate the generalizability of these findings across diverse populations and tumor types. Future research should focus on external validation to assess model performance in real-world clinical settings.

Additionally, despite the strong performance of T1, T2*, and QSM combinations, other potentially valuable parameters—such as DWI and perfusion-weighted imaging were not explored in this study. These modalities could provide complementary information about tumor cellularity and vascularity, further enhancing the ML models' ability to distinguish between different tumor types and grades. Future studies could investigate the inclusion of these parameters to develop even more robust, multi-modal ML models.

5. Conclusion

This study highlights the advantages of MTP MRI for brain tissue characterization, offering multiple quantitative parameters, such as T1, T2*, PD and QSM, in a single and fast scan. The ability to acquire high-resolution, multi-parametric data significantly improves diagnostic accuracy when combined with ML techniques. By reducing scan time and minimizing misregistration, MTP MRI provides a more efficient, comprehensive, and objective evaluation of brain tissues, enhancing its potential for use in clinical practice and personalized treatment planning.

6. Image/Figure Courtesy

All images are the courtesy of Tenet Diagnostic, Bengaluru India.

7. References

1. Qin D, et al. Tumor Progression and Treatment-Related Changes: Radiological Diagnosis Challenges for the Evaluation of Post Treated Glioma. Cancers (Basel). 2022;14(15):3771.

2. Zacharaki EI, et al. Classification of brain tumor type and grade using MRI texture and shape in a machine learning scheme. Magn Reson Med. 2009 ;62(6):1609-18.

3. Juratli TA, et al. Radiographic assessment of contrast enhancement and T2/FLAIR mismatch sign in lower grade gliomas: correlation with molecular groups. J Neuro-Oncology. 2019; 141: 327–35.

4. Ellingson BM, et al. Consensus recommendations for a standardized Brain Tumor Imaging Protocol in clinical trials. Neuro-Oncology. 2015; 17:1188–1198.

5. Pirkl CM, et al. Accelerated 3D whole-brain T1, T2, and proton density mapping: feasibility for clinical glioma MR imaging. Neuroradiology. 2021; 63, 1831–1851.

6. Seiler A, et al. Multiparametric quantitative MRI in neurological diseases. Front Neurol. 2021;12.

7. Cao T, et al. Three-dimensional simultaneous brain mapping of T1, T2, T2∗ and magnetic susceptibility with MR Multitasking. Magn Reson Med. 2022;87(3):1375-1389.

8. Deistung A, et al. Quantitative susceptibility mapping differentiates between blood depositions and calcifications in patients with glioblastoma. PLoS One. 2013;8(3): e57924.

9. Fu T, et al. Brain morphological alterations are detected in early-stage Parkinson's disease with MRI morphometry. J Neuroimaging. 2020; 30:786–92.

10. Klietz M, et al. Cerebral microstructural alterations in patients with early Parkinson's disease detected with quantitative magnetic resonance measurements. Front Aging Neurosci. 2021; 13: 763331.

11.Yongquan y, et al. MULTI-parametric MR imaging with fLEXible design (MULTIPLEX). Magn Reson Med. 2022; 87: 658–73.

12. Silva Santana L, et al. Application of Machine Learning for Classification of Brain Tumors: A Systematic Review and Meta-Analysis. World neurosurgery. 2024; 186: 204–218.e2.

13. Wasule V, et al. Classification of brain MRI using SVM and KNN classifier. 2017 Third International Conference on Sensing, Signal Processing and Security (ICSSS). 2017; 218-223.

14. Machhale K, et al. MRI brain cancer classification using hybrid classifier (SVM-KNN)," International Conference on Industrial Instrumentation and Control (ICIC). 2015; 60-65.

Author Biographies

Dr. Anand H.K.
Chief of Medical Services and CEO,
Tenet Diagnostics,
Ex-President of Indian Radiological and Imaging Association (IRIA), Karnataka
Bengaluru, India

Dr. Anand H. K. is an experienced Radiology and Imaging expert with over 22 years in the field. He is the Chief of Medical Services and CEO at Tenet Diagnostics in Bengaluru. He completed his MBBS in 1996 and earned an MD in Radiology with a Gold Medal in 2000 from Kasturba Medical College, Manipal, India. Dr. Anand co-founded Clumax Diagnostics and has worked as a Consultant Radiologist at various healthcare institutions. He also served as an Assistant Professor at Kasturba Medical College and is an accomplished researcher in areas like Neuro Radiology, Body and Musculoskeletal Imaging, and Cardiac Imaging. He received multiple Radiologists Fellowships for CT Coronary Angiography and has presented and published research at national and international conferences. His contributions demonstrate his dedication to advancing the field of Radiology.

PASSION for CHANGE

If you have any questions about the magazine, or simply wish to reach out to us for any other reasons, you are welcomed to contact us at the following email address: compliance@united-imaging.com